Probing Stark Atoms

Jeremy J. Murray-Krezan
Albuquerque, NM

B.S. University of New Mexico May 2000
M.A. University of Virginia May 2003

A Dissertation presented to the Graduate Faculty
of the University of Virginia in Candidacy for the Degree of
Doctor of Philosophy

Department of Physics

University of Virginia
January 2007

_____

_____

_____

_____

Thesis advisor

R.R. Jones

Author

J. Murray-Krezan

Abstract

Alkaline earth atoms are laser excited in a static-electric field and probed using two experimental techniques: scaled energy recurrence spectroscopy and impulsive momentum retrieval. In scaled energy recurrence spectroscopy experiments, orbital dynamics of two-electron alkaline earth atoms in a static-electric field are studied. Specifically, photoabsorption spectra for Ba and Ca Rydberg atoms are measured as continuous functions of static-electric field and energy. In both atomic species, the laser excitation proceeds through the singly-excited nd series which are strongly perturbed by doubly-excited valence configurations. Clear signatures of the two-electron dynamics associated with these perturbing configurations are observed. In impulsive momentum retrieval (IMR) experiments, approximate momentum distributions of Rydberg electrons in static-electric fields are obtained using the IMR technique in conjunction with spatially sensitive detection, where an imaging detector enables the measurement of half-cycle pulse (HCP) ionization probability across the spatial profile of a focused HCP beam. By modulating the HCP amplitude [Zeibel and Jones, Phys. Rev. A 68, 023410 (2003)], we directly measure the derivative of the ionization vs. HCP impulse curve, enabling the recovery of momentum distributions with finer resolution than previously attainable. A thorough exploration of the HCP radiation utilized in these IMR experiments is also presented. Additionally, we develop a wave-packet method to simulate the effect that a finite HCP duration has on our measurements, and reasonable agreement between simulated and measured momentum distributions is obtained. Elements of both experimental techniques for probing Stark atoms are advanced in these studies. Furthermore, interesting properties of Stark atoms are demonstrated experimentally.

Contents

Dedicated to my wife Cristina,
my daughter Maylin.

Chapter 1

Introduction

1.1 "Why cannot we write the entire 24 volumes of the Encyclopedia Britannica on the head of a pin?"

In a talk titled "Plenty of Room at the Bottom," (December 1959) Richard Feynman asked this question and many others that are important to the concepts of quantum control. From an experimental point of view, a quantum control process is one where pulses of electromagnetic fields are used to control quantum mechanical systems. This notion is mentioned in Feynman's talk, where at several points he comes to the conclusion that in order to control the "very, very small world" of atoms and molecules, reliable probes of the systems must be developed.

Much of the current research in Atomic, Molecular, and Optical physics is driven by experimental and theoretical efforts to overcome technical limitations. For example, interesting advancements in the field of probing atomic and molecular systems have been facilitated by the development of attosecond pulses of light [1], [2], [3], [4]. While these experiments capitalize on the recent development of attosecond pulses, they often borrow

from the experimental and theoretical ground work of femtosecond physics and chemistry. In a twist on a pump-probe experiment, measurements of atomic transients demonstrated the generation and detection of single 250-attosecond pulses as these pulses excite atoms, which in turn emit electrons and 'tomographic images' of the time-momentum distribution of the ejected electrons are obtained [3]. Attosecond pulse frequencies are typically centered in the extreme-ultraviolet, or soft x-ray, portion of the spectrum, which potentially opens the door for time-resolved x-ray diffraction experiments. In principle, such experiments could resolve structure of a radial wavefunction as a function of time. Interestingly, time-resolved radial probability distributions of arbitrary atoms are difficult to measure experimentally, largely due to the fact that electrons only interact with visible and infrared laser light when the electron is near the ion core. A half-cycle pulse (HCP) is a unique probe in this respect, since an electron and HCP may exchange momentum at any position in the electron's radial probability distribution [5] [6]. However, the fact that previous measurements have not been capable of performing a direct, time-resolved measurement of an arbitrary electronic radial-probability distribution, is perhaps surprising to many physicists, since the concept of the radial wavefunction is so very basic to quantum mechanics that it is taken for granted. This demonstrates that even though much is known about quantum mechanics and atomic physics, there is significant room for continued development, even at very basic levels.

Another aspect of current research in Atomic, Molecular, and Optical physics is exploration of the outstanding questions of complexity in increasingly sophisticated systems, eg. multi-electron atoms, molecules, and these systems coupled to external fields. Specifically, molecules are challenging systems for theoretical and experimental studies. However, if one can understand how to probe multi-electron atoms, maybe one can begin to understand how to probe molecular systems. Particularly interesting in the field is the idea of watching chemical reactions happening through time resolved probes of the electronic probability dis-

tribution [7], [2], [4], which is related to the attosecond work previously discussed. Still, the challenge presented by complex systems, ie. more complex than the hydrogen atom, is great enough that even when a system is only slightly more complicated than the one-electron atom, for example two-electron atoms, the development of new probing techniques is still relevant in the modern field of research.

Atoms coupled to external fields are interesting from the perspective of quantum control as well. Recent advancements have demonstrated that a Rydberg electron, phase-locked to a microwave field, can be made into a non-dispersing wave-packet with lifetimes on the order of $900ns$ [8]. In this experiment a HCP is used to probe the electronic probability distribution. The electron is found as a function of the oscillating-microwave field direction, either traveling with positive or negative momentum along the field axis. In other experiments, by applying a series of pulsed electric fields, coherence of Rydberg wave-packet states is preserved for as long as $20\mu s$ [9]. Here, quantum state coherence is measured by determination of atomic state populations as a function of time using a technique called state selective field ionization.

Returning to the point of how the manipulation of atomic systems can be used for writing information in a very small format, as Feynman challenged the scientific community to do in 1959, recently there has been substantial interest in the idea of using atoms for information storage and processing [9], [10], [11], [12]. A few different proposals for writing information onto atoms have been demonstrated, but a common theme is to use properties of the electronic wavefunction to develop a symbolic language [11], [12]. Encoding information onto the electronic wavefunction is, in some cases, as simple as exposing the atom to laser light [15] or a pulsed electric field. The exquisite control over electronic states exhibited in experiments, including those discussed in the previous paragraph as well as many others, suggests that writing on an atom is possible with today's technology. Retrieving the information, as Feynman's lecture also mentioned, is the more challenging problem in practice. Some exper-

iments have made progress toward this goal. In studies by Ahn *et al.* [11], a wave-packet is excited and manipulated, or written to, then interfered with a second, reference wave-packet. Interference of the two wave-packets provides the recovery mechanism for the information encoded in the complex amplitudes and phases of the wavefunction. A second proposal is to encode information in the electronic probability distribution, a method first discussed by Noel and Stroud [12]. An example of this approach is also found in the experimental study in Ch. 5. In the Stark states studied there, calling a state where the probability distribution does not exhibit any structure a **0**, and calling a state where the probability distribution exhibits structure a **1**, defines an experimentally practical system for encoding information onto atoms. The difference between writing a **1** or **0** in this system is a function of the laser frequency that drives the transition, and a HCP probe facilitates resolution of the differences between these two states.

Although Einstein described stimulated emission in 1917, it was not until 1960 that Theodore Maiman developed the first working laser [34]. So when Feynman asked the visionary question that lends this section its title, lasers were only theoretical devices. Today, lasers are useful tools that along with many other applications, can write information onto atoms. While there is still much to be achieved, undoubtedly the science of manipulating atoms has evolved so that to Feynman's question we answer that *we can, in principle, write the 24 volumes of the Encyclopedia Britannica on the head of a pin.* Feynman's question is visionary because it asks for a fairly simple task, but it is also a vehicle that takes the science to new frontiers. We can certainly perform the task of encoding information on atoms at a rudimentary level, and in the journey to this achievement, much has been learned about atomic systems and lasers as well.

Control and measurement are intrinsically linked. This dissertation is primarily concerned with developing probing methods for atomic systems. Dynamics in perturbed Rydberg series

are probed in a static electric field using scaled energy recurrence spectroscopy [17] (Ch. 3). The study of perturbed Rydberg series demonstrates that this wave-packet interferometry technique can be applied to understand multi-configurational atoms, with the possibility of application to even more complex systems, including molecules. Additionally, in Ch. 5, a novel detection method is explored that ultimately provides a higher resolution measurement of electronic momentum distributions. Chapter 6 continues along this line of study with investigations where the half-cycle pulse is used as a probe of a couple of atomic systems. Both types of measurements presented in this thesis demonstrate significant advancements in probing sophisticated atomic systems.

1.2 Rydberg Atoms

The Coulomb potential problem is one of few problems in quantum mechanics that are solvable in closed form, making it the natural starting point for a discussion of Rydberg atoms. Perturbation theory provides a method for extending solutions of the hydrogen atom to atoms with large atomic cores. These approximate techniques have empirical parameters called the quantum defects, δ_l. Rydberg atoms are described with this formalism, when the excited electron's principle quantum number, n, is large [16]. Typically, Rydberg electrons have $n > 10$. Quantum defects are labeled by l for the corresponding series of angular momentum. Energy levels in Rydberg atoms, ie. alkali, alkaline-earth, and other Rydberg electron systems, are described in terms of the effective quantum number, $n^* = n - \delta_l$. The energy of the electron is defined (in atomic units) to be:

$$E = -\frac{1}{2n^{*2}}. \tag{1.1}$$

The quantum defect is physically meaningful in a scattering picture where δ_l is the phase shift of the non-hydrogenic wave, relative to the hydrogenic wave, scattering from the real

atomic potential [16].

In addition to being a system where the spectroscopy can be described theoretically, Rydberg atoms are also interesting experimentally, because the transitions to large n in alkali and alkaline-earth atoms are driven with lasers and/or other electromagnetic pulses. Interestingly, Rydberg transitions can be driven in molecules and solid-state systems, although this thesis does not include any molecular or solid-state studies. This thesis presents studies of alkaline-earth atoms, which have two optically accessible electrons. It is worth mentioning though, that most of the experimental techniques applied to the alkaline-earth atoms in this thesis are equally valid for the study of alkali atoms.

Rydberg atoms are interesting for several physical reasons. To begin, Rydberg atoms are often well-described in classical terms as an electron with a highly-elliptical orbit [16]. This is because in the large n limit, the correspondence principle is applicable. The electron on a highly elliptical orbit has a characteristic period, the Kepler period, which is $\tau_K = 2\pi/\Delta E$, where ΔE is the characteristic energy spacing between n-labeled energy levels. When $n^* > 24$, the Kepler period of a Rydberg electron is greater than $2ps$, which makes these atomic systems well-suited for time-resolved ultra-short pulse laser experiments.

Another reason that Rydberg atoms are interesting systems to study experimentally is that they are sensitive to external fields with magnitude on the same order as the Coulomb binding potential. A typical number that quantifies this statement is that an electron with energy corresponding to $n^* = 30$ is ionized by a static electric field greater than $400V/cm$. Manipulation of Rydberg atoms with external fields, eg. lasers and pulsed electric fields, have been successfully demonstrated in a variety of experiments. A small sample of quantum control experiments have already been mentioned in this chapter and include Refs. [6, 9, 8, 14, 15, 11, 13, 7]. Two topics that are relevant to the study of Rydberg electrons affected by external fields are the Stark effect and Rydberg wave-packets, both of which are discussed

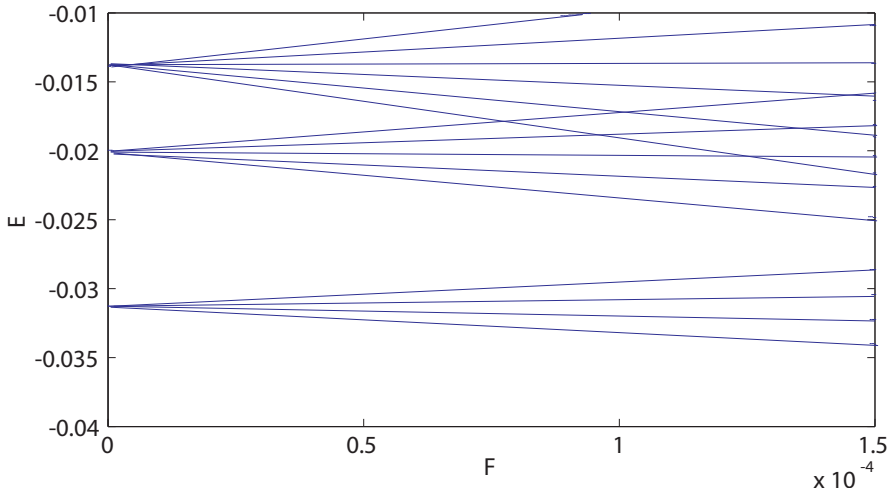

Figure 1.1: Calculated Stark Spectrum of H, plotted as a function of binding energy and electric field strength in atomic units. $E(F)$ is given by Eq. 1.2. Energy levels where $m = 0$, $n = 4, 5$ and 6 are shown in the plot.

in the following sections, and in the body chapters of this thesis.

1.3 The Stark Effect

A bound electron in a combined Coulomb and static-electric field, F, experiences a Stark shift of its energy levels. Although the solution of this problem, for small static-electric fields, in spherical coordinates, is the classic problem in time-independent degenerate perturbation theory [19], the symmetry of the problem is most naturally utilized in parabolic coordinates ($\xi = r + z, \eta = r - z, \phi = arctan(y/x)$) [20]. The parabolic quantum number, k, labels the eigenstates $|nkm\rangle$ in the Stark basis, where the first-order diagonal elements of the Hamiltonian are,

$$E = -\frac{1}{2n^2} + \frac{3}{2}Fnk. \tag{1.2}$$

In general $k = -n+1+|m|, -n+3+|m|, ..., n-3-|m|, n-1-|m|$. The eigenfunctions $|nkm\rangle$ form a complete set, and the transformation between these basis states and the well-known

angular momentum states $|nlm\rangle$ is accomplished with the following formula:

$$|nkm >= \sum_l a_{l,k}|nlm\rangle \tag{1.3}$$

$$a_{l,k} = (-1)^m \sqrt{2l+1} \begin{pmatrix} 1/2(n-1) & 1/2(n-1) & l \\ 1/2(m+k) & 1/2(m-k) & -m \end{pmatrix},$$

where the coefficient $a_{l,k}$ is calculated using a $3-j$ symbol.

Much more about the Stark effect could be mentioned at this point, but we present the information here as only the few points and definitions pertinent to the rest of thesis. Aspects of Rydberg atoms excited in static-electric fields are investigated in a few of the body chapters of this thesis, as well as in Appendix A, so further details are reserved until the discussions in these studies.

1.4 Wave-Packets

An ultra-short pulse laser has a broad bandwidth of coherent laser frequencies. Typically, the bandwidth of the ultra-short pulse laser used in the experiments presented in this thesis is $20nm$, with a central wavelength of $782nm$. In general, a short pulse laser is useful for exciting a Rydberg wave-packet since several frequencies in the laser's bandwidth may be resonant with Rydberg states. For example, $391nm$ (central wavelength) short-pulse light, usually generated by frequency doubling short-pulse $782nm$ laser light in a $1mm$ potassium dihydrogen phosphate crystal, will simultaneously populate Calcium d-states with $n = 28-35$. The coherent excitation of several Rydberg states like was just described creates a radial Rydberg wave-packet.

The interesting properties of Rydberg atoms discussed in section 1.2 are largely applicable to radial wave-packets as well. However, the energy of the bound state is no longer precisely defined, and as such, other interesting properties, for example the Kepler period, are not

precisely defined either. Still, the Kepler period of a wave-packet is $\tau_K = 2\pi n_{ave.}^{*3}$, where $n_{ave.}^{*}$ is the average principle quantum number of the wave-packet's constituent states [21]. When a short pulse laser has several frequencies in resonance with several Rydberg energy levels, and its pulse width is also shorter than the Kepler period at the given transition energies, a radial wave-packet is excited. A picture of a radial wave-packet, as a function of time, is that initially the laser pulse excites the electron to a superposition of n-states. In the initial excitation, the electron is localized at small r, but the localized wave-packet expands outward to large r, until it eventually reflects from the Coulomb potential at its maximum radius. After reflection from the Coulomb potential, the wave-packet continues to execute periodic radial motion with the characteristic timescale τ_K. When n is large, such that the correspondence principle is applicable, the localized wave-packet is analogous to the picture of a classical electron [21].

As well, other types of wave-packets may be excited, such as a Stark wave-packet, which is a coherent superposition of Stark states. A Stark wave-packet oscillates at the Stark frequency, $\omega_S = 3Fn_{ave.}^{*}$ [21], in a static-electric field of magnitude F. The Stark frequency is the precessional period of the wave-packet's angular momentum, which is not a conserved quantity, since the static electric field applies a torque to the electron, $\dot{\vec{L}} = -\vec{r} \times \vec{F}$. Similar to how the energy level spacing between Rydberg states yields the Kepler frequency, the Stark frequency is the difference in energy between Stark shifted states, with energies given by Eq. 1.2. If the short-pulse laser that excites a Stark wave-packet has sufficient bandwidth to also excite multiple n-levels, the Stark wave-packet also oscillates at the Kepler frequency, $\omega_K = 1/n_{ave.}^{*3}$.

Discussions of wave-packets are found throughout this thesis, but especially in the investigations of Stark wave-packet dynamics found in Ch. 3.

1.5 Pump-Probe Experiments

While the experiments in this thesis are varied, one aspect they all share is that they are pump-probe experiments. In these experiments, lasers are used to "pump" electrons into Rydberg, or if driven in the presence of a static-electric field, Stark states. The process of "pumping" enables reproducible production of the electronic states that are studied experimentally.

To study the electronic states, a "probe" pulse is applied. Probing the atoms necessarily destroys the electronic state, enabling detection of the charged particles (electrons or ions) produced by ionization. Usually, states are sensitive to the magnitude and frequencies of the probe pulse, so although not every electronic state is destroyed by a probe pulse, it is certainly true that if a charged particle is detected, the electron has been ionized. Often, as in the case of experiments presented in the subsequent chapters, the probing process is just as interesting as the electronic states that are probed.

1.6 Structure of the Thesis

This thesis is organized into seven chapters, including this one. Ch. 2 describes the experimental apparatus used for various experiments presented in this thesis. Ch. 3 describes a study of the dynamics of two-electron atoms in a static-electric field. This experimental study uses a technique called scaled energy recurrence spectroscopy [17], which is explained in the body of the chapter.

Chapters 4- 6 involve the half-cycle pulse as a probe of atomic systems. Ch. 4 describes how short-pulse terahertz radiation, referred to as a half-cycle pulse, is generated and characterized in the laboratory. Additionally, impulsive momentum retrieval [5] is introduced. Ch. 5 concerns a study of Stark states using a highly-accurate impulsive momentum retrieval

technique. Ch. 6 discusses additional HCP ionization experiments and further explores the use of HCP's for probing Rydberg electrons, specifically addressing the applicability of the techniques used in Ch. 5 to a broader range of atomic systems.

During the investigations into the classical aspects of electrons in static-electric fields, viewed in momentum space, it was found numerically that there are forbidden regions in the electronic probability distributions. Aspects of this result are discussed in Appendix A.

Finally, concluding remarks are presented in Ch. 7.

Chapter 2

Experimental Set-Up

2.1 Introduction

Several experimental tools are utilized in the projects presented in this thesis. In this chapter many of the general apparatus are described, the lab environment, vacuum systems, atomic sources, electronic pulses, detection electronics, and, last, but certainly not least, the laser systems utilized. The production and characterization of ultra-short pulse terahertz radiation is deferred to Ch. 4. Experimental elements common to all of the experiments discussed in this thesis are introduced in the following sections.

2.2 Lab Environment

A controlled laboratory environment is key to the success of experiments. The laboratory has many design features to help maintain a clean environment. A separate shop area is used for soldering, working with mechanical parts, oils and chemicals. A fume hood in the shop area is used for all procedures involving aromatic chemicals and hazardous materials classified by the University standards (see http://keats.admin.virginia.edu/home.html).

To ensure their proper operation and prevent damage, optics must be kept clean, ie. oil- and dust-free. Optics should be kept on the optical benches, or in drawers in the designated optics supply counter. Plastic curtains are used over the large optical table to keep dust off and to help regulate the table's temperature. Fans mounted above the table force filtered air down onto the optics bench: blowing dust off the table.

The optical tables provide a stable surface for mounting optics and lasers. For precision measurements using lasers and optics, two common problems that must be addressed are mechanical oscillations and temperature variations. Aiding in this regard, we use Newport RS 3000 optical tables that are designed to damp mechanical vibrations. Air conditioners maintain the laboratory at a consistent temperature, typically $72°F$. The ultrafast laser system (see Sec. 2.8) located on 5 joined optical tables, has additional temperature regulation. A heater/temperature controller provides heat to the optical table, regulating the temperature at $74°F$ with a $\pm 1°$ accuracy. The laser system seems to work most stably at night, though it is unclear if this is due to the lack of activity in the building most nights or if it is a temperature issue. However, the effect is dramatic and makes conducting sensitive experiments at night well-worth the loss of sleep.

2.3 Vacuum System and Atomic Sources

Laser/atom interactions described in this thesis are studied in vacuum chambers. Laser light enters the vacuum chamber through glass view ports. Glass absorbs in the ultraviolet [34], so quartz windows are used when UV laser light is coupled into the chamber. Voltage feed throughs are used to couple electronic signals into and out of the chamber.

The chamber pressure is maintained below $10^{-6} Torr$ by a Varian VHS-6 diffusion pump. The pump and chamber pressures are monitored and interlocked to prevent hazards associated with high-vacuum systems, the atomic sources, and the high-voltages often used in the

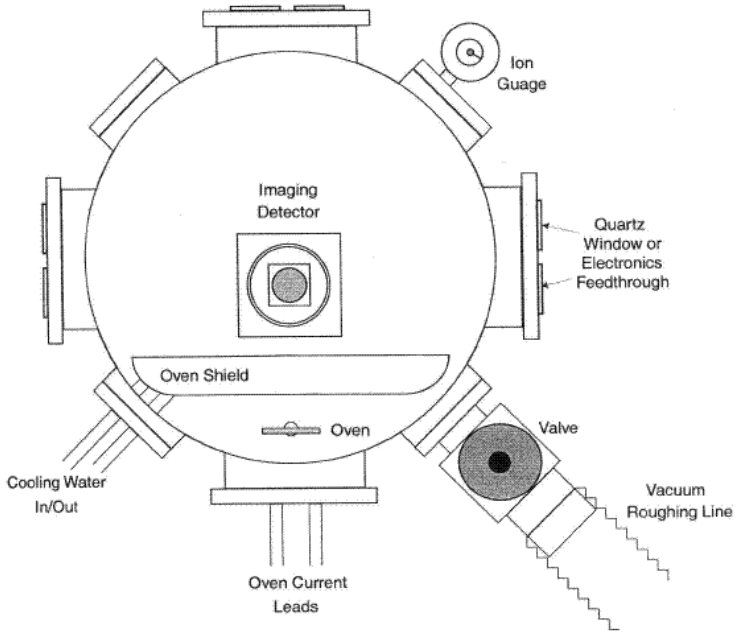

Figure 2.1: Vacuum Chamber schematic [31].

chambers. The interlock system protects both lab users and lab equipment. The diffusion pump's foreline is backed by a mechanical pump, that maintains the foreline pressure well-below $10^{-1}Torr$. To ensure that equipment is not damaged (microchannel plates, phosphor, and other electronics inside the chamber) the vacuum pressure is kept below $4 \times 10^{-6}Torr$ when using high-voltages.

A thermal beam of ground state atoms (Ca or Ba in experiments discussed in this thesis) is produced by the oven inside the chamber. The oven is made of a 6" long, 3/8" diameter stainless steel tube with a $1mm$ diameter exit-hole drilled in the side. The tube is crimped at the bottom, filled with Ca or Ba shot to $1mm$ below the exit hole, then crimped at the top. The tube, a so-called oven, is mounted inside the chamber with the exit-hole facing the interaction region, defined in a very general way for right now, as the region of the vacuum chamber where atoms are exposed to static and/or pulsed fields. The oven current leads connect to the tube's top and bottom crimps.

The oven current leads are connected across a series of transformers that supply up to $110A$ of current at $6VAC$. The current is regulated by a Variac AC voltage regulator. The oven has a small resistance (0.1Ω) and the power dissipated in it Ohmically heats the Ca or Ba raising its vapor pressure. Typical currents used in experiments are $50 - 70A$. Higher currents may be used to increase atomic signal, however temporary fluctuations in the amount of atoms produced may also result. The heated vapor of atoms leaves the oven through the exit-hole, which is aligned with a small hole in a water-cooled copper oven shield, approximately $5cm$ away. The shield hole and exit-hole of the oven define the axis of the thermal beam of atoms. Typical atomic beam densities $10cm$ away from the oven are $10^7 - 10^8 atoms/cm^3$ [31].

2.4 Interaction Region and Ion Detection

Ground state Ca and Ba atoms are excited with nanosecond dye lasers (see section 2.7) to Rydberg states in the interaction region. The interaction region is defined by two parallel $7.5cm \times 7.5cm$ aluminum plates separated by $2cm$. Atoms and lasers interact in the center of the parallel plates, underneath a $25mm \times 2mm$ slit in the top plate. As well, through the application of AC or DC voltages to the aluminum plates, the atoms interact with pulsed or static-electric fields. Specifically, in the experiments presented in the following chapters, Rydberg atoms are excited in static-electric fields, producing Stark states that are subsequently studied as atomic systems. In addition to using electric fields to produce bound states, electric fields are also used to ionize Rydberg states and to accelerate ions, toward or away from the detector.

The detector electronics are a pair of image quality microchannel plates (MCPs) backed by a phosphor anode. The $1.5mm$ diameter MCPs are charged particle detectors. Ions projected through the slit in the top field plate create an electron cascade typically producing

multiple electrons for every ion event at a given time and position. In total, two MCPs are used, where for detecting ions the top plate is grounded and the bottom plate is usually biased at $-1500V$. Electrons are accelerated toward the $4000V$ biased, $3cm^2$ phosphor screen, causing position sensitive fluorescence. A CCD camera, located outside of the vacuum chamber images the phosphor screen through a plexiglass window, and a frame-grabber records the position dependent florescence. Care must be taken to ensure that the recorded signal level is linearly dependent on the number of ions present. In experiments presented in this thesis, the ion signal is proportional to the intensity of the Rydberg-state-producing second dye laser, so neutral density filters are used to attenuate of the second dye laser's light, and ionization levels are reduced accordingly. A photodiode is used to check the neutral density filter's attenuation factor for the given frequency of laser light.

The imaging detector just described is useful for making position sensitive measurements [22] [18]. In experiments where ultrafast beams counter propagate under the top-plate slit, time-dependent information is encoded into the spatial coordinate. For an example of this type of measurement see Ref. [23]. In other experimental set-ups, the spatial coordinate is used to encode other parameters, eg. electric field strength in Refs. [22, 18], and the experiments presented in subsequent chapters of this thesis.

2.5 Voltage Supplies

Several voltage supplies are used in experiments presented in this thesis, where the source is usually chosen to fulfill specific experimental requirements. Specifically, as mentioned in the previous section, voltages applied to the parallel plates produce electric fields in the interaction region. Additionally, voltage supplies are used to induce birefringence in Pockel's cells, power detector electronics, and generate HCPs. Many of the voltage supplies used in experiments presented here are commercially obtained. One type of pulsed voltage supply

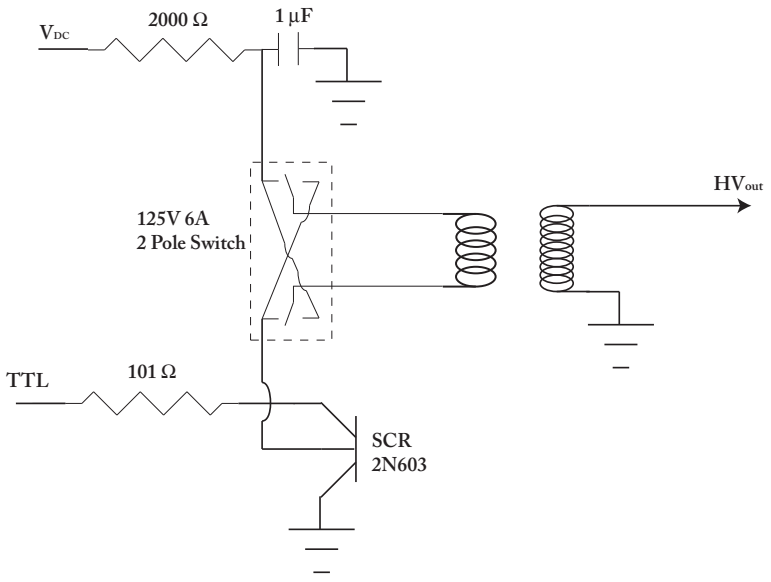

Figure 2.2: Circuit diagram for a voltage pulser, sometimes referred to as a field pulser. A $5V$ trigger, labeled TTL, determines when the high-voltage (HV) pulse is applied. When the TTL is applied there is conduction between the anode(middle pin) and the cathode(bottom pin) of the SCR. The 2 pole switch controls the polarity of the pulse. In one position voltage is applied to the primary, and the secondary of the transformer is grounded when the TTL is applied to the SCR. In the other switch position, the secondary is biased and the primary is grounded when the TTL is applied.

that is built in the lab is the so-called field pulse box. The circuit diagram for a field pulse box is shown in Fig. 2.2. This circuit uses a transformer to produce a high-voltage. Typically, using a car transformer, up to about a $8kV$-peak pulse is applied to the GaAs wafer in the HCP ionization experiments in Ch. 5 and Ch. 6. In general, higher peak-voltages can be generated by the field pulse box. The characteristic width of a pulse generated by the field pulse box is dependent on the electronic components used. Specifically, for the previously mentioned car transformer, the pulse width is about $50\mu s$. With a faster transformer high-voltage pulses with widths of a few microseconds are achieved.

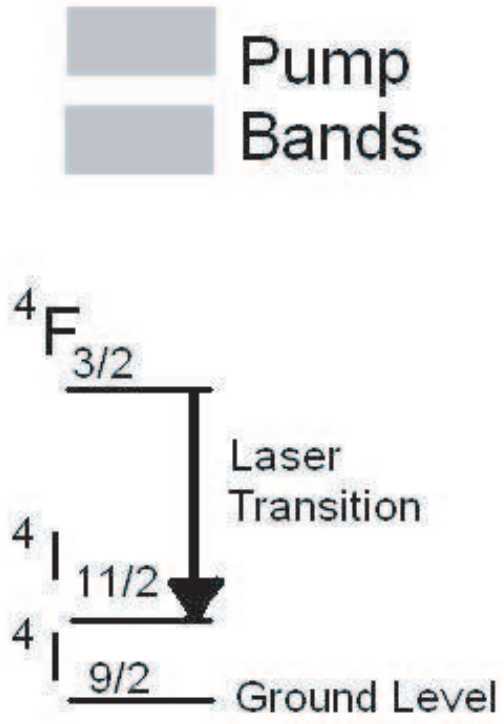

Figure 2.3: Energy level Scheme for the Nd^{+3} Ion [26].

2.6 Solid State Lasers

Solid state (eg. $Nd:YAG$) lasers are reliable and commercially available. These characteristics make $Nd:YAG$s the work-horse laser of many labs, including our own, where they optically pump other lasers and amplifiers in the experiments presented in this thesis. Three different types of solid-state lasers are used: the Coherent Surelight II, Spectra-Physics Quanta-Ray GCR, and Spectra-Physics Millennia Vs.

The Surelight and Quanta-Ray gain medium is a rod of neodynium-doped yttrium aluminum garnet ($Nd:YAG$). The gain medium is optically pumped by a high-voltage discharge through a gas tube, called a flash lamp. The flash lamp is an incoherent light source that supplies photons with a frequency that the gain medium strongly absorbs. Excited electrons in the pump-band quickly decay into the ${}^4F_{3/2}$. The laser transition is ${}^4F_{3/2} \rightarrow {}^4 I_{1/2}$

with energy corresponding to the emission of a $1064nm$ photon. Stimulated emission is sustained in a resonant laser cavity, optimized for $1064nm$ light. High-power nanosecond laser pulses are produced by Q-switching the optical resonant laser cavity, where a Q-switch is an electro-optic device used to control the laser's gain [84].

Light from the Surelight and Quanta-Ray $Nd:YAG$ lasers is often frequency doubled or otherwise mixed in non-linear crystals to produce $532nm$ or $355nm$ light. Typically, $532nm$ laser light is used to pump dye lasers producing light in the visible region, while $355nm$ light pumps dye lasers producing light in the ultraviolet. The specific colors produced by the dye lasers are dependent on the dye and frequency selected, discussed in Sec. 2.7. As well, the three harmonic frequencies of YAG light are often mixed in non-linear crystals producing frequencies of light useful for experiments. For example, $1064nm$ light mixed with $620nm$ light from a Rhodamine 640 dye laser creates $\sim 391nm$ light that is useful for Rydberg excitations in Ca. Finally, another common use of $532nm$ laser light is for ultrafast laser light amplification, discussed in sections 2.8.5 and 2.8.4.

The Millennia Vs's gain medium is neodynium-doped yttrium vanadate ($Nd:YVO_4$), electrically pumped by solid-state diodes. Since Nd^{+3} is the laser active medium, the light produced by this laser is similar to the ones described previously. However, this laser is optimized to produce very stable, high-power continuous-wave laser light. Frequency doubled light from this high-power continuous-wave laser is used as a pump source for the ultrafast laser system oscillator, discussed in section 2.8.1.

2.7 Dye Lasers

Organic dyes, often the same chemicals used in biological staining, coloring clothes, and other household products, are the gain medium for the tunable dye laser. Compared with many gas and solid-state gain mediums, dyes offer a large lasing bandwidth. Most dye-

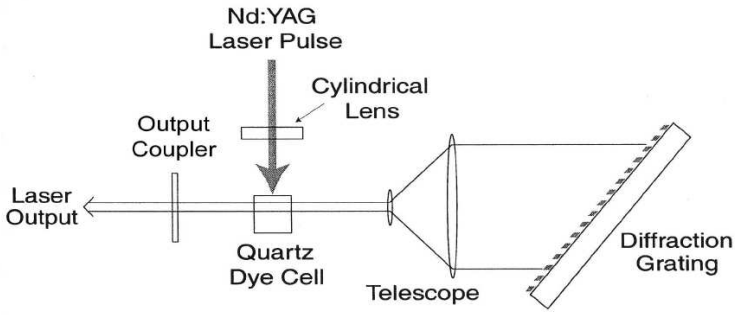

Figure 2.4: Schematic of the Hänsch-style dye laser [31].

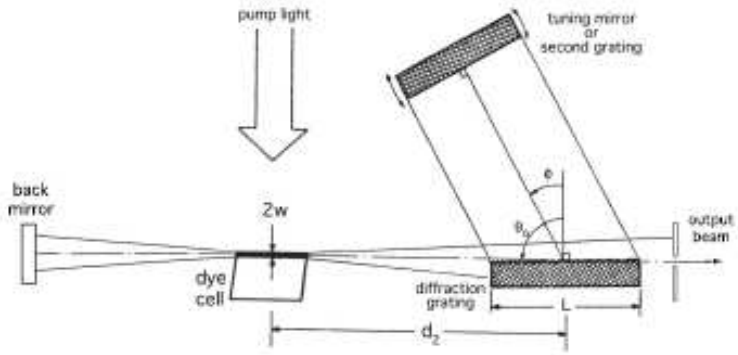

Figure 2.5: Schematic of the Littman-style dye laser [31].

lasers in the laboratory are home-made. There are two main types, the Hänsch [27] and Littman [28] designs, shown in Figs. 2.4 and 2.5 respectively. The basic materials needed to construct a dye laser are the same in both designs, a quartz cuvette, organic dye mixed in a solution, eg. methanol or 1-4 Dioxane, a circulating pump, an optical cavity (mirrors and a diffraction grating), and a pump source that drives a population inversion in the gain medium. Specifically in this thesis, the pump source is laser light from a $Nd:YAG$ laser.

In general, at least two dye lasers are used to excite Rydberg states. Specifically, for Ca, $423nm$ and $391nm$ light excites ground state atoms through an intermediate state (4s4p) to Rydberg states (4snd). $423nm$ light is produced in a dye laser where the gain medium is $0.5g/L$ of Stilbene 420 in Methanol. $394nm$ light is produced in a dye laser where the gain medium is $0.3g/L$ of Excelite 398 mixed in 1-4 Dioxane. $391nm$ light is produced by $0.3g/L$ of a 50:50 mix of Excelite 398 and Excelite 392 in 1-4 Dioxane. Care must be taken when using 1-4 Dioxane which may accumulate static charges while flowing through a circulation system, igniting itself [29]. Safeguarding against this hazard, grounded stainless steel wires are run through the circulation system providing a path to ground for any static-charge build up.

2.8 Ultrafast Laser System

Ultrafast laser light used in experiments presented in the following chapters is produced in a physically large laser system (spanning two joined $10'$ optical tables), with many different optical components. Though it is a complex system with many parts, each subsystem has a specific function, and can operate independently of the rest of the system. The subsystems are described in detail in the following sections. An overview of the ultra-short pulse production process is that $0.5W$ of $30fs$ light is produced in the oscillator. The oscillator output is sent to one of two short-pulse laser light amplifiers. One amplifier is a $30fs$ multipass

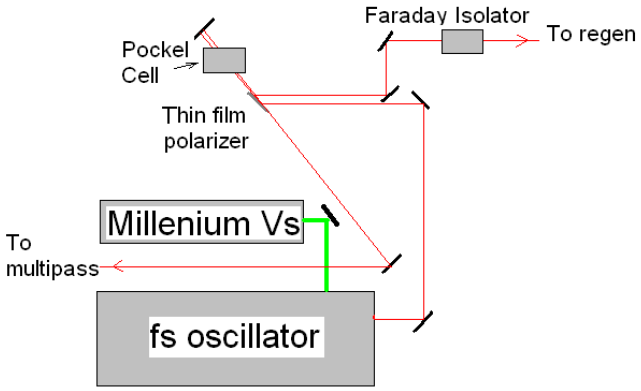

Figure 2.6: A complete diagram of the Kapteyn-Murnane Laboratories Inc. fs oscillator is in Ref. [32]. The oscillator output is a train of $30fs$ pulses separated by $11ns$. A Pockels cell switches the polarization of selected pulses, allowing them to pass through a thin-film polarizer to a multipass amplifier. Pulses not switched by the Pockels cell are reflected by the polarizer toward the regenerative (regen) amplifier.

amplifier. The other amplifier is a regenerative amplifier and multipass amplifier in series, with a $30mJ$, $\sim 100fs$ final product - experiments described in this thesis use a third of this light.

2.8.1 Oscillator

The oscillator is a commercially available Kapteyn-Murnane Laboratories Inc. model MTS Mini Ti:Sapphire Laser Kit. The oscillator is optically pumped with 3.5 W of $532nm$, cw-laser light from the Spectra-Physics Millennia Vs. Originally polarized in the vertical direction, the $532nm$ pump light is rotated to horizontal before illuminating the Ti:Sapphire crystal - the oscillator's gain medium. Ti:Sapphire has a large bandwidth, typically spanning $700nm - 1100nm$ [31], allowing for the simultaneous excitation of on the order 10^5 resonant cavity modes. Mode spacing in the oscillator is $64MHz$. One cavity mirror is a broadband high reflector, suitable for the propagation of the many longitudinal modes, and the other is a semi-transparent output coupler, also suited to broadband laser light. A pair of prisms correct for group velocity dispersion in the cavity.

Short pulses are achieved through the coherent interference of the different longitudinal cavity modes, so-called mode-locking. An initial jolt to the optics, applied by jiggling one of two dispersion correcting prisms produces an intense pulse inside the laser cavity with a specific phase relationship between the different-frequency cavity modes. The in-phase cavity modes add together coherently, creating an intense pulse. Inside the Ti:Sapphire crystal, a non-linear effect, called the optical Kerr effect self-focuses the intense pulse, preferentially amplifying the in-phase modes. The oscillator's output beam is a TEM_{00} spatial mode, short-pulse beam, with a central wavelength of $800nm$ [32].

2.8.2 Short-Pulse Laser Amplification

In general, ultrafast laser pulses have large peak intensities, so care must be taken to avoid damaging optical components during amplification. The problem of amplifying a short pulse is solved by temporally separating the pulse into its various frequency components, referred to as chirping. Each frequency component is amplified, and the chirped pulse is reassembled into a short pulse. Optical set-ups in the sections that follow are the ultrafast laser system components that chirp the pulse, amplify it, and finally reassemble it.

2.8.3 Expander

The ultra-short pulse is chirped in the expander. A grating diffracts the different frequencies of the pulse at different angles [34]. The separated frequencies travel different path lengths in the expander, specifically the redder light travels a shorter distance than the bluer light. The peak power of the expanded pulse is reduced by roughly three orders of magnitude allowing for amplification in the regenerative and multipass amplifiers.

In addition to chirping the pulse, the expander is used to select the central wavelength of the laser light. The motivation for selecting the pulse's central wavelength is that certain

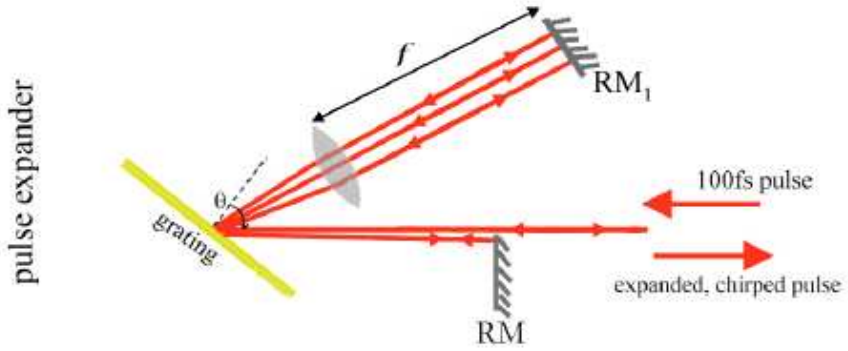

Figure 2.7: Short pulse expander [30]. A diffraction grating and lens spatially separate a broadband short pulse into its different frequency components. Mirrors, RM and RM_1, retroreflect the light off of the grating a total of 4 times. Spatially separated frequency components travel slightly different path lengths in this optical arrangement yielding as the output of the expander, a chirped pulse where the higher frequencies are delayed in time relative the lower frequencies.

experiments use the short-pulse light to drive transitions that require a specific frequency. Central wavelength selection is achieved in the expander by selecting the angle of the grating, labeled θ in Fig. 2.7. In experiments presented here $\theta = 54°$. As well, a razor blade positioned in front of RM, acts a spatial filter, attenuating the light corresponding to the $800nm$ portion of the spectrum as it is projected on RM. Recall that $800nm$ is the central wavelength of the oscillator. A Jarrell Ash MonoSpect 18 monochrometer is used to align the razor blade, and verify that the spectrum of the expander output is attenuated gradually, rather than abruptly truncated, and has a central wavelength of $780nm$.

2.8.4 Regenerative Amplifier

The regenerative amplifier (regen) is itself a laser cavity that acts as an amplifier for the frequency-chirped laser light, referred to as the seed pulse. The regen has a Ti:Sapphire crystal, gain medium and cavity mirrors, M1 and M2 in Fig. 2.8. The Ti:Sapphire crystal is pumped by $590mW$ of $532nm$ light from a Spectra-Physics Quanta Ray GCR. The $10ns$ pump light creates a population inversion in the Ti:Sapphire crystal that has a characteristic

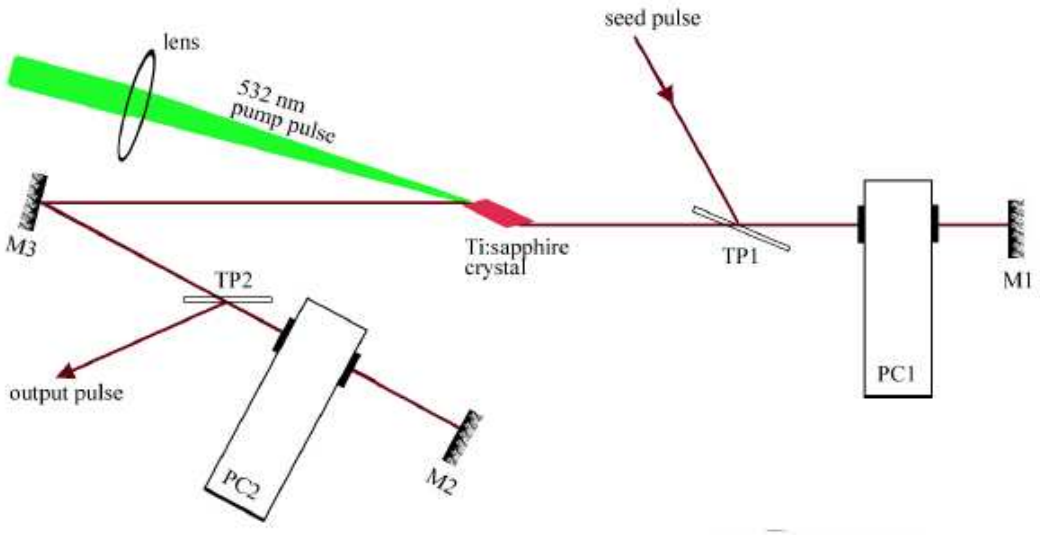

Figure 2.8: Regenerative amplifier (regen) [30]. A Ti:Sapphire crystal is optically pumped providing a gain medium for the chirped pulse output of the expander. The chirped pulse sweeps the gain typically about 20 times in the regen cavity. Thin-film polarizers and Pockels cells enable pulse switching in to and out of the cavity.

time-scale of $3.8\mu s$ [33]. Thin film polarizers (TP1 and TP2 in Fig. 2.8) and Pockels cells (PC1 and PC2) are used to both couple the seed pulse into the regen cavity and the amplified laser pulse out. The incoming seed light is vertically polarized, and the thin film polarizers reflect vertically polarized light while allowing horizontally polarized light to pass through. High-voltage pulses applied to the Pockels cell cause them to rotate the polarization of light in the cavity by 45°. When voltage is applied to PC1, the seed light is switched into the cavity. The light is amplified in the cavity for roughly $200ns$, completing several passes through the gain medium before a high-voltage pulse is applied to PC2, the light's polarization is rotated by 90° and the light is reflected out at TP2. A total of about 20 round trips in the regen cavity amplifies the light by a factor of 4×10^6.

Unfortunately, the regen has dispersive components that do not allow for equal amplification of all frequencies in the seed light. This dispersion modifies the output pulse's bandwidth, a point that is discussed further in the next section. The most dispersive elements in the regen are the thin film polarizers, mirrors, and wavelength dependent coatings.

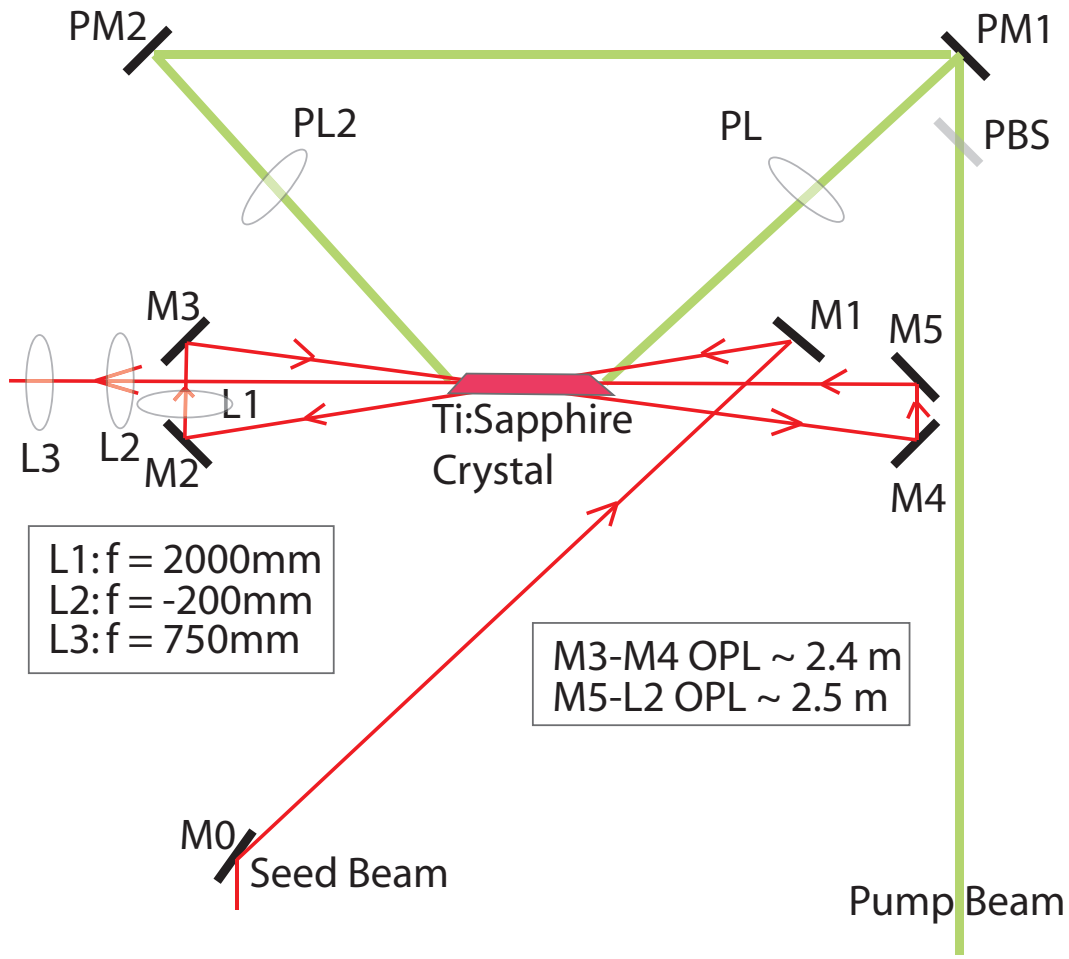

Figure 2.9: Multipass amplifier. The Ti:Sapphire crystal is optically pumped with $532nm$ YAG light focused by lens PL1 and PL2. Upon exiting the regen cavity, the seed light sweeps out gain on every pass through the pumped Ti:Sapphire crystal, resulting in a factor of 5 amplification at the multipass output.

2.8.5 Multipass Amplifier

In the multi-pass amplifier (multi-pass), like in the regen, $532nm$ light from a Spectra-Physics Quanta Ray GCR is used to pump a population inversion in a Ti:Sapphire crystal. The chirped-pulse exiting the regen passes three times through the pumped Ti:Sapphire crystal sweeping out gain. The multi-pass optics are arranged in a bow-tie pattern and the set-up is fairly straight forward. Typically, amplification by a factor of 5 is produced in the multi-pass. The amplification factor is a function of the $Nd:YAG$ pump power and can be

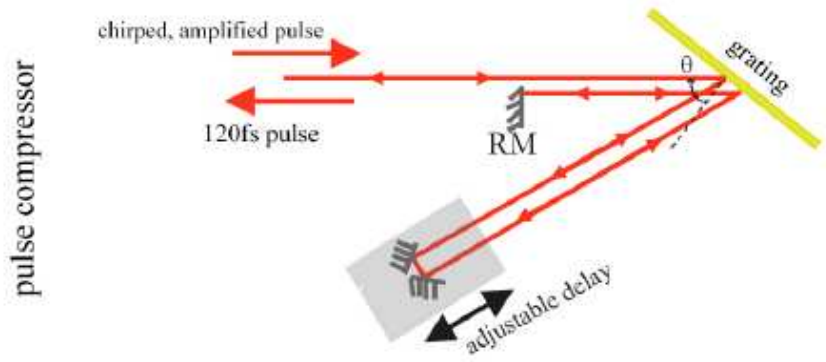

Figure 2.10: Compressor [30]. The chirped frequency components are put back together, temporally, in the compressor. The amplified, chirped pulse is diffracted from a grating a total of 4 times, through the use of a retro-reflecting mirror (RM) and two mirrors mounted on a translational stage, providing an adjustable delay.

higher, up to a factor of 10 times.

In the multi-pass, the mirrors and lenses are dispersive elements. Together then the multi-pass and regen amplifiers reduce the bandwidth of the amplified laser light, and consequently lengthen the duration of the pulse produced by the ultrafast laser system. Regardless, pulse widths are still sufficiently short for the experiments presented in this thesis, and the remarks on the regen and multi-pass amplifier's dispersion only serves to explain why the ultrafast laser system's pulse width is typically about 5 times longer than the oscillator's pulse width.

2.8.6 Compressor

The compressor undoes the chirp introduced by the expander, constructing an ultra-short laser pulse from the amplified chirped pulse. The compressor is aligned with $\theta = 54°$ to match the chirp introduced by the expander. A delay stage allows for adjustment of the various frequency components' relative path lengths. Fine-tuning of the relative path lengths is achieved with this adjustable delay control and through real-time monitoring of the pulse width using a single-shot autocorrelator discussed in Sec. 2.8.7. In experiments presented in subsequent chapters, the output of the compressor is a $100 fs$ ultrafast pulse.

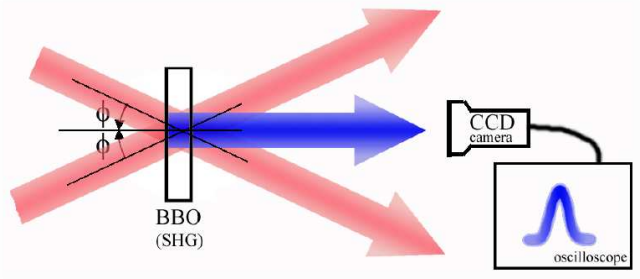

Figure 2.11: Single-Shot Autocorrelator [30]. Identical beams of ultrafast laser light intersect, both spatially and temporally, in a non-linear crystal (BBO). Phase-matching inside the crystal allows for second harmonic generation (SHG), producing SHG light proportional to the ultrafast pulses' temporal overlap at a given position. The SHG intensity profile is monitored with a CCD camera and oscilloscope, to characterize the ultrafast laser's temporal pulse shape.

2.8.7 Short-Pulse Laser Characterization

The challenge of characterizing the temporal pulse shape of a femtosecond laser is that electronic detectors generally do not have a fast-enough response time. This challenge is overcome through the use of autocorrelation techniques. In general an autocorrelation is performed by generating two identical ultrashort pulses, eg. in a standard Michelson interferometer [34] or in the single-shot autocorrelator, Fig. 2.11, and then sending both pulses through a non-linear doubling crystal [34], BBO in Fig. 2.11. When the pulses are overlapped simultaneously in the crystal, the resulting intensity of both pulses is large enough to induce second harmonic generation (SHG). In a Michelson interferometer the delay of one pulse may be scanned relative to the other pulse, and the intensity of SHG light is a function of the relative delay between the pulses. In the single-shot autocorrelator, where the identical beams are spatially overlapped inside the non-linear crystal, and their spot sizes are large enough that the overlap is homogeneous, the relative time delay between the two pulses is scanned as they intersect at an angle of 2ϕ, and information about the pulse-widths is encoded into the SHG spatial beam shape. We define the longitudinal width of a pulse of light, ΔL, as the distance between the original pulse's leading and trailing edge. Inside the non-linear crystal,

with index of refraction n, $\Delta L = c\Delta t/n$, where c is the speed of light, and Δt is the pulse duration. The intensity of the SHG light is monitored with a CCD camera and oscilloscope. The width of the intensity of the SHG, as a function of position, is proportional to ΔL. The spatial intensity variation of the SHG is calibrated to the ultra-short pulse duration by inserting a glass slide into one beam path of the two identical beams. This results in a longer optical path length for one beam, and in a spatial translation of the SHG profile, since the two beams now simultaneously overlap at a different spatial position inside the BBO crystal. The temporal delay is $t_d = (n_0 - 1)d_0/c$, where d_0 is the width of the glass slide and n_0 is the index of refraction in the microscope slide. Typically a glass microscope-slide coverslip with $d_0 = 0.15mm$, results in an optical-delay of $280fs$. Measurement of the SHG profile shift for this known delay, determines the scale of the SHG spatial intensity profile in units of time.

Chapter 3

Two-electron orbital dynamics in a static-electric field

3.1 Introduction

An alkaline-earth atom in a static-electric field provides an interesting laboratory for studying two-electron orbital dynamics. To a good approximation we may consider the classical picture of the singly-excited Rydberg electron [16]. This electron, excited in a static electric field, is launched onto an elliptical trajectory with a Kepler period of $\tau_K = 2\pi n^3$, where n is the principle quantum number. As illustrated in Figs. 3.1 and 3.2, the electric field torques the semi-major axis of the elliptical orbit causing the orbital angular momentum to precess with a characteristic Stark period, $\tau_S = 2\pi/3Fn$, where F is electric field strength.

Scaled-energy recurrence spectroscopy (SERS), originally introduced by Eichmann *et al.* [17], is a technique for revealing the semiclassical dynamics that underly complex energy spectra. The method has been used in conjunction with closed-orbit theory [35], to explore the behavior of singly-excited Rydberg atoms in the presence of strong electric and/or magnetic fields [1-13]. For singly-excited atoms in static-electric fields, SERS typically reveals the

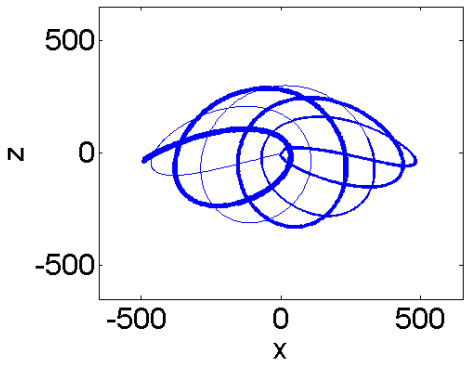

Figure 3.1: Trajectory of an electron launched into a static-electric field ($F = 5000V/cm$) with initial conditions $n = 18$ and $l = 0$. The line-width is proportional to time, where the narrowest line is $t = 0$ and the widest line is $t = 2\tau_S$.

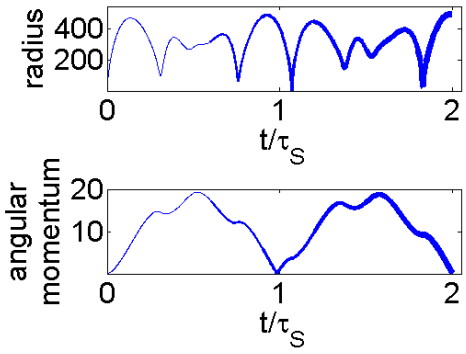

Figure 3.2: radius and magnitude of the angular momentum vector plotted as a function of time for the electron in Fig. 3.1. Oscillations corresponding to both the Kepler and Stark periods are observed.

Kepler and Stark periods. For non-hydrogenic Rydberg electrons, the dynamics are further complicated by scattering from the ion core. SERS also reveals the time scales associated with scattering between uphill and downhill orbit configurations in non-hydrogenic atoms.

Given the success in applying these experimental and computational methods to single-electron systems, it is desirable to consider if similar frequency domain methods can be used to explore two-electron dynamics in the presence of external fields. Two-electron interactions introduce a new characteristic time-scale, the configuration interaction time, τ_{CI} [50, 41], associated with scattering between singly- and doubly-excited configurations. Yet in spite of the fact that a number of previous experiments have focused on two- or multi- electron systems [40, 41, 42, 43, 44, 45], only one experiment in Ba [41] has utilized SERS to focus exclusively on the role of configuration interaction in Stark dynamics within multi-electron atoms. Bates *et al.* [41] used direct laser excitation of the $5d7d\ ^1D_2$ perturber which is embedded in, and coupled to, the singly-excited $6snd$ Rydberg series in Ba. SERS and direct Fourier transform spectroscopy were used to interpret absorbtion spectra collected as a function of binding-energy and electric field strength. Bates *et al.* observed a clear increase in

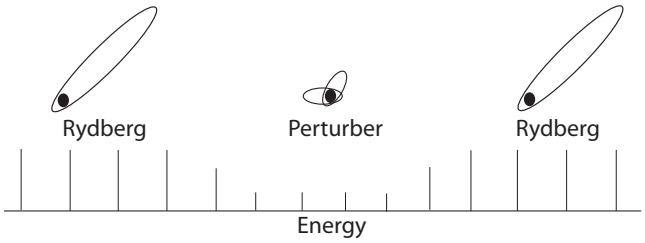

Figure 3.3: Schematic diagram of a perturbed Rydberg series. The double-valence perturber is embedded in the single-valence Rydberg series, causing oscillator strength and quantum defect variations.

the fundamental Kepler period compared to what is observed in single electron systems. They attributed this longer period to both the time-lag associated with electron scattering back and forth between doubly-and singly- excited configurations and to an increased anharmonicity in the effective binding potential at energies near the perturber. Unfortunately, the range of electron binding energies that could be explored was restricted to the width of the $5d7d$ perturber. Thus, the achievable time resolution was limited to the inverse of the resonance width, i.e. comparable to the time shifts that were inferred.

In this chapter, we examine Stark dynamics in the presence of strong configuration interaction from the Rydberg electron rather than valence electron perspective. We directly excite the Ca $4snd$ and Ba $6snd$ Rydberg series and record photoabsorption maps as a continuous function of electric field and electron binding energy. Embedded (see Fig. 3.3) in the Rydberg series of Ca and Ba are the $3d3d$ [46] and $5d7d$ [51] perturbers, respectively. We explicitly compare and contrast the scaled-energy recurrence spectra obtained from different energy regions within the Stark maps, i.e. regions within or near the doubly-excited resonances and regions not strongly influenced by these perturbers. This analysis provides a clear picture of the two-electron dynamics and allows us to characterize the general effectiveness of scaled-energy recurrence spectroscopy in revealing those dynamics. Ultimately, these methods and their extensions, might be profitably applied to more complex spectra in

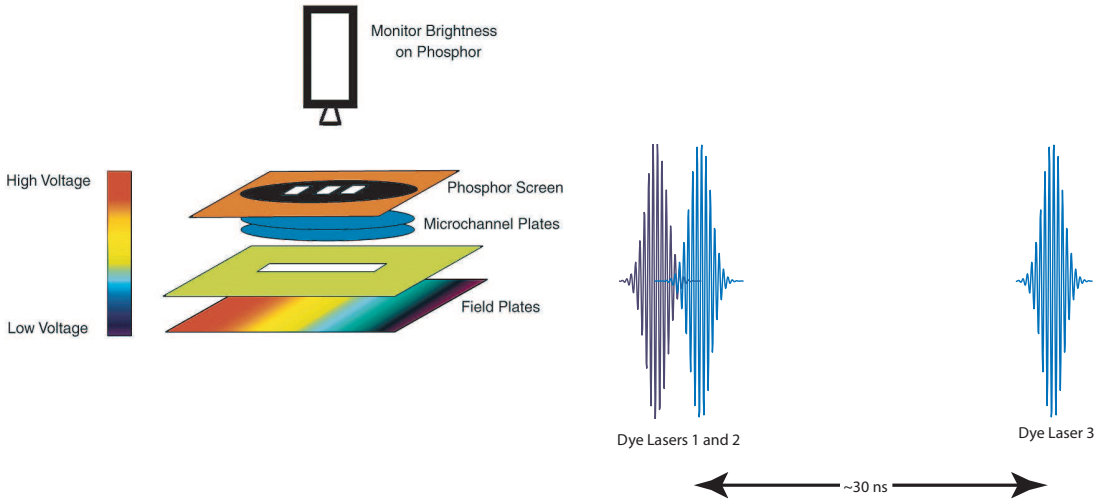

Figure 3.4: Two nanosecond dye lasers perform the excitation in a static-electric field. The inhomogeneous static electric field is produced by 12 individually biases wires 1.5mm below an aluminum plate. A third dye laser provides ionization proportional to photoabsorption probability as a function of the second laser's frequency, and the position dependent electric field strength. Ionization is monitored with the imaging detector (MCP, phosphor, and CCD camera).

multi-configurational atoms and molecules as a probe of the underlying classical dynamics.

3.2 Experimental procedures

3.2.1 Apparatus

The experimental apparatus has been described previously [22]. A schematic of the experiment is shown in Fig. 3.4. Alkaline-earth atoms, Ba or Ca, in a thermal beam are laser excited in a spatially inhomogeneous static electric field. Stark spectra are recorded as a continuous function of Rydberg energy and electric field strength, then transformed into scaled-energy recurrence maps.

Both Ca and Ba are studied providing two different systems to probe perturbations within Rydberg series. The thermal beam of atoms is produced by a resistively heated oven, described in Ch. 2. When Ca is studied the oven is filled with 99% Ca shot, and when Ba

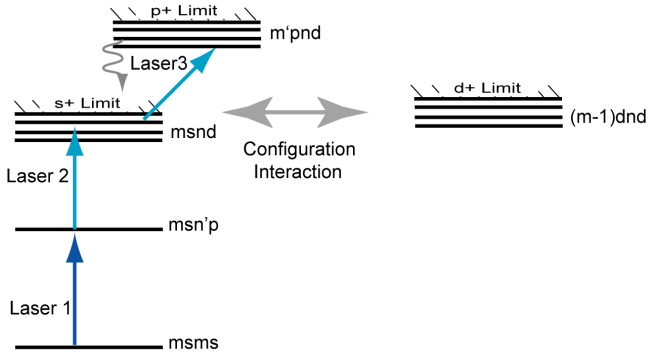

Figure 3.5: General excitation scheme. Ground state Ba or Ca atoms are excited into $msnd$ Rydberg states, which interact with double-valence $(m-1)dnd$ states. Laser 3 excites farther to an autoionizing state that decays rapidly, causing an ionization current proportional to the number of atoms in the $msnd$ states.

is studied the oven is filled with 99% Ba solids. Additionally, the dye lasers used for the excitation are different for the two different atomic species. In general though, as illustrated in Fig. 3.5, the atomic species are excited by dye laser 1, to an intermediate state. Next, in a static-electric field, dye laser 2 drives transitions to the highly-excited Stark states. Specifically, for Ca, dye lasers with wavelengths 422 nm and $391-395$ nm drive the transitions $4s4s\rightarrow 4s4p\rightarrow 4snd\ ^1D_2$ with $13 < n < 24$. For Ba, the excitation $6s6s\rightarrow 6s6p\rightarrow 6snd\ ^1D_2$, where $14 < n < 50$, is performed using two dye lasers with wavelengths of 554 nm and $420-430$ nm. Relative frequency calibration to better than 0.3 cm^{-1} is achieved by monitoring the transmission of the second laser through a 2 mm etalon. The absolute frequency of the second laser is established to an accuracy better than 1 cm^{-1}, using the known positions of nd Rydberg states in zero-field [46, 51]. The laser/atom interaction region is 12 parallel wires in a horizontal plane, 1.5 cm below an aluminum plate. The wires are spaced 2 mm apart, and connected to neighboring wires by $475k\Omega$ carbon-film resistors. The magnitude of the electric field gradient in the interaction region is a function of the voltages applied to the two ends of the wire/resistor chain. The frequency of dye laser 2 is scanned with fixed voltages applied across the ends of the resistor chain. For example, in the Ca experiments, voltages $0kV$, $2kV$, and $4kV$ were applied in sequential scans, with the

other end of the resistor chain at ground. Higher voltages were also applied in sequential scans, $6.5kV$ and $8.5kV$, with the low-voltage side at $2.5kV$ and $3.5kV$ respectively. The voltage difference across the wire/resistor chain is always less than 5 kV, to ensure electric field gradient linearity and minimize non-vertical field components. Calculations of the field plate geometry, using SIMION software to solve the electrostatic boundary value problem indicate that magnitudes of the horizontal field components are always less than 5% as large as the vertical field components.

Ten nanoseconds after the Rydberg excitation, a third dye laser excites electrons to an autoionizing state, producing an ion current proportional to the number of Stark atoms present. In Ca, 393 nm photons saturate the $4s^+ \rightarrow 4p^+_{3/2}$ transition. In Ba, the $6s^+ \rightarrow 6p^+_{3/2}$ transition is saturated with 455 nm photons. Ions produced at different locations within the spatially inhomogeneous electric field are projected through a 2 $mm \times 25$ mm slit in the upper plate, onto a MCP detector backed by a phosphor anode. Following each laser shot, position dependent fluorescence from the phosphor is imaged by a CCD camera, and recorded using a frame-grabber and HL Image data collection software.

For each laser scan at a fixed voltage, a calibration scan is performed, at the same fixed voltage, but without the third dye laser. In this scan, for field strengths $F > 1/16n^{*4}$ [16], the electron becomes unbounded by adiabatic field ionization. Electric field strength versus position is calibrated by finding, as a function of laser frequency, the position of the static-electric-field ionization threshold.

Complete Stark maps are composites of the laser scans taken over several ranges of electric field strength, and are shown for Ba and Ca in Figs. 3.6 and 3.7 respectively.

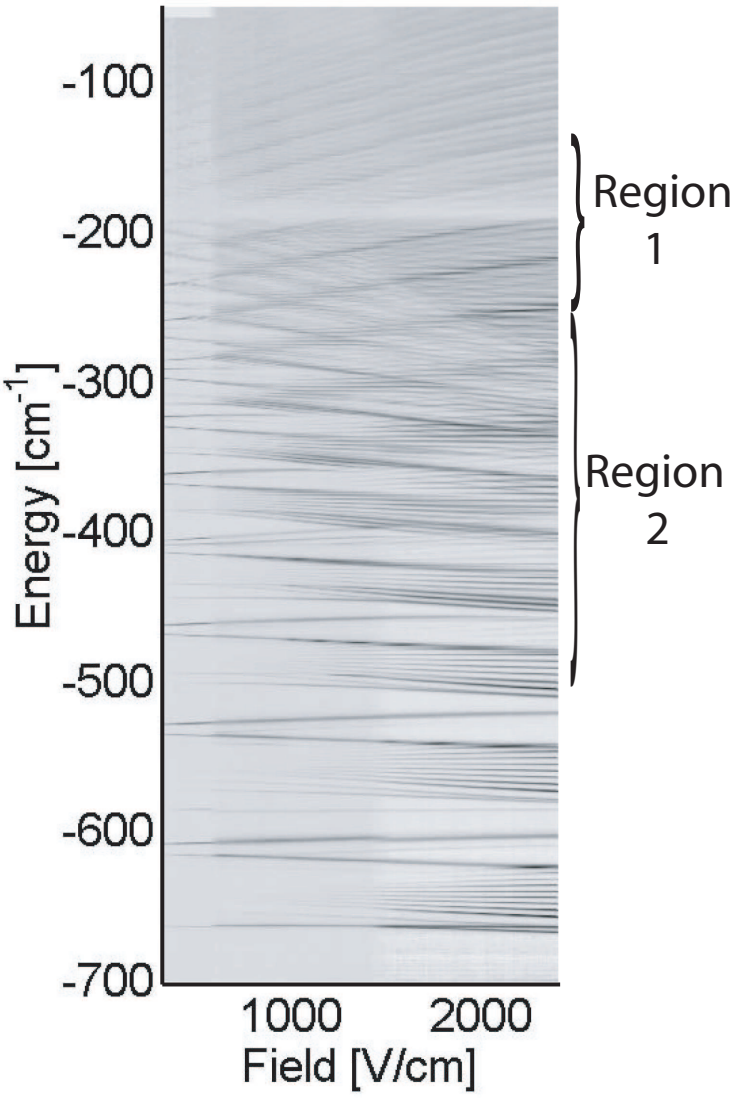

Figure 3.6: Density plot of the measured Ba Stark map. Large photoabsorption probability is shown as dark regions. The attenuation of the photoabsorption probability near $E = -194$ cm^{-1} (Region 1), is due to the $5d7d\ ^1D_2$ perturber. States at lower energy (Region 2) are not strongly coupled to the perturber.

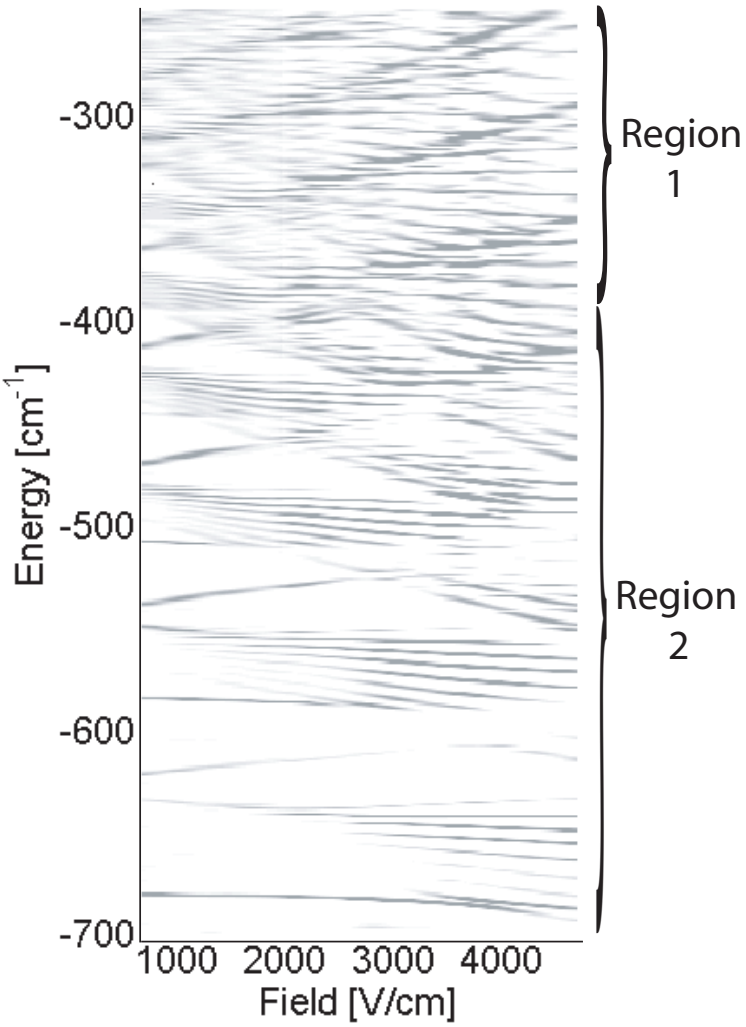

Figure 3.7: Density plot of the measured Ca Stark map. Large photoabsorption probability is shown as dark regions. States in Region 2 are strongly coupled to the $3d3d$ perturber, while states in Region 1 are not.

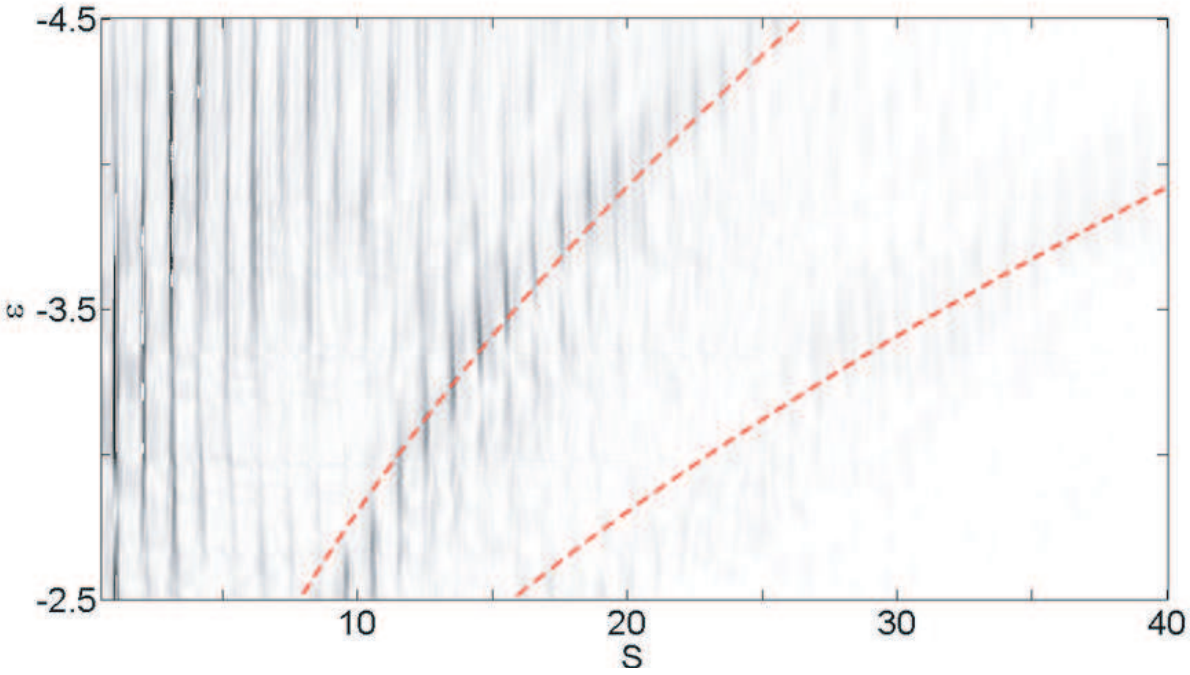

Figure 3.8: Ba recurrence map. Dashed lines are the one-electron $j = 1$ and 2 Stark revivals.

3.2.2 Scaled Energy Recurrence Spectroscopy

To reveal the periodic orbital dynamics in a static-electric field, the Stark map axes are scaled into the coordinates

$$\epsilon = E/\sqrt{F}, \tag{3.1}$$

$$n^* = 1/\sqrt{-2E} \text{ [22]}. \tag{3.2}$$

Fourier transformation with respect to n^*, produces a scaled-energy recurrence map as a function of scaled energy, ϵ, and scaled action, S. For one-electron atoms, one unit of scaled action corresponds to a single Kepler period. The recurrence strength at any point is proportional to the probability that an electron wave-packet, launched from the ion core at $t = 0$, has returned to the core in its initial configuration, at a time $t = S$ later.

While a two-electron Hamiltonian is not scale invariant, we analyze Ba and Ca spectra with SERS in the approximation that these systems can be treated as one-electron atoms in a static-electric field. Figures 3.8 and 3.9 are the Ba and Ca recurrence maps respectively.

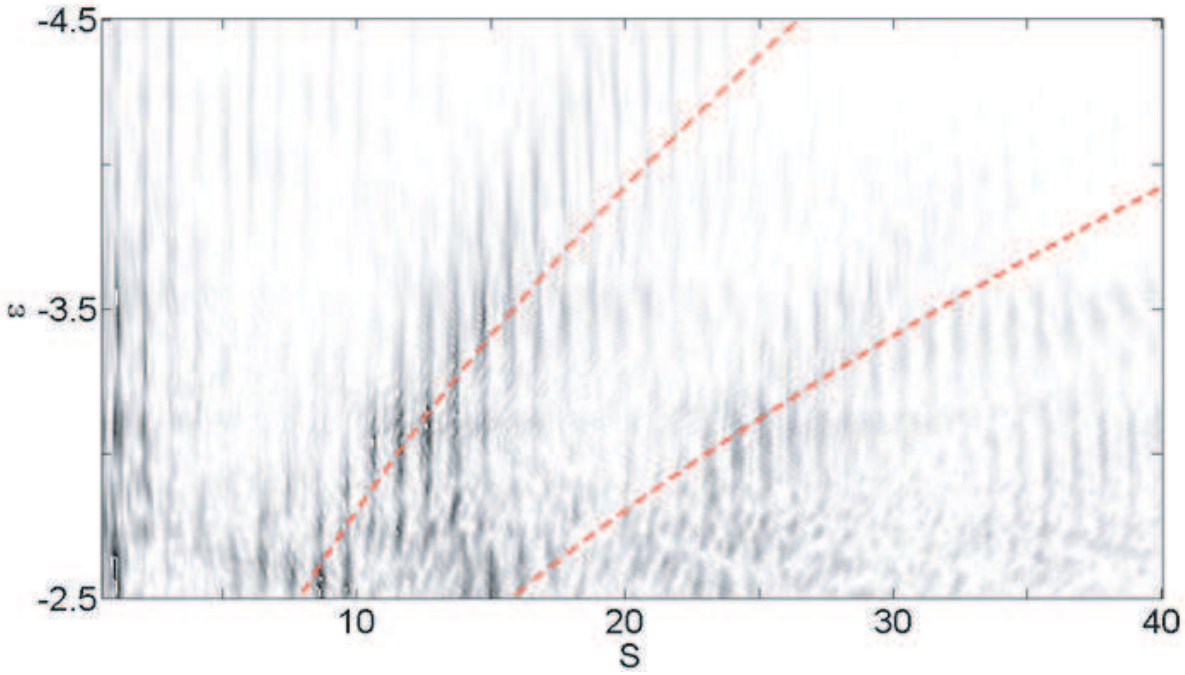

Figure 3.9: Ca recurrence map. Dashed lines are the one-electron $j = 1$ and 2 Stark revivals.

The scaled energy recurrence maps clearly illustrate the changing rate of angular momentum precession as a function of scaled energy, as the recurrence strength tends to fade out, when the electron is torqued by the field and no longer returns to the ion core in its original state. For large negative values of ϵ, the electric field is relatively weak and many Kepler recurrences are observed before the electron's increasing angular momentum temporarily precludes further returns to the vicinity of the nucleus. Conversely, for less negative ϵ, the angular momentum precession from low to high and back to low-l configurations occurs more rapidly. Accordingly, bands of recurrence maxima are observed centered at Stark recurrence times,

$$S_j = (\frac{4}{3}\epsilon^2 - \frac{1}{2})j, \tag{3.3}$$

for the j *th* repetition of the Stark precession. In single electron systems, recurrence maxima within the j *th* band or sequence [42] are seen at integer or half-integer values of S for even and odd values of j respectively [22]. For an example, hydrogenic integrated recurrence spectra are calculated and shown in Fig. 3.10. These plots also function as comparisons with

the experimentally obtained plots in the following sections.

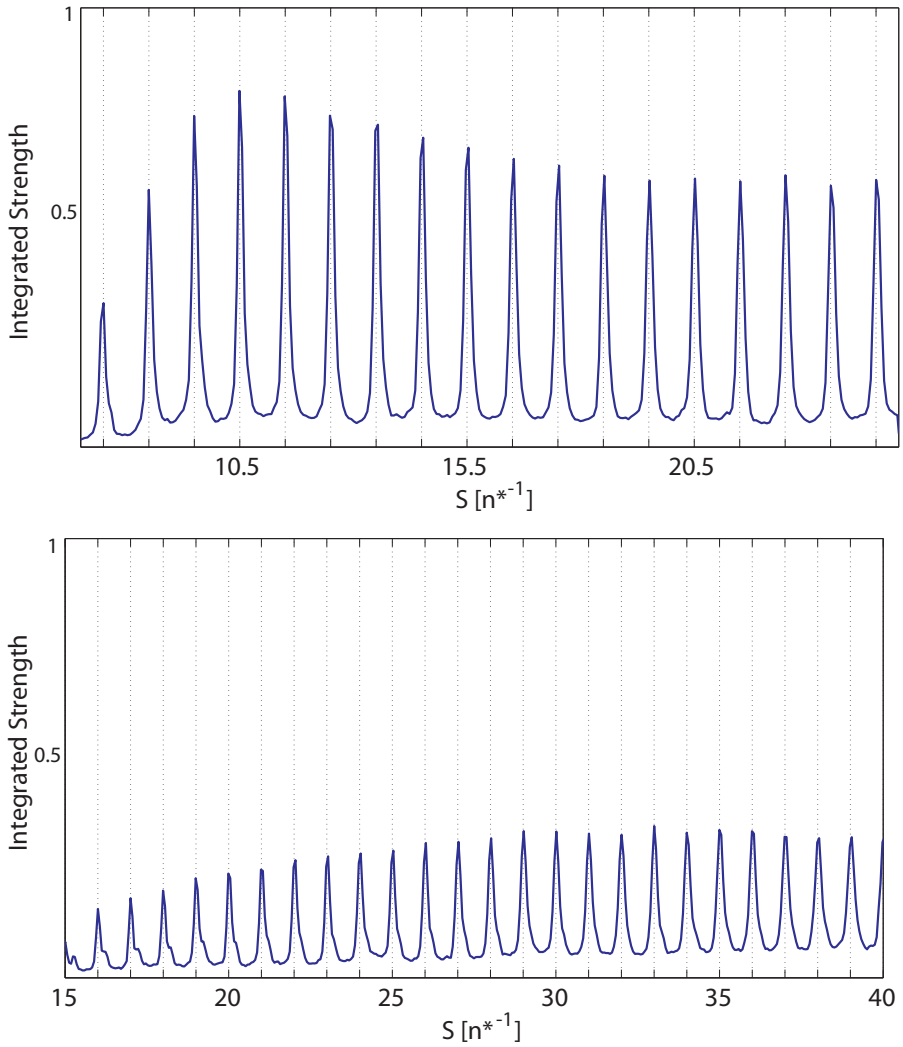

Figure 3.10: Calculated strength of the Sequence 1 (upper plot) and Sequence 2 recurrences (lower plot) in hydrogen, integrated over scaled energy. Recurrence strengths peak at half-integer values for Sequence 1 and integer values for Sequence 2.

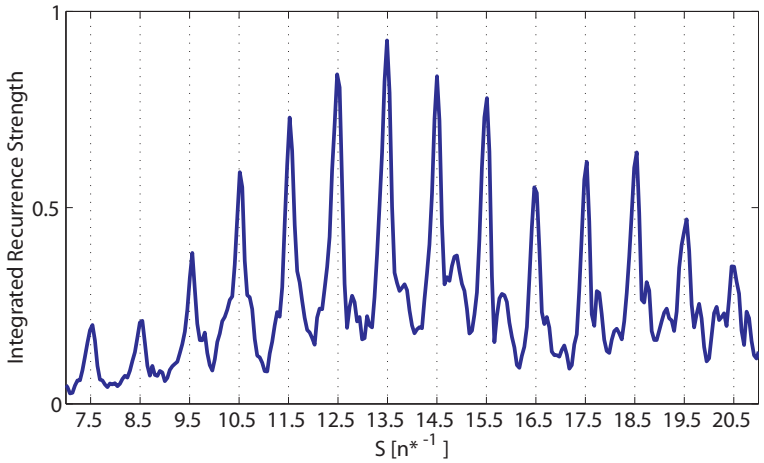

Figure 3.11: Integrated Ba recurrence strength as a function of action. Secondary recurrence peaks are observed after the large Sequence 1 peaks that are maximal at half-integer values of the action.

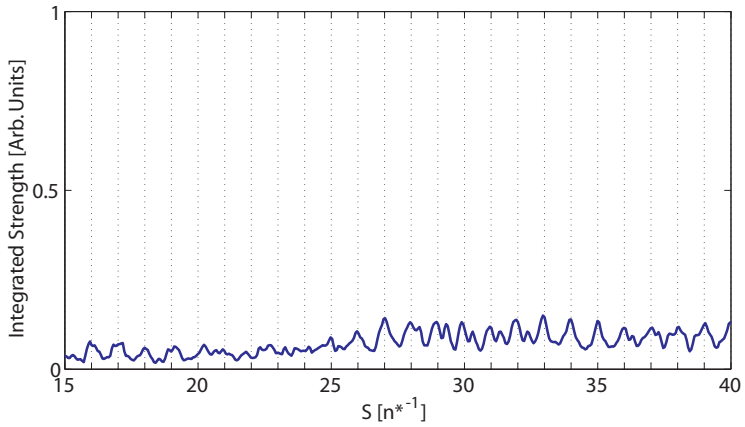

Figure 3.12: Integrated Ba recurrence strength as a function of action for Sequence 2. Signal levels are significantly smaller, possibly because of the significant dispersion in the perturbed wave-packet. Even with the lower signal levels, additional structure is observed in these spectra as well.

In the Ba recurrence map, Fig. 3.8, the first Stark revival is visible but the recurrence strengths of the second revival are weak. Additionally, a second set of recurrence peaks, are observed roughly $0.279 \pm 0.003\ n^{*-1}$ after the primary peaks. The secondary peaks are viewed clearly in Fig. 3.11 where the recurrence strengths of the $j = 1$ sequence are integrated over ϵ at constant action. In this experiment, the entire energy range of the $5d7d$ perturber was sampled when $\epsilon > -3.0$. The multiple-recurrence structure reflects the two-electron dynamics in the system. While two-electron effects are clear, the energy range over which a scaled-energy recurrence spectrum is sampled is important to the resulting dynamics. This point is explored further in section 3.3.3.

Sequences corresponding to the first and second Stark revivals are visible in Ca. Though recurrence strength maxima within the sequences are located near the values predicted by Eqn. 3.3, at large action the Kepler recurrence peaks are shifted off of the hydrogenic values. These shifts are clearly visible in Figs. 3.23 and 3.14, where the recurrence spectra in the $j = 1$ and 2 sequences are integrated while holding action constant. Similar recurrence peak shifts are observed in the zero-field autocorrelation, a point that is discussed further in sections 3.3.4 and 3.3.5.

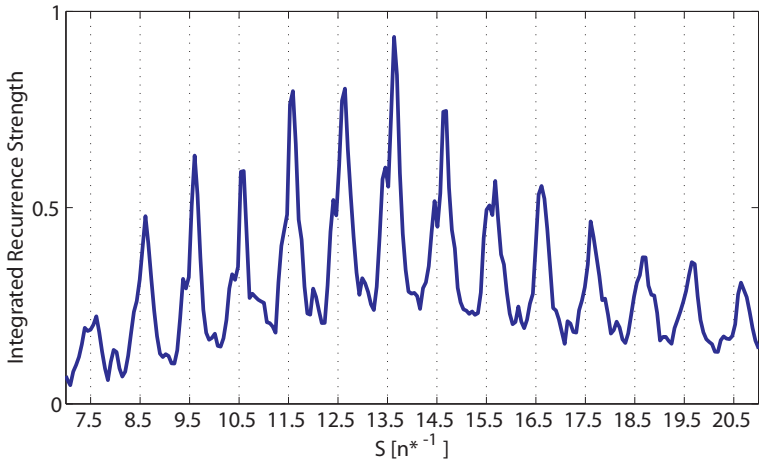

Figure 3.13: Strength of the Sequence 1 Ca recurrences integrated over scaled energy. Peak strengths are shifted to actions larger than the half-integer values.

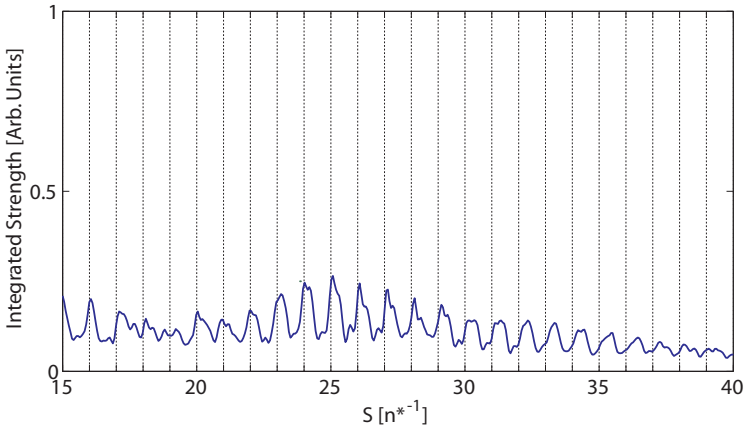

Figure 3.14: Strength of the Sequence 2 Ca recurrences integrated over scaled energy. Peak strengths are shifted to actions larger than the integer values.

3.3 Discussion

3.3.1 Overview of Results

The coarse structures in both the Ba and Ca recurrence maps are strikingly similar to those associated with single-electron atoms. This is perhaps surprising in light of the strong perturbations in the Rydberg and Stark spectra of these two-electron systems. However, this similarity reflects that the electron's interaction with the static-electric field dominates the dynamics of these systems.

The classical picture of an electron in an elliptical orbit precessing in the static-electric field illustrates the dynamics that lead to the Stark revivals in scaled-energy recurrence maps. In this wave-packet picture, the electron is launched from the atomic core with $l = 2$. The inner valence electron is localized near the core in alkaline earth atoms, and consequently when the Rydberg electron is at a small radius it may interact with the doubly-excited configuration. Thus, the initial conditions of the orbit are influenced by the doubly-excited configuration, leading to two-electron dynamics. However, launched into the static-electric field, the wave-packet's angular momentum is rapidly torqued and the electron spends little time during the Stark period as a d-wave. The perturber studied in these Rydberg series of Ca and Ba couples through the d-character. Consequently, the two-electron effects are muted in the presence of the field, and the one-electron picture remains valid using SERS even in these highly perturbed alkaline earth atoms. Still, by examining the recurrence positions when the electron returns the core, ie. at the $j = 1$ Stark revival, the two-electron effects are apparent.

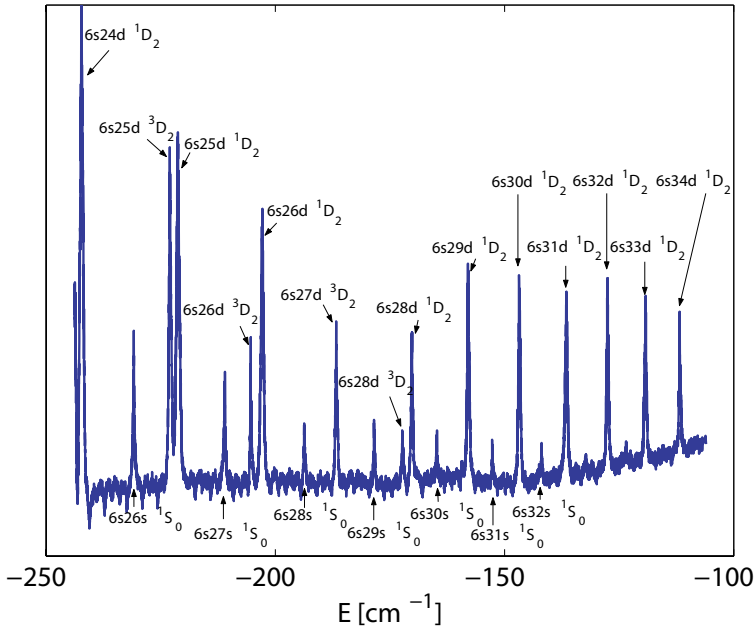

Figure 3.15: Measured Ba spectrum in the perturber's vicinity. States are labeled in accordance with Ref. [51].

3.3.2 Ba Spectroscopy

The Ba Stark map (Fig. 3.6) shows a pronounced window resonance near $E = -194\ cm^{-1}$. This window resonance is also conspicuous in Fig. 3.15, the zero-field Ba spectrum, where it is associated with the $5d7d\ ^1D_2$ perturber. A scaled autocorrelation of this zero-field spectrum is shown in Fig. 3.16. The perturber and its effect on the $6snd$ series has been studied previously in zero-field [50, 51] and in static-electric fields [41, 52]. The resonance spans approximately 4 n-states, coupling singlet and triplet d-states with the perturber. While at lower ($n < 22$) and higher ($n > 31$) energies the quantum defects of singlet and triplet d-states do not vary significantly, *near the perturber the quantum defects change rapidly* [51].

3.3.3 Ba: Narrow Perturbing Resonance

As illustrated in the energy level diagram, Fig. 3.3, the $5d7d$ perturber is narrow compared with surrounding Rydberg regions, so by sampling the energy spectrum in Fig. 3.6 through

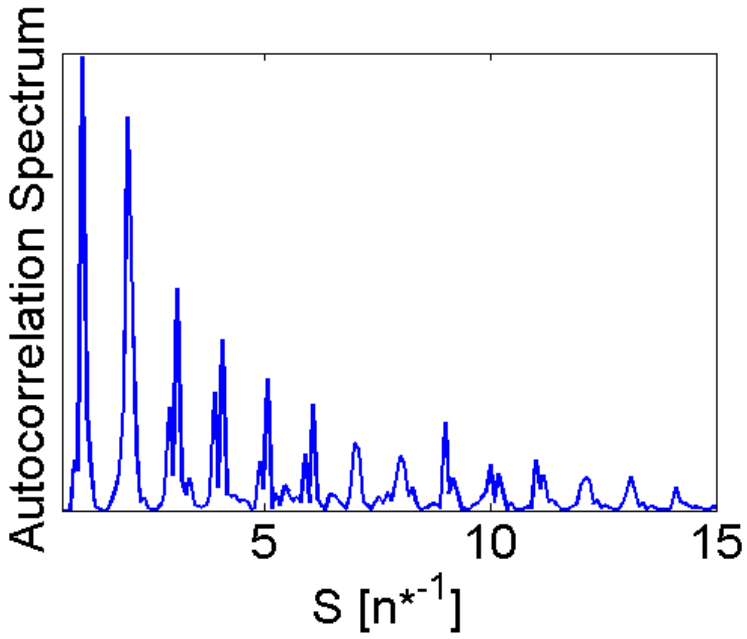

Figure 3.16: Autocorrelation of the measured Ba spectrum, Fig. 3.15. S the action is the Fourier conjugate to energy in units of n^*. Oscillations between singly- and doubly-excited configurations [50] are reflected in the multi-peaked structures and the decaying tails that recurrence peaks have on their higher-action sides.

narrow windows either excluding or including the perturber region, the one- and two-electron dynamics near the core are differentiated in Fig. 3.17. In the wave-packet picture, the locations of recurrence peaks at half-integer values suggest that the electron is launched as a Rydberg wave-packet regardless of the chosen energy range. However, sampled directly within the perturber's energy range, doubled peak structures are prominent indicating a wave-packet interference not demonstrated in Ca nor the computed H spectrum. By contrast, sampled from energies well outside of the perturber's energy range, the one-electron picture is recovered.

Lyons *et al.* studied the evolution of a singly-excited Rydberg wave-packet launched in the vicinity of the $5d7d$ perturber, and showed that the wave-packet oscillates between singly- and doubly-excited configurations [50]. These oscillations are reflected in the multiply-peaked structures of Fig. 3.16, which is a Fourier transformation of the energy spectrum. Scaling the Rydberg energy axis into the coordinate $n^* = 1/\sqrt{-2E}$ before Fourier transformation

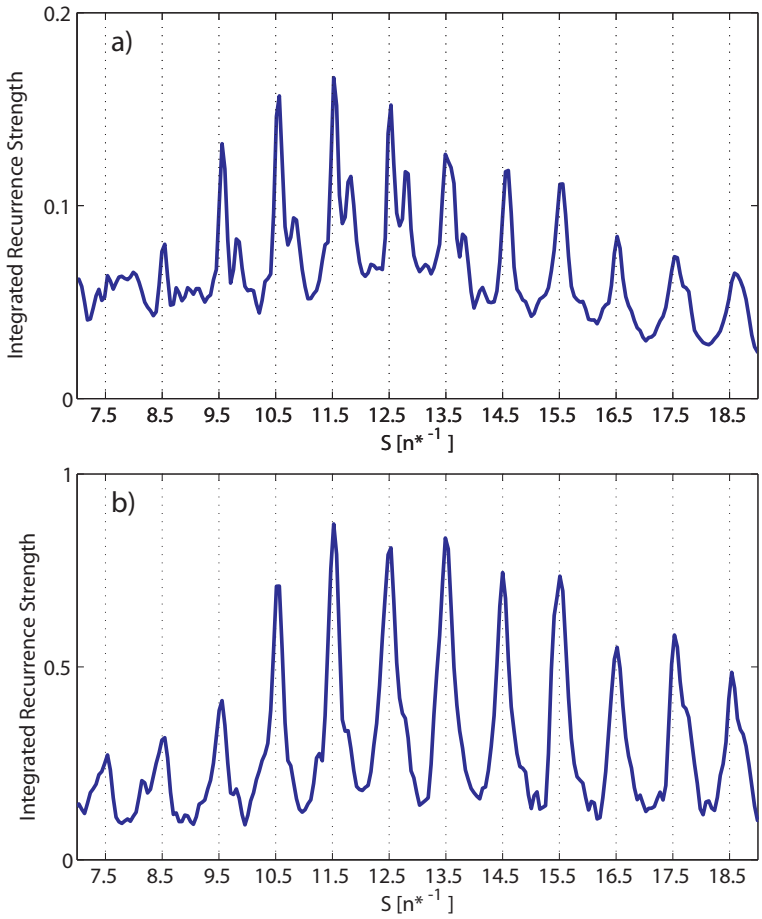

Figure 3.17: Ba Sequence 1 integrated recurrence strength sampled through narrow energy windows. a) is sampled in Region 1 of Fig. 3.6, near the $^1D_2$ $5d7d$ perturber. b) is sampled in Region 2 of Fig. 3.6, adjacent to the perturber.

produces the scaled autocorrelation in Fig. 3.16, where peaks mark the electron's return to the core as a d-wave.

The integrated recurrence spectra in Fig. 3.11 indicate the dynamics when the electron returns to the core as a d-wave in the static-electric field. The primary recurrences peak at half-integer values, the expected $j = 1$ recurrences for a one-electron atom, suggesting that the electron is launched as a Rydberg wave-packet that precesses in the field, then later revives at the Stark period. Upon returning to the core as a d-wave there is a large probability to scatter into the $5d7d$ configuration. Collisions between the two valence electrons ensure that the doubly-excited configuration has a finite configuration interaction time, τ_{CI}, measured previously as $0.58ps$ [41]. Although we obtain a fairly consistent splitting between peaks, indicating a picture where the secondary recurrence peaks are observed as the electron scatters out of the $5d7d$ configuration, and back into the Rydberg d-state, it is not clear that this should be the correct picture. The work of Henle *et al.* [54] calculates the wave-packet of a perturbed Rydberg series and shows "breaking up of the wave packet into two parts." They simulate this wave-packet by considering an energy-dependent quantum defect of the form $\mu = \delta - 1/(\pi arctan[\frac{1}{2}\Gamma/(E - E_n)])$, where δ is the unperturbed quantum defect, Γ is the resonance width, and E_n is the energy of the perturber [54]. The perturbed wave-packet decays, providing a long tail on the higher-action side of the recurrence peaks, with a relaxation time of $\tau_{CI} = 1/\Gamma$ (see Fig. 3.16 and Fig. 3.11 for indications of a long tail in Ba data). The portions of the wave-packet that decay out of the doubly-excited configuration are out of phase with the original state on later visits to the core. At certain times, the out of phase portions interfere constructively or destructively, producing the multiple-peak structures, Henle's so-called breaking up into parts. However, the characteristic time-scales for interference related splittings in zero-field are not given by τ_{CI} [54]. In Figs. 3.18 and 3.19 plots b) and c), results are shown from two different model spectra and their scaled

autocorrelations, analogous to the wave-packet calculations of Henle *et al.*. Both perturbed autocorrelations exhibit interference peaks. In both autocorrelations, to the extent that there is any order to their sizes, the splittings are roughly the same size, despite that in Fig. 3.19 b) $\Gamma = 4n^*$ and in Fig. 3.19 c) $\Gamma = 10n^*$. The size of the splittings are in fact dependent on both τ_{CI} and on the temporal resolution, which is inversely-proportional ΔE_{Total}, the entire range of energies. In fact, the size of the interference splittings in Fig. 3.19 b) and c) are more strongly dependent on ΔE_{Total} than on τ_{CI}.

One might also wonder if the hole in the spectrum, exhibited clearly in the Ba Stark map is the cause of the multiple peak structures in the Ba recurrence map. Figures 3.18 and 3.19 d) and e) show calculated autocorrelations resulting from evenly spaced energy levels with a hole in the oscillator strengths. The evenly spaced spectrum without a hole in it Fig. 3.18 a) and its autocorrelation Fig. 3.19 a) are also given for comparison. From these graphs we see that a hole in the spectrum creates symmetrical side-bands around the standard recurrence peaks, at integer values. While we possibly are seeing effects of the hole in the Ba recurrence spectrum, the dominant interference features are the asymmetric structures, occurring on the larger action side of the peaks. The model calculations shown in Figs. 3.18 and 3.19 should be considered in the context that they are analogous to zero-field spectra, in contrast to the Ba recurrence maps which are scaled autocorrelations of a perturbed Rydberg atom in a static electric field. However the calculations, suggest that the effects of the hole in the Ba Stark map do not cause the asymmetric multiply peaked structures we observe. The asymmetric multiply peaked structures we observe are a result of the changing quantum defect near the $5d7d$ perturber.

Since in a static-electric field we observe a reasonably consistent interference structure, for completeness, the sampling window size in energy space (ΔE_{Total}) was varied to investigate its effects on the recurrence spectra. While changing the window size, more states are

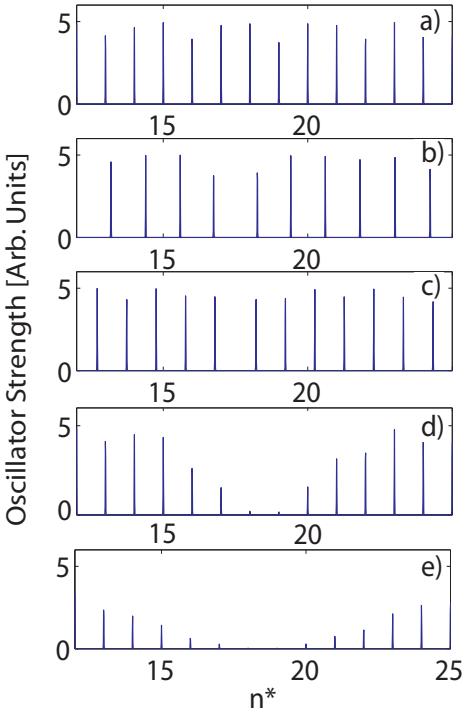

Figure 3.18: Model Spectra. a) Evenly spaced energy levels at integer values. b) and c) Changing quantum defect spectrum, with the form discussed in the text [54], where $\Gamma = 4n^*$ and $\Gamma = 10n^*$ respectively. d) and e) Evenly spaced spectra with attenuated oscillator strength. The FWHM of the holes are $\Gamma = 4n^*$ and $\Gamma = 10n^*$ respectively.

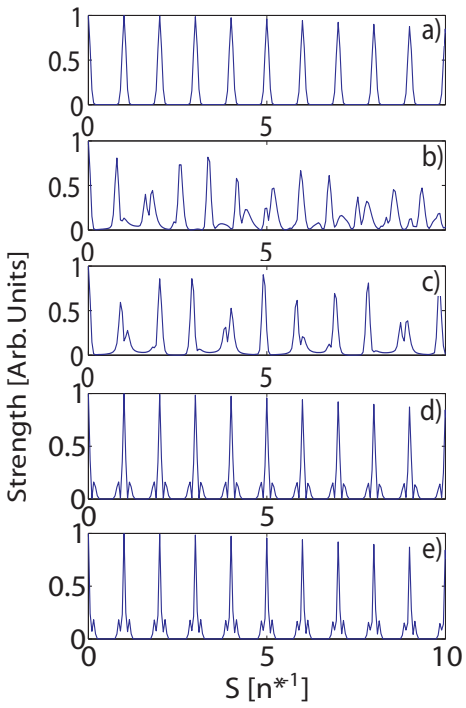

Figure 3.19: Scaled autocorrelations of respective spectra in Fig. 3.18. a) Evenly spaced peaks at integer values. b) and c) Perturbed spectra with asymmetric interference structure in both cases. d) and e) Symmetric structures, with width related to the bandwidth and Γ, result as sidebands on the evenly spaced autocorrelation peaks.

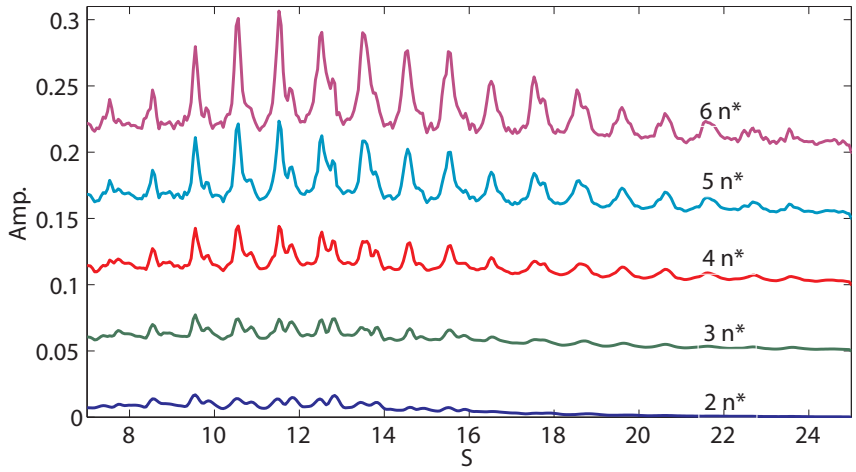

Figure 3.20: Ba Seq. 1 scans (offset for clarity) where the sampling window is a gaussian $exp[-(N-n^*)^2/\sigma^2]$ with $n^* = 24.5$, and various values of σ annotated. The positions of doubled peaks are not significantly shifted by changes of σ.

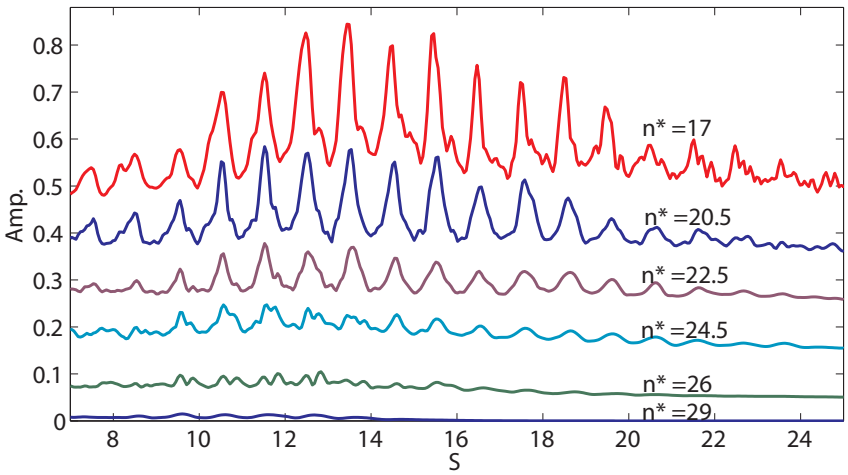

Figure 3.21: Ba Seq. 1 scans (offset for clarity) where the sampling window is a gaussian $exp[-(N-n^*)^2/\sigma^2]$ with $\sigma = 2.5n^*$, and various values of n^* are shown. Double-peaked structures are observed when $n^* = 24.5$, near the energy of the $5d7d$ perturber.

included and a modest variation in recurrence peak positions and amplitudes is expected. This investigation, plotted in Fig. 3.20, indicates that the peak positions, and therefore the splitting between primary and secondary recurrence peaks, are not significantly shifted, even for large variations of the sampling window size. The lack of large shifts in the peaks' positions with variations in window size suggests that the recurrence data is not transform limited. However, this study clearly shows that the interference structures that are observed are not a result of the window size. Similar to the previously discussed plots, Figs. 3.11 and 3.17, Fig. 3.21 clearly shows that the recurrence spectrum interferences are localized to the perturbed region of the energy spectrum.

In summary, the experimental investigations of the Ba scaled energy recurrence spectrum apparently indicate a wave-packet picture where the secondary recurrence peaks are a result of the electron scattering into the $5d7d$ perturber state for a measured time of about $0.6ps$ before it rescatters into the Rydberg d-character. Since the recurrence spectrum is an autocorrelation, and the time just mentioned is a measurement, this interpretation follows. However, even though it is tempting to think so, the measured time scale's agreement with the configuration interaction time is fortuitous, since the analysis of the analogous zero-field spectrum shows that the interferences in scaled autocorrelation peaks are not strongly dependent on τ_{CI}.

3.3.4 Ca Spectroscopy

In the Ca Stark map the effect of the $3d3d$ perturber is somewhat subtle. It's presence is more obvious in the zero-field spectrum shown in Fig 3.22. Notably, the $4s15s$ state, located at $E = -685\ cm^{-1}$, has larger photoabsorption probability than the neighboring $4s14d$ state. However, at higher n-values ($n > 20$) the spectrum follows the characteristic propensity for significantly stronger d-, compared to s-excitation strengths. Armstrong *et al.* [46] observed

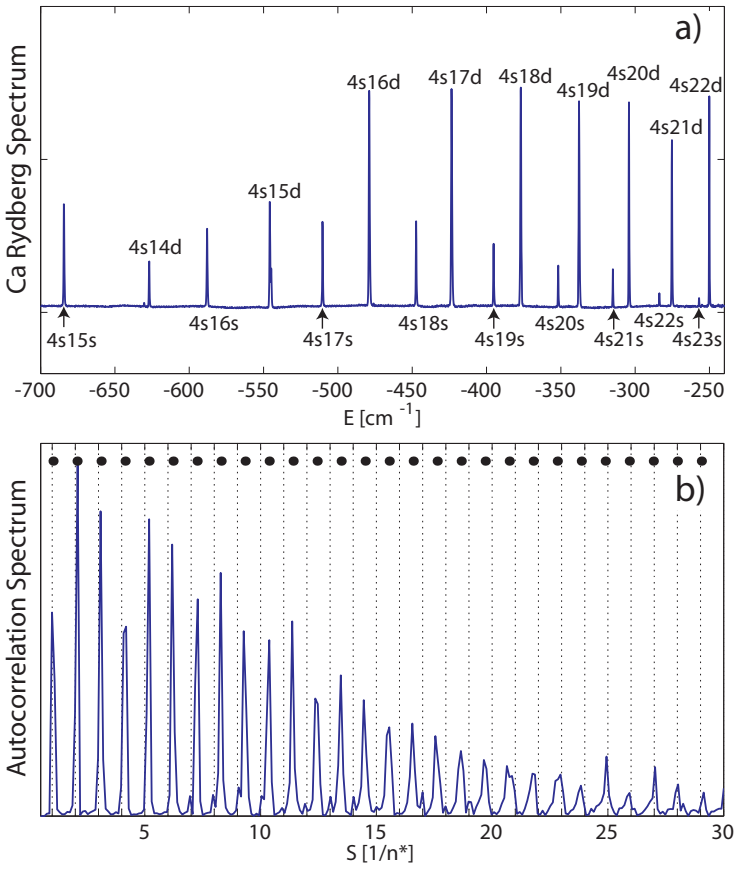

Figure 3.22: a) Rydberg and b) autocorrelation spectra of Ca. The $4snd$ Rydberg series is perturbed by the doubly excited $3d3d$ state. The autocorrelation spectrum shows the Rydberg character near the ion core as function of action. Dashed lines at integer action mark the standard single-electron Kepler recurrences. Bullets (•) show the predicted peak positions when the energy dependence of the quantum defect $\Delta\delta = 0.037$ is taken into account.

a minimum in the d-state oscillator strength near $4s13d$ consistent with Fig. 3.22, which shows a clear attenuation of the d-state photoabsorption probability at energies $E < -500$ cm^{-1}. In addition to oscillator strength variation, the quantum defect changes as a function of energy from $\delta_d = 0.60$ at $n = 13$ to $\delta_d = 1.01$ at $n = 22$.

As shown previously, in Sec 3.3.3, Fourier transformation of the energy spectrum yields a wave-packet picture in the time domain. Scaling the Rydberg energy axis into the coordinate $n^* = 1/\sqrt{-2E}$, before Fourier transformation, produces the autocorrelation in Fig. 3.22, where peaks mark the electron's return to the core as a d-wave. Ca's changing quantum defect leads to a longer orbital period, $\tau'_K \approx \tau_K(1 + \Delta\delta_d)$, where $\Delta\delta_d \ll 1$ is the change in quantum defect per n, and the additional time per orbital period is spent near the atomic core [47]. The hydrogenic Kepler recurrences, S_K, peak at integer values. However, with a varying quantum defect, the characteristic orbital recurrence becomes $S'_K \approx S_K(1 + \Delta\delta_d)$. While the change in quantum defect per n is only a few percent, after several orbital periods, the extra time accumulates and the electron returns to the core significantly after the standard Kepler recurrence.

3.3.5 Ca: Broad Perturbing Resonance

Considering the schematic energy level diagram, Fig 3.3, our experiment excites comparable proportions of both the perturbed and unperturbed Rydberg character. As previously discussed with Ba, and shown in Fig. 3.23, sampling through narrow energy windows, one where the quantum defect changes less rapidly, and one where the quantum defect changes significantly per n, isolates the effects of the perturber. One difference from the discussion of Ba is that in Ca the perturbing resonance is very broad, yielding a short configuration interaction time, which was estimated previously to be on the order of $100 fs$ [46]. In the wave-packet picture, selectively sampling the energy range, in proximity to the perturbing

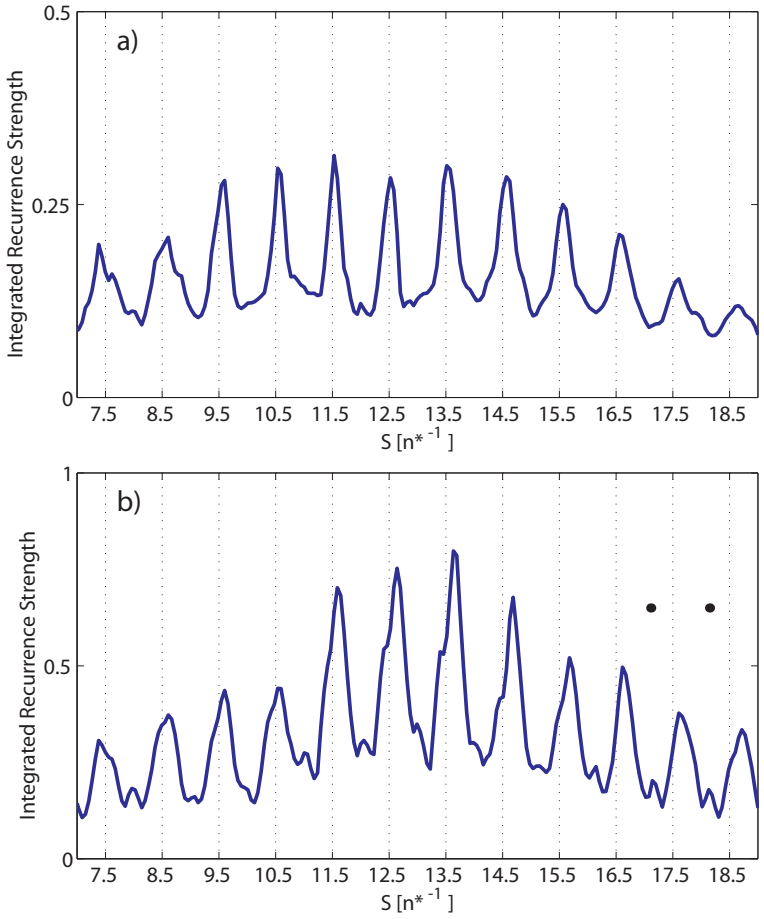

Figure 3.23: Ca Sequence 1 integrated recurrence sampled through narrow energy windows. a) is sampled in Region 1 of Fig. 3.7. b) is sampled in Region 2 of Fig 3.7. The $3d3d$ perturber couples strongly into the d-states included in Region 2. Bullets (•) mark the predicted positions of recurrence peaks for $S = 13.5$ and 14.5, assuming a proportional increase in the Kepler recurrences, like is seen in the zero-field case (see Fig. 3.22). Measured peak positions do not show a proportional increase in the action of the same size as they do in the zero-field spectrum.

resonance, is essentially like choosing the wave-packet's initial configuration. In Region 1 of the Ca Stark Map, Fig 3.7, a one-electron wave-packet is launched. In Region 2 of Fig 3.7, where the perturber is strongly coupled into the Rydberg series, small shoulders then dips in the recurrence strengths at the half-integer values of the action, are observed before the primary recurrence peaks, reflecting elements of the previously discussed perturbed wave-packet picture. Since τ_{CI} is so short there is a large probability for the wave-packet to scatter into the perturber and back out again before the end of the wave-packet's excitation. The primary recurrence peaks are located at slightly larger actions than predicted by the one-electron picture, because the wave-packet is launched in a mixed, single/double-valence, configuration.

Despite that two-electron effects are measured, our observations of Ca quantitatively reinforce the picture that two-electron dynamics are rare while the Rydberg electron is precessing in the electric field. In the zero-field situation for Ca, where the electron is launched from a mixed singly- and doubly-excited configuration, the picture is clear, since the doubly-excited configuration is localized near the core, the electron must scatter from the two-electron configuration to orbit outward as a Rydberg electron. Before the electron returns to its initial state it must scatter back into the perturber character. The configuration interaction time, associated with scattering between the double- and single-valence states, causes the longer Kepler period. Likewise, the shift of recurrences in Figs. 3.9, 3.13, and 3.23 are a reflection of the longer Kepler period, and the lag behind one-electron recurrence peak positions accumulates each time the core is sampled, indicated by the trend of larger shifts in recurrence peaks at larger action. However, as Bates *et al.* noted previously, one should not expect a proportional increase in the Stark recurrence positions since the electron rarely visits the core, and spends very little time in the perturbing configuration during the Stark period [41]. The Ca system studied here is expected to have much smaller shifts than

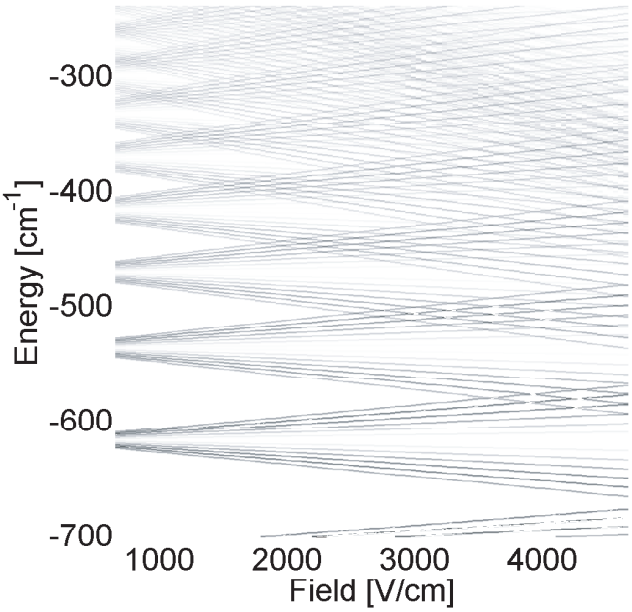

Figure 3.24: Calculated shifted-hydrogen model where values of $\Delta\delta = 0.04$ are the shift between all zero-field levels.

were observed in Ba, by Bates *et al.*, but provides extensive data at the $j = 1$ Stark revival. Bullets mark the expected positions of selected recurrence peaks in Fig. 3.23 b), assuming a proportional increase in the Stark recurrence peak locations. The lack of agreement between the measured peak positions and the peak positions assuming the proportionally increasing model demonstrates the failure of this model for describing the perturbed Ca wave-packet in a static electric field.

Since we are stating that the two-electron effects are muted in the static electric field, for completeness, we present an exploration of how small shifts in the Rydberg energy levels do lead to large shifts in the recurrence spectrum, and how the shifts might affect dynamics in a static-electric field. To study the effects of small shifts, a hydrogenic Stark spectrum is computed where the n-labeled Stark manifolds are separated by $\Delta n^* = \Delta n - \Delta\delta$. One specific hydrogenic spectrum is shown in Fig. 3.24, where Δn is unity and $\Delta\delta = 0.04$. Although the small energy level shifts are not readily apparent in the hydrogenic Stark spectrum, in the integrated recurrence spectrum, Fig. 3.25, calculations for a shift of $\Delta\delta = 0.04$ produce

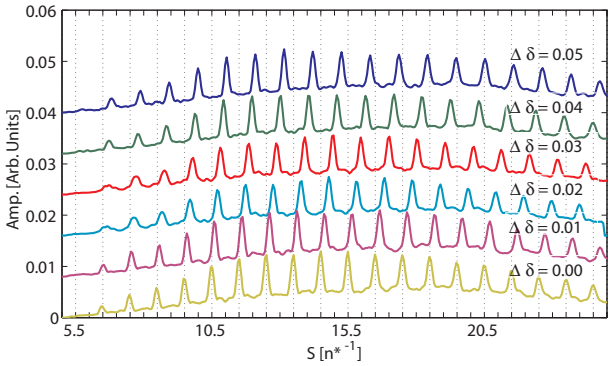

Figure 3.25: Calculations (offset for visual clarity) using the shifted-hydrogen model where the value of $\Delta\delta$ is the shift between zero-field levels. The largest shifted Ca data in Fig. 3.26, $n^* = 15$, is reasonably-well represented by these calculations where $\Delta\delta = 0.01$, even though from the zero-field spectrum (see Fig. 3.22) one might expect a larger shift. In the measured spectra, large shifts are not observed because only the d-states are shifted and the electric field mixes in other l-states.

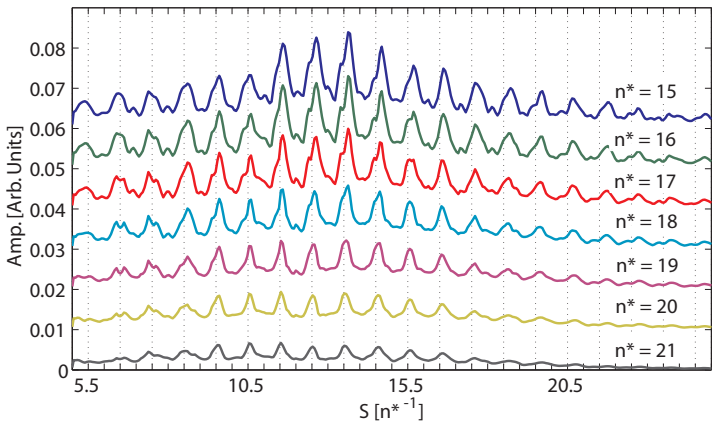

Figure 3.26: Ca Seq. 1 integrated recurrence strength where the sampling window is a gaussian $exp[-(N - n^*)^2/\sigma^2]$ with $\sigma = 3n^*$, and various values of n^* are shown. The curves are offset for display purposes. At the smallest n^*, recurrences peak after half-integer values, since these energy ranges encompass the $3d3d$ perturber. At the largest n^*, recurrences are at integer values, similar to what is expected for hydrogen.

integrated recurrences that peak conspicuously late when the electron returns to the ion core at the Stark period. Comparison of the most shifted Ca recurrence spectra in Fig. 3.26 with the modeled recurrence spectra in Fig. 3.25, indicates a reasonable agreement when $\Delta\delta = 0.01$. The fact that all of the recurrence peaks are shifted by much less than in the hydrogenic model where $\Delta\delta = 0.04$, the shift one might expect from zero-field considerations, demonstrates that the electron in a static-electric field spends very little time in the perturbing configuration before the first Stark period.

3.4 Conclusions

We have measured Ca and Ba photoabsorption as continuous functions of energy and static-electric field. Through the methods of scaled energy recurrence spectroscopy, and a technique for viewing the wave-packet dynamics when the electron returns to the core in its initial state, the orbital dynamics of two-electron atoms in a static-electric field are probed. In Ca, the elliptical orbital period is slightly longer, an effect of the broad energy perturbance of the d-states. In Ba, near the energy localized $5d7d\ ^1D_2$ perturber state, interferences are apparent in the recurrence spectra. By studying these two systems, in conjunction with the work of Bates *et al.* [41], we study the effect of perturbers in Rydberg series on the energy-dependent quantum defects, and the implications for choosing the initial conditions of the excited electron. Despite, the two-electron behavior observed in the alkaline earth spectra, overall we see scaled energy recurrence spectra where the Kepler and Stark periods are predicted well by the one-electron picture, indicating that orbital dynamics are dominated by interactions with the static-electric field, and not by the low l-states. The techniques we demonstrate for viewing the electron when it returns to the core in a scaled energy recurrence spectrum provide interpretable pictures of the two-electron dynamics in a static electric field. Potentially, this work opens the door to studying more even complicated

systems, for example Rydberg systems with several configurations or even molecular systems.

Chapter 4

Ultra-short Pulse Terahertz Generation

4.1 Introduction

Ultra-short pulse terahertz (THz) radiation is produced in the laboratory using a biased Gallium Arsenide (GaAs) semiconducting wafer, illuminated by ultra-short pulse laser light. The main lobe of the ultra-short THz radiation is approximately $0.5ps$ wide (FWHM) [66]. Additionally, the main lobe of this short pulse is roughly half an optical cycle of mm-wavelength radiation, hence the term half-cycle pulse (HCP).

Terahertz radiation is positioned between infrared and microwave, but is a largely unexplored region of the spectrum. Active research into THz generation and THz pulse properties is conducted both in our lab [55, 56] and in others', for a small sample of this research see Refs. [57]- [66]. One reason that the THz region remains less explored than the adjacent regions, is a lack of reliable THz sources and detectors. Currently, there is a wide variety of active research areas, including THz domain spectroscopy of biochemical compounds [58], THz detection in observational astronomy [71, 72], and semiconductor physics [64, 65], all in

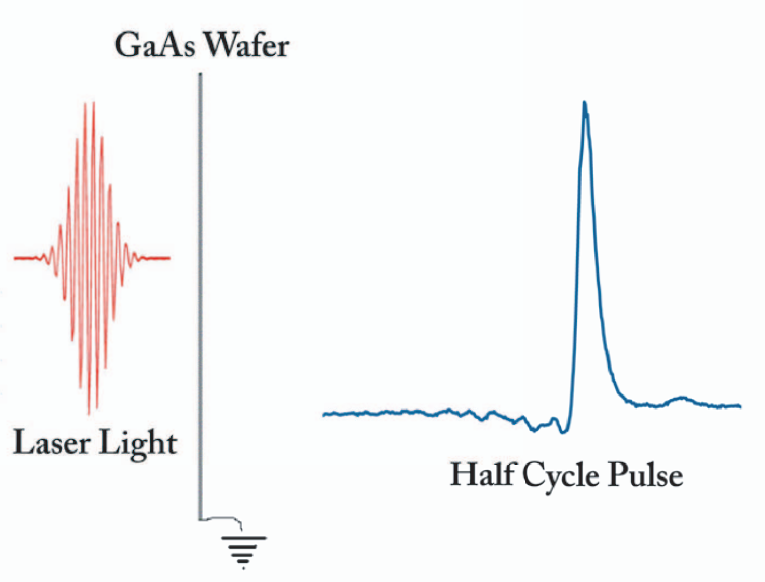

Figure 4.1: Ultra-short pulse laser light illuminates a biased GaAs wafer. A half-cycle pulse of ultra-short THz radiation is produced. The half-cycle pulse trace shown in this schematic diagram is a measurement of the electric field strength as a function of time provided by Dr. Lung Ko [56].

addition to the atomic physics research discussed in this thesis and in many of the references in the bibliography.

This chapter provides experimental details of the ultra-short pulse THz radiation used in this thesis. In this chapter HCP characterization is demonstrated through a combination of detection methods: use of a pyroelectric detector and HCP ionization of Rydberg atoms. Rydberg atoms are sensitive detectors of THz radiation, and HCP ionization of Rydberg atoms facilitates a calibration method for the HCP electric field strength [6]. The chapter ends with a brief discussion of impulsive momentum retrieval, which is the primary application for ultra-short pulse THz radiation in this thesis.

4.2 HCP Generation

As previously mentioned, ultra-short THz pulses are generated by illuminating a high-voltage biased GaAs wafer with ultra-short pulse laser light, shown schematically in Fig. 4.1.

Typically the laser light is $\sim 100fs$, $780nm$ (central wavelength), from the laboratory's ultra-fast laser system. The GaAs wafers are purchased from AXT Inc. Wafers are prepared for the experiments using a specific procedure that facilitates reproducible HCP generation. First, a diamond-tipped scribe is used to etch the surface of the wafer. When tapped lightly, the wafer is cleaved along the etched surface. Typically wafers are cut to a size of $2cm \times 2cm$. Electrodes are painted onto the surface of the semiconductor using GC Electronics Silver Print II. A microscope slide is used to apply the paint so that the electrodes have clean, straight edges. Silver paint is also utilized to bond both a multi-strand wire to the top electrode, and the back of the wafer to an aluminum sheet. The aluminum sheet is attached to a standard optical mount and electrically connected to ground with a multi-strand wire. The top electrode is biased using a voltage pulser, described in Ch. 2.

Since high-voltages are applied to the GaAs wafer, care is taken to avoid sparking on the wafer surface. Sparks on the wafer surface can damage the wafer, and also generate noise in an experiment. A thin layer of Norland Optical Adhesive 88 is applied on the front surface of the GaAs wafer, typically, just over the electrodes, providing a layer of insulation between the electrodes and the wafer surface. The optical epoxy is cured under a UV lamp, or by illumination with a small amount of $355nm$ laser light: approximately 1% of the total beam from the third harmonic of the Quanta-Ray $Nd:YAG$ laser. A thin layer of the optical epoxy is also applied to the back of the wafer, where the wafer is bonded to the aluminum sheet, but care is taken not cover a significant part of the wafer surface, since the epoxy may absorb the THz radiation. Using the procedure described in the last two paragraphs, as high as $8.5kV$ is routinely applied to the GaAs wafer without any evidence of sparking.

GaAs is photoconductive, with a room temperature band-gap of $1.43eV$ [83], so when $780nm$ ($\sim 1.6eV$) short-pulse laser light is incident on the surface of a GaAs wafer, electrons are promoted into the conduction band. For a GaAs wafer prepared in the manner described

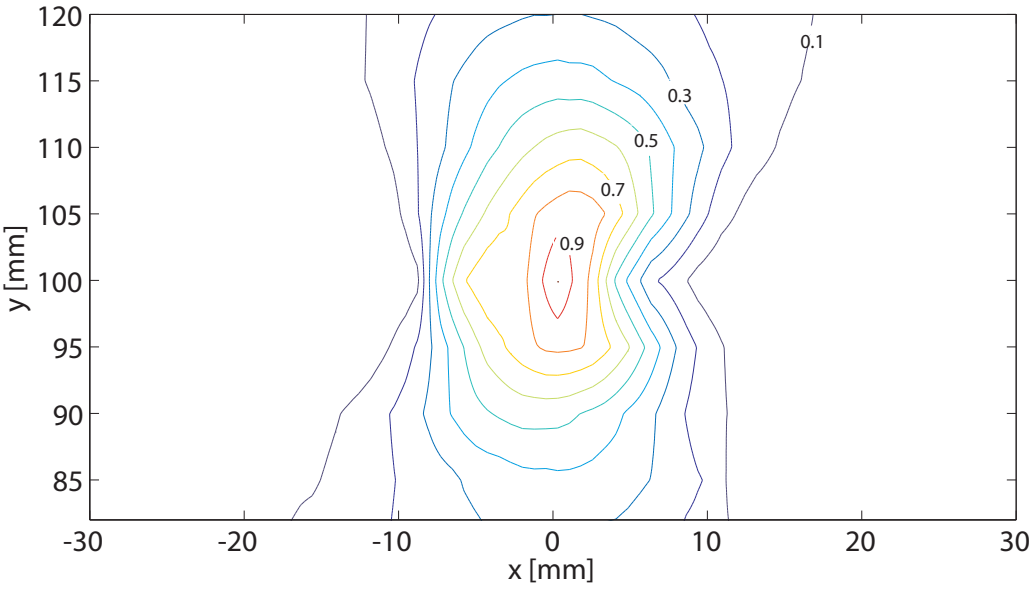

Figure 4.2: Density plot of the focused HCP beam. The beam intensity maximum is at $(x = 0mm, y = 100mm)$, which is also the focal point of $780nm$ laser light in this optical set-up. y is the beam's propagation axis, and the $f = 10cm$ parabolic mirror is positioned at $y = 0$. The measured HCP beam waist at the focal point is $7.9mm$.

here and illuminated with short-pulse laser light, biased electrons on the top electrode are accelerated to the grounded bottom electrode across the conductive surface, producing THz radiation. The THz radiation propagates through air. In experiments, two gold mirrors, one planar and one parabolic are used to guide the HCP into a detector or interaction region.

4.3 HCP Characterization

4.3.1 THz beam studies

A Molectron P1-40 pyroelectric detector is used to characterize the beam of THz radiation produced in the set-up described in the previous section. The waist of the THz beam is measured using this detector in a configuration identical to the set-up used to measure characteristics of Rydberg atoms in Ch. 5 and 6 (see Fig. 5.1). By identical we mean that the same sizes and kinds of optics are used, and the optics are positioned approximately

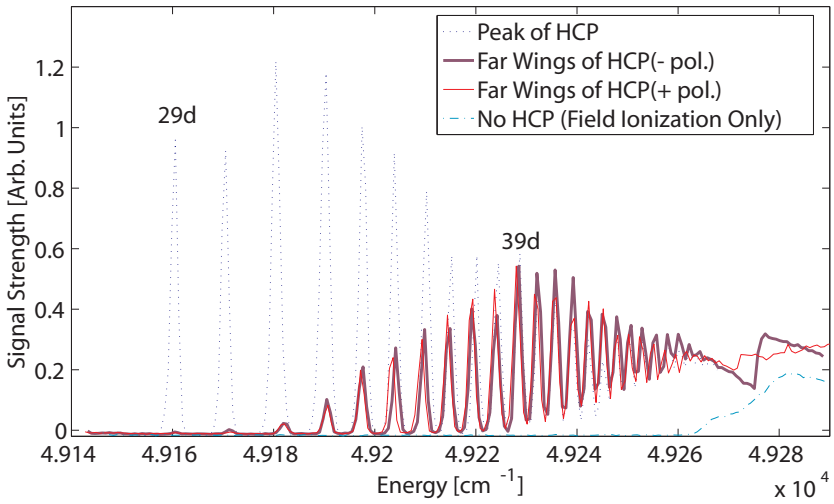

Figure 4.3: HCP ionization as a function of laser energy. The HCP bias is $6.5kV$. On-axis the HCP ionization is expected even at lower energies (ie. the $29d$ level), however, off-axis, no HCP ionization is expected, and the ionization observed is the result of an ambient noise level present when short pulse THz radiation is generated. The off-axis scans are taken $> 15mm$ from the beam axis. The absolute signal strength of the curve labeled "Peak of HCP" is attenuated by roughly a factor of two, to demonstrate the relative agreement with the "Far Wings" curves.

the same distances away from each other as they are in the atomic ionization experiments presented in this thesis. Figure 4.2 demonstrates that the THz beam is focused by the parabolic mirror. The measured THz beam waist at the focus of the parabolic mirror is $7.9mm$. Given that the active area of the P1-40 detector is $2mm \times 2mm$, it is estimated that actual beam waist is $7.5mm$, modeled as a gaussian beam detected through a $2mm$ wide square window.

4.3.2 HCP impulse calibration

Rydberg atoms are sensitive detectors of THz radiation. As with most sensitive detection schemes it is also sensitive to noise. In general HCP ionization of Rydberg atoms proceeds by a total energy transfer [5, 6, 78], so the lower the n-value, the harder a state is to ionize, and consequently the less sensitive the measurement is to noise. Typically, for HCP ionization experiments in this thesis $25 \leq n \leq 35$. High-energy states tend to ionize at the noise levels

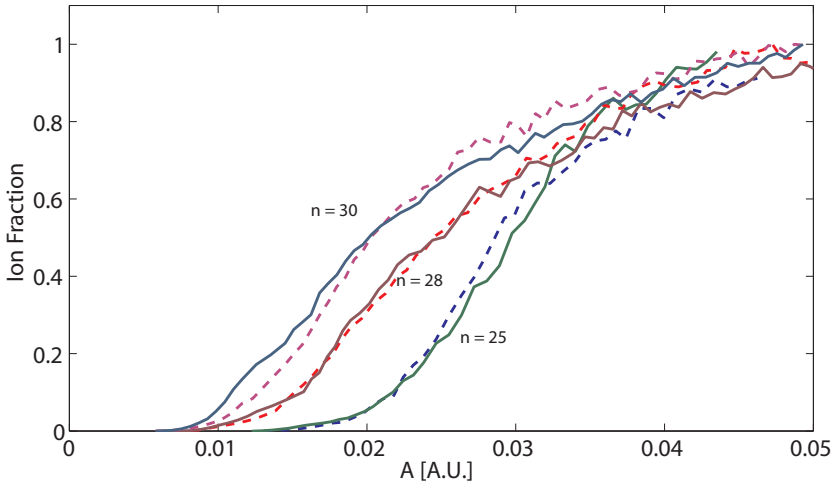

Figure 4.4: Typical HCP ionization as a function impulse, A, for various n-values. The solid curves are produced with a negatively biased wafer. The dashed curves are produced with a positively biased wafer. Rydberg d-states, having no dipole moments, are insensitive to the HCP polarity. Verification that opposite polarities produce similar ionization curves aids in checking the HCP alignment.

present with a reasonably sized HCP. An experimental study of the ambient noise level as a function of Ca d-state energy is shown in Fig. 4.3. In this experiment, the frequency of the dye laser that produces Rydberg d-states is scanned in the presence of a focused HCP, and ionization is monitored. A $40V/cm$ field pushes ions toward the detector, and also ionizes Rydberg atoms above $n = 54$. The results of this experiment, indicate that above $n = 39$, Rydberg d-states are efficiently ionized by the ambient noise produced by the $6.5kV$ biased wafer.

The curves plotted in Fig. 4.4 are typical of HCP ionization curves, measured before and after every experimental measurement. They are measured at a constant laser energy by scanning the bias applied to the GaAs wafer, and recording the ionization level. Saturation, or ionization fraction equal to unity is approximated as the curves tend to level off at large impulses. It is important to note that signal to noise levels of $10:1$ are typical, so the usual experimental approach is to make several measurements throughout the day and average the results together to produce curves like those in Fig. 4.4. To calibrate the HCP impulse

strength, A, ionization scans are recorded at three different laser energies corresponding to states where $n = 25, 28,$ or 30. The experimental knob turned during a scan is bias voltage. Once the voltages that produce the 50% ionization level for all three laser energies are determined, a single scale factor is found that calibrates the voltage axis (laboratory units) into impulse strength (physical units). Since the ambient noise of the HCP tends to ionize with similar efficiency to the peak-HCP field above $n = 39$, an extraction pulse of $F = 150V/cm$ is used to push ions toward the detector in these measurements. The final energy then, $E_f = -2\sqrt{F}$, for this particular choice of extraction field yields that $n_f = 39$, using the standard relation between n and E. This choice of extraction field is important to ensure that the energy transferred to the electron by the HCP is well-defined. The 50% ionization levels in Fig. 4.4 are at $A = \sqrt{-2\Delta E}$, where the total energy transfer required to HCP ionize an electron with energy $E_0 = -1/2n^{*2}$ at the 50% ionization level is $\Delta E = -2\sqrt{F} - E_0$. Determination of the 50% ionization level is of course dependent on an accurate determination of 100% ionization. In practice, it is difficult to accurately determine the maximum ionization level attained, since saturation is not reached. The large signal to noise levels we see for large kick strengths are also problematic. Typically, we find that the curves in Fig. 4.4 reach about 0.9 ionization fraction, however, this number for the ionization fraction factor is only an educated guess at this point. The ionization-fraction factor and the determination of it is discussed further in Sec. 4.4 where we discuss impulsive momentum retrieval. One ionization-fraction factor is determined for all data taken on a given day.

As a final note about verifying the quality of HCPs produced in the lab, it has been found previously that HCP generation is optimized when the wafer is illuminated with $40\mu J/cm^2$ of $780nm$, $100fs$ laser light [66]. Measurement of this functional dependence, demonstrated in Fig. 4.5 helps to establish that the HCP generation is optimized.

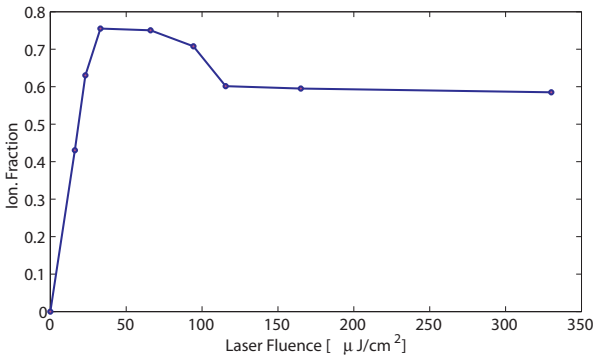

Figure 4.5: HCP ionization as a function of short-pulse laser fluence. The atomic state is $25d$ of Ca. Laser energy is varied by inserting neutral density filters into the $780nm$ beam path and the ionization is recorded. These results are consistent with previous measurements which showed that there is a HCP generation maximum at $40\mu J/cm^2$ [66], and aid in verification that ionization is caused by the HCP and not longer timescale noise.

4.3.3 Transient Attenuator Studies

A transient attenuator is used to study HCP ionization in a time-resolved fashion [55]. The transient attenuator is a GaAs wafer typically positioned between the parabolic mirror and the experimental detection region. When illuminated with ultra-short pulse laser light the transient attenuator is conductive. If the laser pulse arrives at the attenuating wafer after the HCP, the THz pulse passes through the wafer. If the laser pulse arrives at the wafer before the THz pulse has completely passed through it, part of or the entire HCP may be reflected by the transient attenuator.

In previous experiments by Tielking *et al.* [55], it was observed that after the main lobe of the HCP, there is a $\sim 5ps$ long opposite-polarity tail. Additionally, there is a reflection pulse delayed by $11ps$. The transient delay studies presented here do not indicate any obvious features in the HCP beyond the sharp, $1.5ps$ rise in ionization resulting from the main pulse of THz radiation passing through the transient attenuator. The negative tail is expected to be small, so perhaps that explains why it was not detected in these experiments. However, while the measurements presented here are inconsistent with the measurements of Ref. [55], they are not inconsistent with other measurements of the same effect [75].

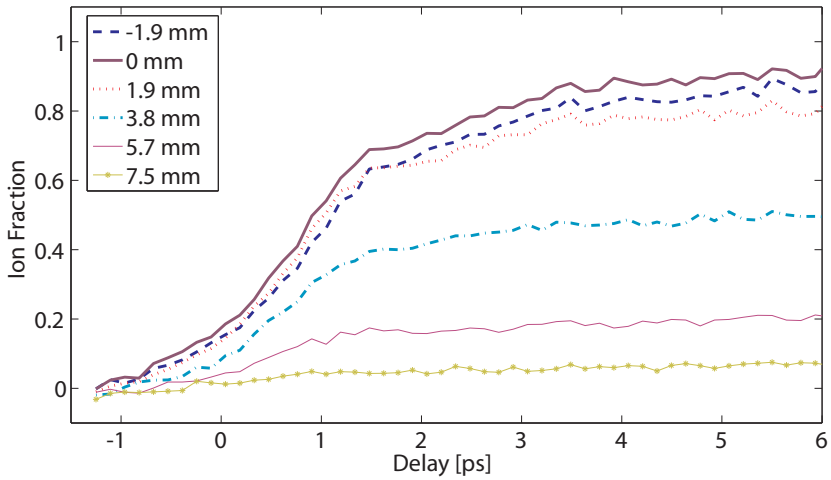

Figure 4.6: HCP ionization as a function of delay between the HCP and ultra-short pulse laser light incident on a transient attenuating wafer where $n = 30$. The ultra-short pulse light gates the HCP by making the GaAs attenuating wafer a conductor. Shown are the ionization levels as a function of delay at different spatial positions in the THz beam.

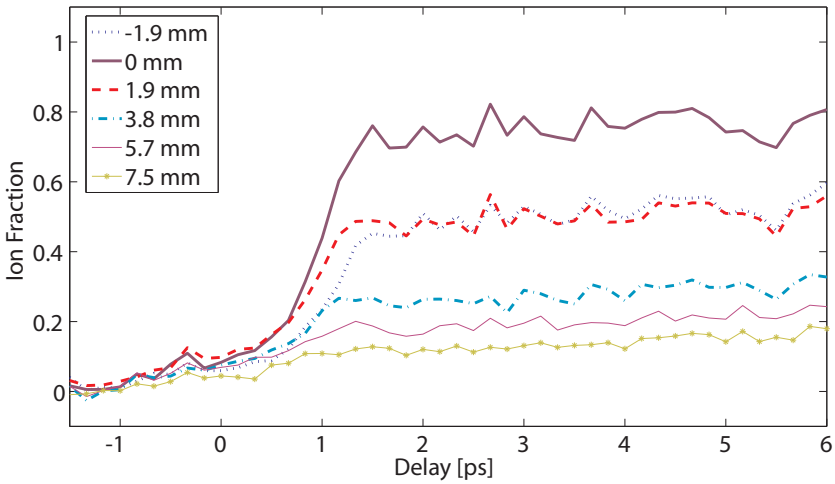

Figure 4.7: HCP ionization as a function of delay between the HCP and ultra-short pulse laser light incident on a transient attenuating wafer where $n = 25$. Shown are the ionization levels as function of delay at different spatial positions in the THz beam. The curves here and in Fig. 4.6 do not indicate temporal variation in the HCP as a function of the spatial position.

The two goals of these HCP ionization studies are to observe the characteristics of the HCP temporally, as discussed in the previous paragraph, and spatially, where we verify that the wings of the focused THz beam are not delayed relative to the center of the beam. Verification of this ensures that the experimental technique where the spatially inhomogeneous field profile is used to measure several HCP ionization levels in one laser shot is, a time-resolved probe of electronic dynamics that occur on time-scales longer than the HCP duration. The results of the transient attenuator studies are shown in Figs. 4.6 and 4.7.

The spatio-temporal profile of ultra-short pulse THz radiation has been studied previously by Budiarto *et al.* [57] and Gürtler *et al.* [59]. The results of Budiarto indicate that the off-axis portions of the focused THz radiation are significantly spread out in time, for instance at $3.81mm$ off-axis the pulse is nearly $4ps$ wide. Gürtler's measurements indicate similar results, namely that $2mm$ from the beam axis, the pulse is about $2ps$ wide. Both results are supported by near-field diffraction calculations using their specific experimental parameters. The results shown in Fig. 4.6 and 4.7 indicate that, to within the resolution of our experiment, the off-axis HCP has the same pulse width as the on-axis pulse. A possible explanation for the discrepancy between our measurements and the previously published data is that the THz beam in our experiment is not very well focused. Gürtler *et al.* shows that although a focused beam of THz radiation does tend to spread out in time, the unfocused beam does not. The measurements in Sec. 4.3.1 indicate that the parabolic mirror has a focusing effect on the THz radiation, however, the beam does not seem to be tightly focused [84, 59]. Partially, this is expected because the wavelengths of THz radiation are very long and thus are diffraction limited to a relatively large spot size. Still the beam-waist that is measured is larger than expected from an elementary diffraction calculation [84]. It is also unclear if the GaAs wafer should be considered as a source of collimated radiation or as a divergent source. In the later case, the parabolic mirror is expected to collimate the beam

rather than focus it. In conclusion, whether the beam of THz radiation is actually focused or more approximately collimated, it is apparent from the ionization studies presented in this section that the HCP beam may be used to conduct a time-resolved measurement of the an atomic state with characteristic timescales longer than $1ps$.

4.4 Impulsive Momentum Retrieval

Impulsive momentum retrieval (IMR) is a technique where HCP ionization measurements are analyzed to recover approximate momentum distributions of the ionized atomic state [6]. Assuming that a HCP's pulse duration is infinitely short, a classical picture of the HCP/electron interaction is that the HCP provides the electron an impulsive kick in the pulsed field direction. Before the HCP kick the electron's energy is,

$$E_i = \frac{\overrightarrow{p}^2}{2} + V(\overrightarrow{r}). \tag{4.1}$$

After the impulsive kick the electron's energy is,

$$E_f = \frac{(\overrightarrow{p} + \overrightarrow{A})^2}{2} + V(\overrightarrow{r}), \tag{4.2}$$

where $A = -\int F(t)dt$, and $F(t)$ is the magnitude of the HCP's electric field. Calculation of the total energy transferred when the electron is ionized ($E_f \geq 0$) by an impulsive kick yields that,

$$-E_i \leq \overrightarrow{p} \cdot \overrightarrow{A} + \frac{\overrightarrow{A}^2}{2}. \tag{4.3}$$

Rearranged where $\overrightarrow{A} = A\hat{z}$ Eqn. 4.3 gives:

$$p_z \geq \frac{1}{A}(-E_i - \frac{A^2}{2}). \tag{4.4}$$

This equation says that if an electron has momentum equal to or greater than p_z, then at the given electron energy, E_i, the electron will be ionized by a kick of magnitude A. Very

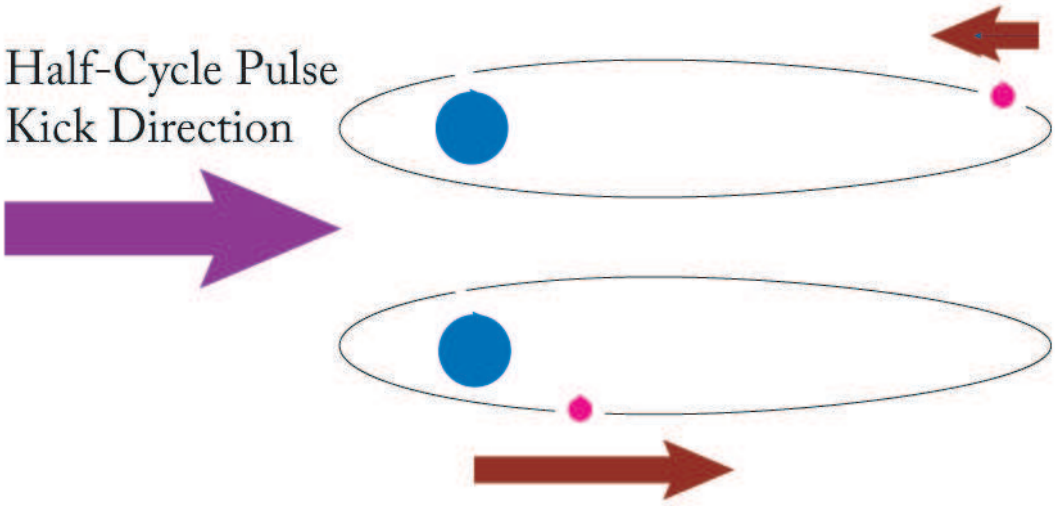

Figure 4.8: Schematic diagrams of the HCP interacting electrons in a couple of different configurations. The upper illustration shows the electron near the outer turning point of the classical orbit going toward the ion-core. The lower illustration shows the electron near the ion-core rapidly moving toward the outer turning point.

large impulsive kicks ionize all electrons present. Very small impulsive kicks will not ionize any electrons at all. In between these two extremes the momentum distribution is mapped out. For two examples, consider the classical pictures of an electron near the ion core, with momentum either parallel or anti-parallel to the kick direction. Near the ion core, the magnitude of the electronic momentum is maximum. Only a small kick is required to ionize the electron when its momentum is parallel to the kick direction. By contrast, a large kick is required to ionize the electron when its momentum is anti-parallel to the HCP field axis. A third case to consider is when the electron is at the outer turning point of the classical orbit, and its momentum is zero. Here Eq. 4.4 yields that $A = \sqrt{-2E_i}$. In this case the probability for ionization by a HCP kick in the $+\hat{z}$ direction is equal to the probability for ionization by a HCP kick in the $-\hat{z}$ direction. For this reason, the case where the electron is near the outer turning point is usually referred to as the 50% ionization level [5].

The relevant information in IMR is not the ionization fraction $I(A)$, but the derivative of ionization dI/dA, since this represents the probability density of the electron projected onto

the $\widehat{A}$-axis. Using Eqn. 4.4 at a given value of A, dI/dA is scaled by dA/dp into momentum space, where dI/dp is the electronic momentum distribution projected onto the $\widehat{A}$-axis.

In traditional IMR experiments [6] a HCP ionization curve, for example one of the six in Fig. 4.4, is measured, and numerical derivatives of the ionization curves are calculated. In principle, a momentum distribution can be recovered from a single ionization curve. In practice, it is experimentally difficult to accurately map out the distribution when the kick strength $A > \sqrt{-2\Delta E}$, where ΔE is the energy required to ionize the electron. However, by taking two separate scans, for example a $+z$-HCP scan and a $-z$-HCP scan, a single momentum distribution is recovered by combining the two data sets. Typically through IMR, a $+z$-HCP scan measures the momentum distribution over a range $-0.01 < p_z < \infty$ and a $-z$-HCP scan measures the momentum distribution over a range $-\infty < p_z < 0.01$. There is a region of overlap between the two sides of the momentum distribution, and by finding the ionization-fraction factor, discussed previously in Sec. 4.3.2, the overlap between the two sides is maximized. Typically, the ionization-fraction factor is determined to be ~ 0.9. We reiterate, that one ionization-fraction factor is determined for all data taken on a given day.

Unfortunately, numerical differentiation of $I(A)$, as mentioned in the previous paragraph, tends to amplify experimental noise, rendering results from this approach difficult to interpret. Amplitude modulation-IMR [74, 31] follows the mathematical formalism described in this section, however, the derivative signal is recovered directly by an experimental technique. The modulation techniques employed in the experiments presented in this dissertation are discussed in Chapters 5 and 6. To conclude this chapter and whet the reader's appetite for the following chapters, we remark that direct measurements of the derivative provide for significant improvements to the IMR technique.

Chapter 5

Probing Stark Momenta

5.1 Introduction

Half-cycle pulse ionization provides a time-resolved method to monitor the evolution of arbitrary electron wave-packets though impulsive momentum retrieval, where IMR probes an electronic momentum distribution projected along any Cartesian axis [5, 67]. Since its introduction, IMR has been successfully applied to measure electronic momentum distributions of eigenstates and wave-packets, in the later case providing a time-resolved probe of the electron. Much has been achieved through the application of IMR, for example, several experiments [5, 8, 68, 69, 70, 85] have used HCPs to probe the electronic velocity in a particular direction versus the opposite direction. However, IMR is capable of resolving smaller structures of the momentum-space probability distribution, possibly even structure that reflects the wave nature of an electron [78]. The full utility of IMR for measuring nuances of the probability distribution requires an accurate measurement of the change in ionization as a function of HCP impulsive-kick strength. Numerical derivatives of the ionization versus kick strength curve tend to amplify experimental noise, rendering this straightforward approach inaccurate. A better approach is to use amplitude modulation impulsive momentum retrieval

(AM-IMR), recently demonstrated by Zeibel *et al.*, which provides a direct measurement of the derivative signal [74].

This chapter describes an experimental investigation of Stark states using improved AM-IMR techniques. Experiments presented here capitalize on the technique of Zeibel *et al.* by exploiting the spatial variation of HCP field strength across the terahertz beam profile, to simultaneously measure HCP ionization yield over a continuous range of kick strengths. In addition to providing a direct measurement of the derivative signal, the new techniques do not require lengthy scans of the HCP field strength, since all necessary field strengths are recovered in one laser-shot. This reduces errors associated with experimental drift that often made previous measurements difficult [67]. Furthermore, the new techniques remain useful, in principle, for performing time-resolved experiments (see Sec. 4.3). Stark eigenstates are useful for AM-IMR benchmark experiments for several reasons: i.) eigenstates have well-defined energies so that blurring of the momentum image due to the uncertainty principle is minimized [5, 78] ii.) direct comparison with theory is possible since the momentum distributions are given by the projection of the wavefunction in momentum space [86] [20], iii.) states with nearly zero dipole moments, have a notch in the projection of the momentum distribution along the Stark field axis providing structure within the momentum distribution that is resolvable upon projection to the p_z-axis.

In the following sections the experimental techniques are discussed, and results for the p_z-distributions of Stark states are described. Next, for comparison purposes computational methods for Stark states are described. The experimental results are further discussed with interpretation facilitated by a wave-packet propagation model.

5.2 Experimental Procedures

5.2.1 Apparatus

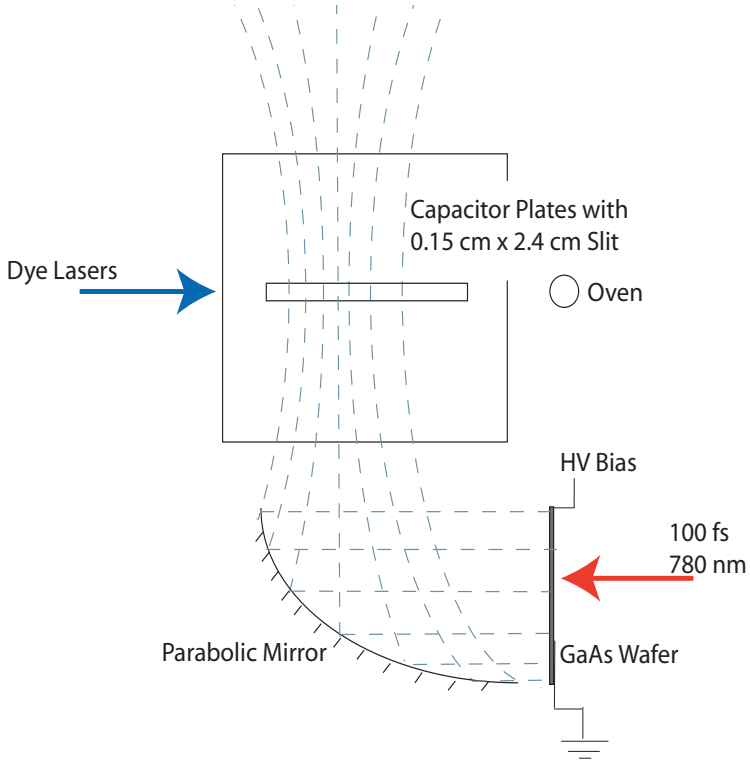

Figure 5.1: Schematic diagram of the experiment. The HCPs are produced with a GaAs wafer, and the beam of HCP radiation is focused on Stark atoms produced between the capacitor plates.

In the experiments two nanosecond dye-lasers excite a thermal beam of $4s4s$ Ca atoms, through the $4s4p$ intermediate level to a Stark state $4snk$, where either $n = 27$ and $k = 19$ or $n = 28$ and $k = -26, -24$, or -6. The first dye laser is polarized vertically, and the second is polarized horizontally. Thus $|m| = 1$ for the excited state. We have chosen to excite $|m| = 1$ rather than $m = 0$ states because the relative amplitudes of the various k-labeled states in the Stark manifold are more evenly distributed as m grows larger [49]. The Stark state excitation is performed using a narrow-band dye-laser ($0.15cm^{-1}$). The separation between Stark states shrinks at higher energies; subsequently the dye laser bandwidth limits

how high of an energy level we can excite and still drive transitions to only one Stark state. The excitation is performed in a static-electric field of $104V/cm$ generated between two aluminum plates separated by $2cm$. At this field strength the Stark manifolds of the $n = 27$ and $n = 28$ states have not yet crossed, and adjacent k-states are separated by $\sim 0.39cm^{-1}$ [20]. Approximately $20ns$ after their creation, the Stark atoms are exposed to a $0.5ps$ HCP [66]. Ions produced by the HCP are projected by the static electric field through a narrow slit in the upper capacitor plate into an imaging detector (MCP, Phosphor screen, and CCD camera). Ionization as a function of HCP field strength is monitored and momentum distributions are recovered using impulsive momentum retrieval.

The HCP is generated by illuminating a biased $2cm \times 2cm$ GaAs wafer with $40\mu J/cm^2$ of short-pulse light from the Ti:Sapphire laser system [66]. Peak HCP electric field strength is varied as a function of the bias on the GaAs wafer. The resulting HCP is collected with a parabolic mirror and a $\sim 1cm$-waist beam of terahertz radiation intersects the atomic beam under the narrow slit in the upper capacitor plate, illustrated in Fig. 5.1. The spatially varying field profile of the HCP beam provides all field strengths required to measure an ionization versus HCP impulse strength curve in one-laser shot. A typical ionization curve versus position is shown in Fig. 5.2, where the calibration of position versus HCP impulse strength is achieved within the interaction region using the ionization probability curves for Rydberg d-states in Ca [77, 67].

5.2.2 AM-IMR using spatially sensitive detection

While, all ionization, $I(A)$, where $A = -\int F dt$, is provided in one laser-shot, the derivative dI/dA is measured by amplitude modulating the GaAs bias voltage over time [74]. By monitoring the ionization as a function of time, when the temporal variation is caused by a sinusoidal amplitude modulation, dI/dA is recovered through a Fast-Fourier Transform

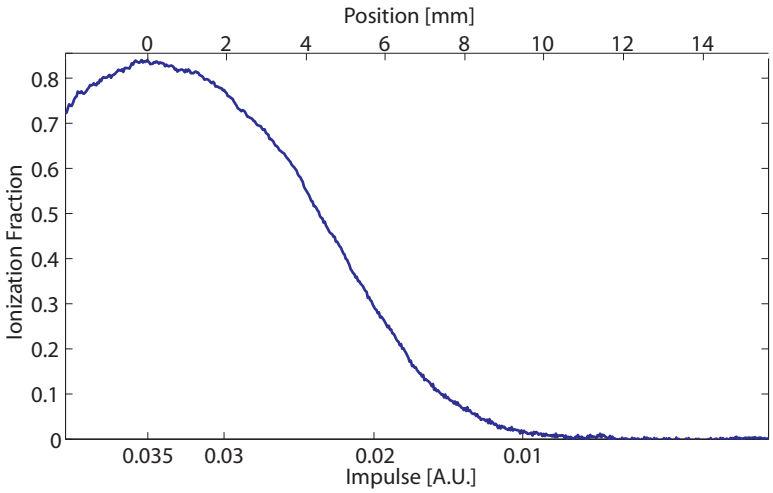

Figure 5.2: Typical HCP ionization curve as a function of position with respect to the HCP beam axis centered at $0.0mm$. The atomic state ionized in this measurement is $n = 28$ $k = -26$ with $V_0 = 6.5kV$.

(FFT), using the formula:

$$\frac{dI}{dA} = \frac{1}{2AN} \sum_{|f_0-\Delta f| \leq f \leq |f_0+\Delta f|} G(f), \tag{5.1}$$

where $G(f)$ is the spectral amplitude at the frequency f, f_0 is the modulation frequency, Δf is the band of nearby frequencies that are included in the summation, and N is the total number of points in the Fourier transform. A typical time-scan and its FFT are shown in Fig. 5.3. The laser system operates at $15Hz$, and the modulation frequency is always kept low enough that several shots are averaged per-point in the time scan. Additionally, to avoid under sampling, it is necessary to collect several points per modulation period. Within these constraints, various frequencies have been used successfully, including $0.02Hz$, $0.04Hz$, and $0.08Hz$, and there is no reason why other frequencies less than the laser rep-rate could not be utilized as well. Typically, we collect data with a $6.5kV$ average-bias on the wafer, and a $0.15kV$ peak-to-peak modulation. Previously, Zeibel [31] used larger modulation voltages. However, since our goal is to make a very accurate derivative measurement, it is important that the modulation amplitude (ΔA in units of impulse) be as small as is feasible, since

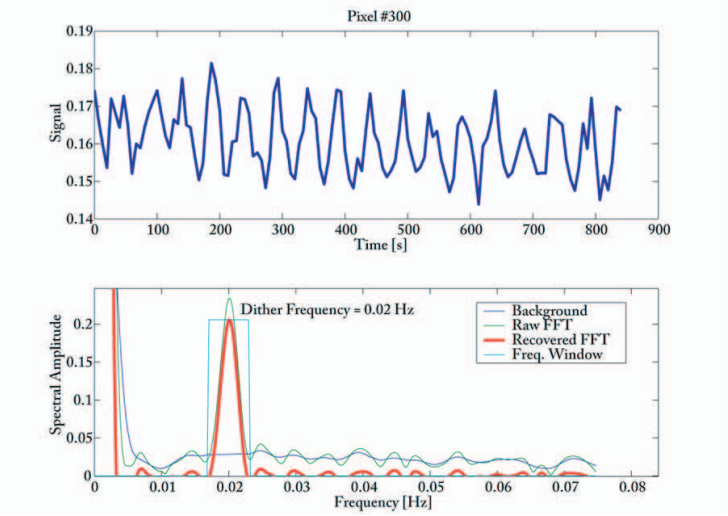

Figure 5.3: (upper plot) typical time scan recorded at a particular position (lower plot) the FFT of this time scan. The position is at camera pixel 300, and is near the FWHM of the HCP beam. The modulation frequency, f_0 is $0.02Hz$. The summation in Eq. 5.1 is performed over frequencies in the rectangular Freq. Window. The Background is subtracted off of the Raw FFT signal, since this Background contributes power at the modulation frequency, but appears not to have any specific frequency dependence [31].

this limits the experimental resolution. Unfortunately, small modulation amplitudes also results in a smaller signal to noise ratio, and because of the noise, power may be aliased into or out of the modulation frequency. So, although Eq. 5.1 provides a direct measure of the derivative signal, in practice we find that the recovery is not perfectly efficient, and usually power is modulated out of the modulation frequency. We have a good way to check this because if the efficiency were perfect, the derivative signal, integrated over A should equal the ionization signal, $I(A)$, which is the DC data in a time scan. Figure 5.4 shows typical ionization curves measured at both $f = 0$, the DC data, and integrated from the measured signal at the modulation frequency, the AC data. The signal size and shape of the DC data is set by the impulse calibration, discussed in Ch. 4. A single efficiency correction factor is determined by minimizing the least-square difference between the DC and integrated AC measurements at all A. Typically the efficiency correction factor is between 1.0 and 1.1.

Through the impulse approximation, the momentum distribution along the HCP field axis

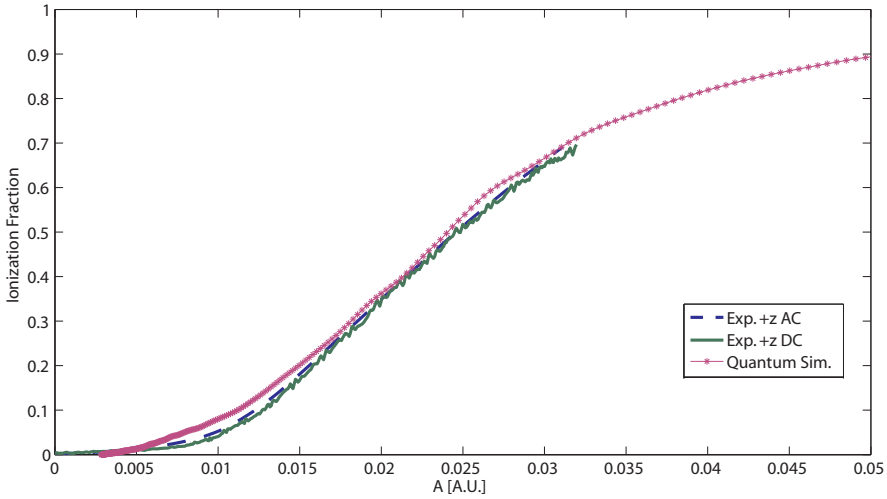

Figure 5.4: Typical ionization curves. The solid line is measured at the DC frequency of a time scan, like the one in Fig. 5.3, but at several kick strengths. The dashed line is the integrated derivative signal, where the derivative signal is measured at the modulation frequency (labeled here AC). This data is for the $n = 28, k = -26$ energy level, and the efficiency factor is 1.07. The theoretical curve is shown for comparison, and the computational method that produces this curve is discussed in Sec. 5.3.2.

is recovered. Unfortunately, at large peak-HCP field strengths this approximation breaks down [79, 67]. To avoid large HCP field effects, momentum distributions are measured at impulses on the order of and less than $1/\sqrt{-2\Delta E}$ in both the $\pm p_z$-directions. Modulation scans using kicks in both directions are spliced together, using a weighted average of the overlapping data points to form the complete distribution [31, 101]. It is desirable that except for the HCP polarity, the $+p_z$ and $-p_z$ scans are identical, so in addition to the sinusoidal modulation, the GaAs bias polarity is reversed periodically, at the switch frequency, providing the complete momentum distribution, both the $+p_z$ and $-p_z$ parts in one scan. To switch the bias voltage polarity, we modified a standard voltage pulser, which was previously discussed in Ch. 2. In the usual voltage pulser circuit a 2-pole mechanical switch is used to control the bias polarity. In the modified pulser (see Fig. 5.5), a relay replaces the mechanical switch. The relay is controlled by a $12V$ $0.029mHz$ square wave produced by a Kepco Power op amp, where the square wave input to the op amp is generated by a "flip-flop biting its

tail", backed by a divide-by-N clock triggered at $15Hz$ [87]. Typically the switch frequency is chosen so that neither it, nor its harmonics are spectrally close to the modulation frequency, and both $0.029mHz$ and $0.015mHz$ square pulses were used successfully.

Although the ionization differences at the switch frequency can be recovered with the same formula used for the derivative signal, the data from the two different polarities are separated into two data sets using a computer algorithm to determine, given the switch frequency and notes taken while the data is recorded, which data points of a scan correspond to which HCP polarity. Each of the two data sets are next Fourier transformed, as described previously, to recover dI/dA for each bias polarity. Typically, Stark states with large dipole moments showed ionization differences when probed with opposite polarities of HCP. The observed effect is small, consistent with the measurements of Stark states at lower n's by Jones *et al.* [76] where the effect was described as a result of the electron interacting with the core, because the HCP was not acting perfectly impulsively. The asymmetry in HCP ionization is also dependent on the Stark state's orientation, where the asymmetry is found to be proportional the state's dipole moment [76]. This ionization asymmetry was not observed previously by Jones *et al.* for the higher-n states that are measured in this thesis. However, another difference between the present experiments and those of Ref. [76] is that Jones *et al.* used the standard approach to HCP ionization experiments, of scanning a voltage over time, rather than the modulation techniques we employ here. It was verified that ionization differences are not detected for the higher-n states, when the conventional voltage scan technique is used. This discussion points to the consistency with the experiments of Jones *et al.* when the standard IMR techniques are utilized, and the higher accuracy of the improved IMR techniques presented here. Ionization from Stark states with small dipole moments do not depend on the HCP polarity, at least to the accuracy we measure, and as such these scans are not separated into two different sets, but treated as two identical data sets.

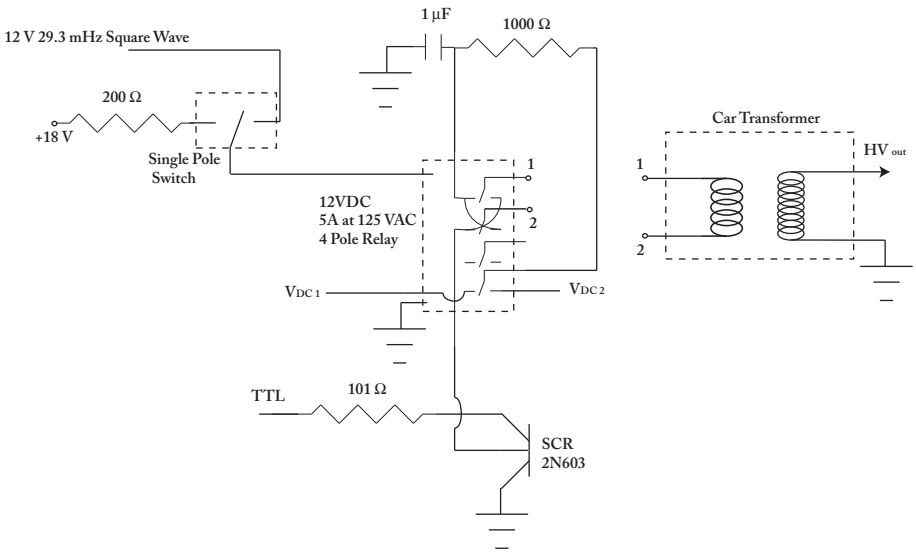

Figure 5.5: Schematic diagram of the field pulser used to bias the GaAs wafer in this experiment. The Single Pole Switch allows for operation in a standard mode (useful for HCP calibration scans), or with a control pulse, labeled here as a $12V$ square wave. Poles 1 and 2 of the relay are cross wired with points 1 and 2 of the car transformer, switching the polarity of the high-voltage output. V_{DC1} and V_{DC2} can be different, but are in fact equal in the experiments presented in this chapter.

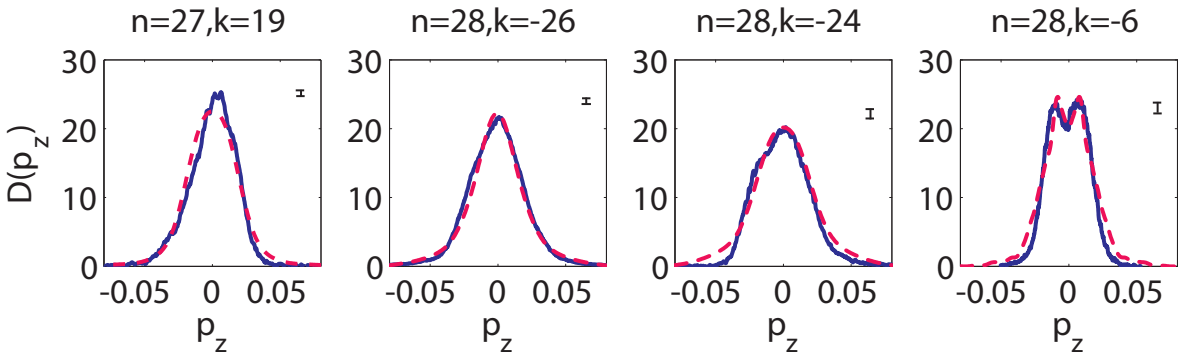

Figure 5.6: Measured (solid line) z-momentum distributions for several Stark states. Results from a wave-packet calculation (dashed line), where states are probed through a $500fs$ window are overlaid for comparison. Computational methods are discussed in Sec. 5.3.2.

Figure 5.6 shows the experimentally determined momentum distributions. The $k = -6$ state, has a narrow z-momentum distribution and structure near $p_z = 0$. The large dipole moment states, $k = -26, -24$ and 19 have broad and smooth distributions, evidently without resolvable structure. In the calibration of the impulse-axis, discussed in Ch. 4, the maximum ionization fraction was determined. As a result of experimental errors either in the determination of this ionization fraction, or in the data presented in Fig. 5.6, the experimentally determined approximate-momentum distributions are not necessarily normalized to unity. Typically, the normalization differs from unity by only a few percent, and for consistency in the calibration of the experimental data, we do not re-normalize the measured distributions shown in Fig. 5.6. The data in Fig. 5.6 represent the averages of several different scans taken on a few different days. The error bars indicated are the largest, sample mean variances: $\sigma = \sqrt{\frac{1}{N(N-1)} \sum_i^N (y_i - \bar{y})^2}$, with N equal to the number of independent measurements. The $k = -6$ state has a comparatively large sample mean variance, but we offer two explanations that both contribute here. Firstly, this state has a smaller absolute signal level, $1/10^{th}$ the size as the $k = -26$ state. Secondly, this state has, in comparison with the other measured states, a narrower momentum distribution. The largest valued σ for the $k = -6$ state is found near $p_z = 0.025 A.U.$, where the slope of the distribution is sharp. Notably, the largest mean sample variance near $p_z = 0$, is less than half the size of the error bar shown in the $k = -6$ plot of Fig. 5.6. We estimate the experimental resolution as $0.002 A.U.$, obtained by adding the spatial resolution of the detector in quadrature with the resolution limit from the amplitude modulation technique. With the improved accuracy of the spatially-sensitive AM-IMR technique we resolve the $0.007 A.U.$-wide structure in the $k = -6$ momentum distribution.

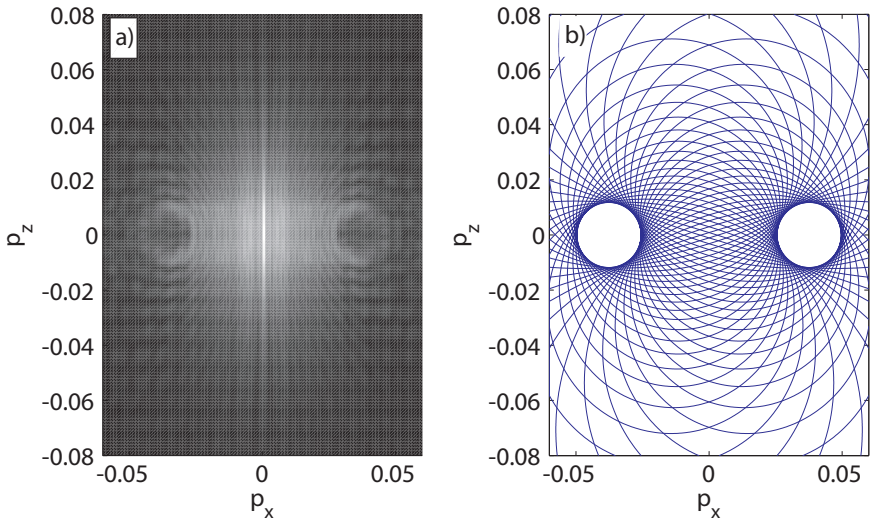

Figure 5.7: a) Calculated $n = 28, k = -6$ Stark state probability is plotted in momentum space b) Trajectories of electrons computed by integration of the classical equations of motion where the energy and $\langle A_z \rangle$ correspond to $n = 28$, $k = -6$.

5.3 Discussion

5.3.1 Momentum Distribution Calculations

For electric fields small enough that different n-levels are not mixed, Stark eigenstates of hydrogen are calculated using the equation:

$$\Upsilon(p, \Theta, \Phi) = \sum_l (-i)^l a_{n,m;l,k} Y_{l,m}(\Theta, \Phi) \int r^2 R_{n,l}(r) j_l(pr) dr, \tag{5.2}$$

where j_l is a spherical Bessel function, $a_{n,m;l,k}$ is a Clebsh-Gordon coefficient, n, l, and m are the principle, angular momentum, and magnetic quantum numbers, and k is the parabolic quantum number, which is proportional to the dipole moment of a Stark state, $\langle z \rangle = 3/2nk$. Two Stark states, calculated using this formula are shown in Figs. 5.7 a) and 5.8 a). The trajectories of these two Stark states' classical analogs are shown in Figs. 5.7 b) and 5.8 b).

Figure 5.9 shows the Stark spectrum of Ca. The Ca $29d$ state has a quantum defect of roughly unity [46], so in the HCP ionization study presented here, where the figure of

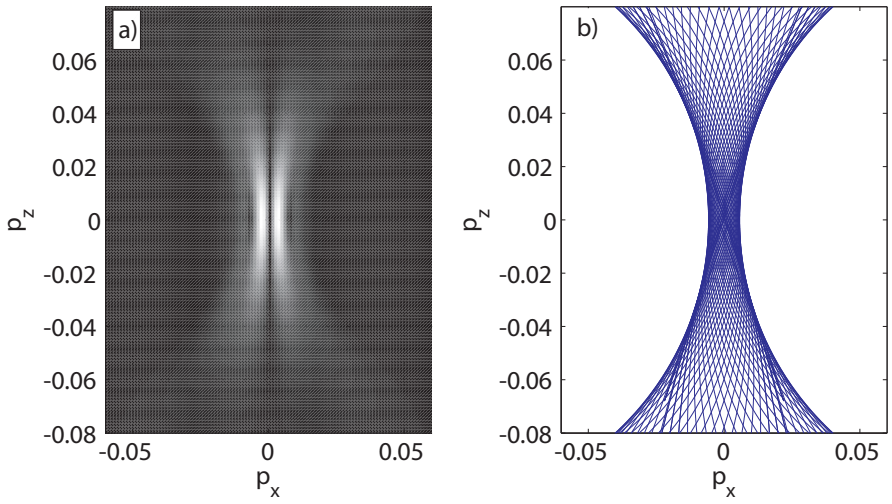

Figure 5.8: a) Calculated $n = 28, k = -26$ Stark state wavefunction in momentum space b) Trajectories of electrons computed by integration of the classical equations of motion where the energy and $\langle A_z \rangle$ correspond to $n = 28$, $k = -26$.

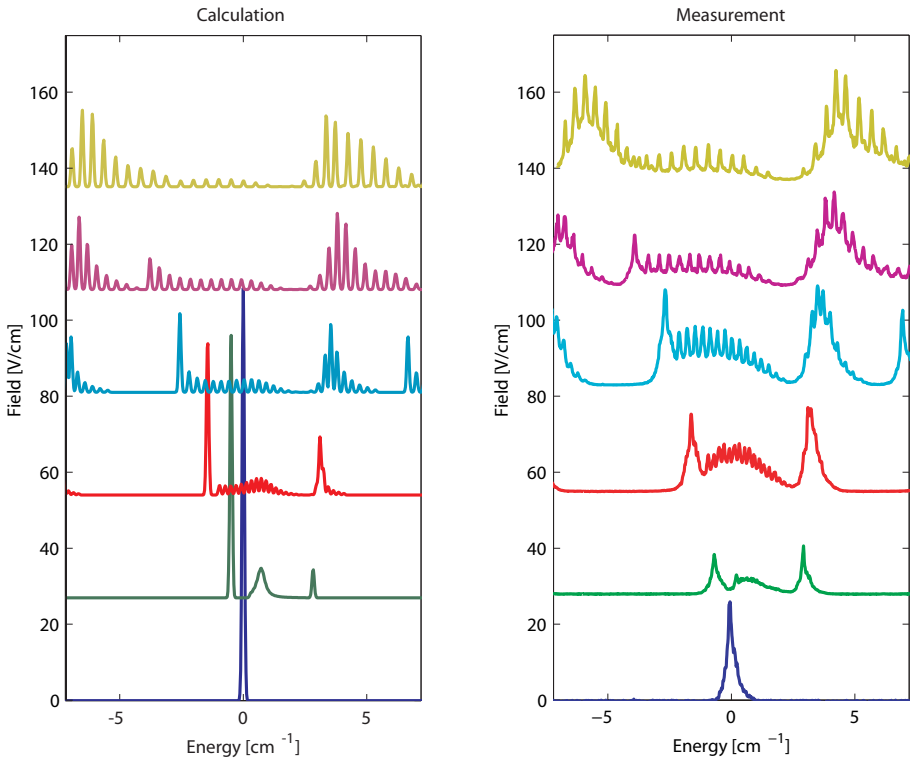

Figure 5.9: Ca Stark Spectra. The energy axis is centered on the Rydberg 29d level. For comparison the calculated Ca spectra are also shown. The measured Stark spectra are shown saturated to bring out the states with smaller signal strengths.

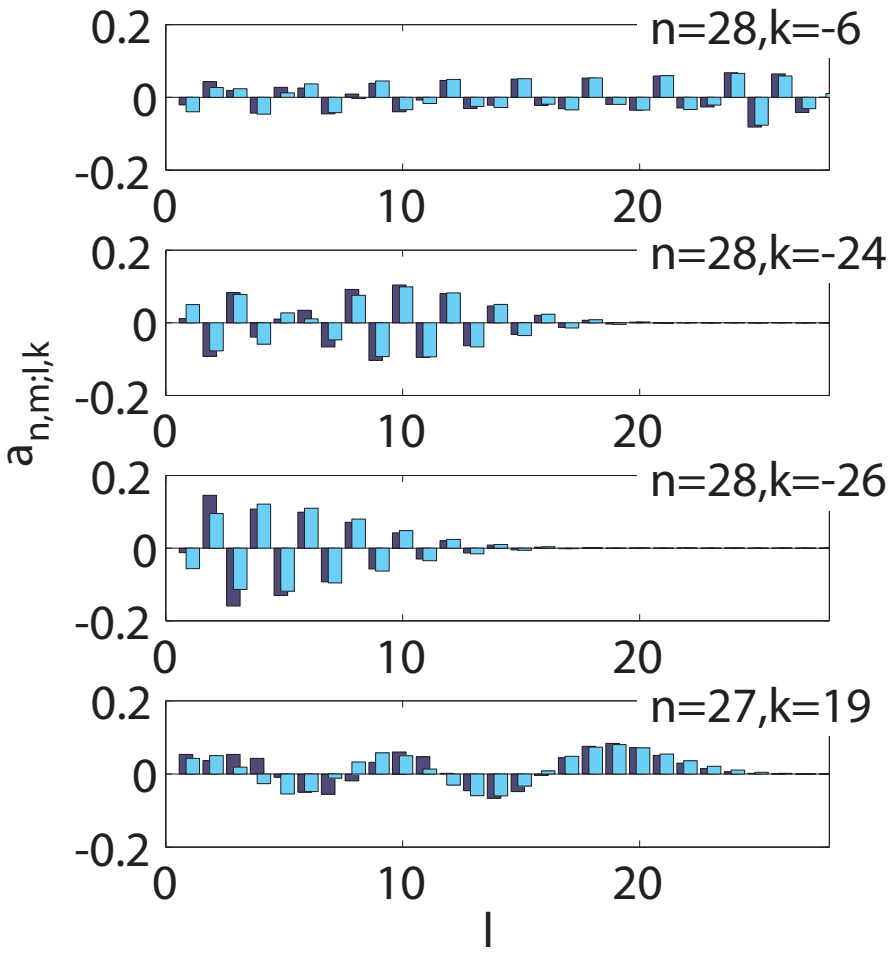

Figure 5.10: Angular momentum character of the Ca(Dark Blue) at $F = 104V/cm$ and H(Light Blue) Stark states for several values of n, k. Over the range of l, distinct similarities between Ca and H are verified.

merit is the effective energy, $29d$ is similar to the hydrogenic state $n = 28$. Calculations of the Ca Stark spectra are shown in Fig. 5.9 for comparison with the measured spectra. The spectra are calculated using the known quantum defects [46, 48], and Zimmerman *et al.*'s [49] computational approach for considering the diagonalized energy matrix. Eigenvectors and values of the energy matrix are calculated as a function of electric field strength. The columns of a unitary transformation matrix $U^{E'}_{E'',l'}(F)$ are the eigenvectors of the diagonalized energy matrix. The oscillator strength for a transition from a low-lying state, E_i, l_i, m_i, to a Stark state, E_s, m_s, is

$$|a_{E_i,E_s}|^2 = \frac{2}{3}(E_i - E_s)|\sum_{E''}\sum_{l''} U^{E'}_{E'',l''}(F)\langle E_i l_i m|rcos(\theta)|E''l''m_s\rangle|^2, \tag{5.3}$$

where the dipole matrix element $\langle E_i lm|rcos(\theta)|E''l''m_s\rangle$ is calculated with a Numerov algorithm [49]. For Ca, $a_{n,m;l,k}$ as a function of energy and static electric field strength is calculated using Eq. 5.3.

While there are some differences between hydrogen and Ca, overall the calculations displayed in Fig. 5.10 indicate that the differences between the Stark states of Ca and the Stark states of H are relatively small at $F = 104V/cm$. The similarities facilitate our calculations of the momentum distributions, using the frame-work in place for hydrogen [20]. Making the approximation that Ca Stark states at $F = 104V/cm$ are basically hydrogenic also facilitates understanding the data from a classical point off view.

The structure in the small dipole moment state is a result of a classically forbidden region in momentum space as seen in Fig. 5.7 b). Classical trajectory calculations are discussed in detail in Appendix A, and will only be discussed briefly here. Classical Stark trajectories are computed by integrating the Hamiltonian of an electron launched with $l = 0$ into a combined static-electric and Coulomb field. The launch angle, with respect to the static field axis specifies the dipole moment of the classical electron, where the time averaged z-component of the Runge-Lenz vector, $\langle A_z\rangle$ is a constant of the motion [47]. Classical

representations of the states, shown in Figs. 5.7 b) and 5.8 b) are determined by matching $\langle A_z \rangle$ and energy to those in the quantum representations. The electron's angular momentum precesses, but is constrained to be $l \leq \sqrt{n^2 - k^2}$, where $k = n\langle A_z \rangle$. The largest value of angular momentum the classical electron can attain plays a role in determining the area of the forbidden regions in momentum space. Stark states with large dipole moments have significantly larger forbidden regions than states with nearly zero dipole moments, yet, even though they have broader momentum distributions the probability drops off significantly enough at large values of z-momentum, that a notch does not remain visible in the projection of the momentum distribution onto the p_z-axis.

Understanding of the smooth shape of the large dipole moment states is also aided by the classical picture of the momentum space trajectories. However, as is shown in the next section, because the measured momentum distributions tend to be narrower than calculated momentum distributions, a calculation that incorporates the measurement processes is necessary.

5.3.2 Wave-packet Calculation

Previous HCP ionization calculations have studied angular momentum eigenstates [78, 81], wave-packets [79, 80], diamagnetic Zeeman states [82], and the extreme uphill and downhill Stark states in a one-dimensional approximation [80, 81]. However, a complete two-dimensional quantum mechanical calculation of the HCP ionization of an electron in a static-electric field remains a computational challenge. Rather than integrate the Schrödinger equation, we simulate a modified electronic wavefunction by calculating the phase acquired by an electron moving on a classical trajectory during a finite probing window. Our computational approach is similar to Robicheaux's higher-order impulse approximation, which also calculates HCP effects on the initial wavefunction without integrating the Hamiltonian [79].

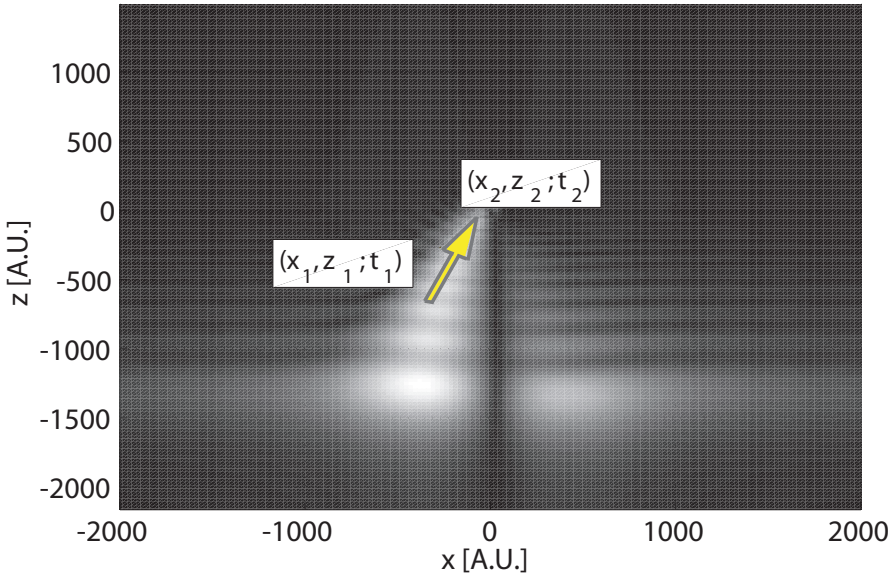

Figure 5.11: Schematic of a trajectory for a large dipole moment state ($k = -26$). Probability density, $P(x, z)$, is plotted for an electron with momentum $p_x > 0$ and $p_z > 0$. Near $(x = 0, z = 0)$ the electron moves a significant distance during the HCP probing window when $t_2 - t_1 \geq 500 fs$.

While our model does not include effects of the HCP field, our approach demonstrates the effect of measuring the electron's inherent motion through a probing pulse time window. The motivation for this approach is that near the atomic core, the velocity of a Rydberg electron is maximized, contributing to the high-momentum wings of its momentum distribution. However, the electron spends very little time near the core, and consequently the impulse approximation breaks down at small r. For example, consider monitoring an electron through a short time window where the electron is on a trajectory that is initially moving toward the core at a high velocity. This electron rapidly orbits around the point $r = 0$, such that by the end of the probing pulse it is already moving back toward the orbit's outer turning point. In the illustrative situation described, where the electron has a large-magnitude positive and negative momentum during its orbit, the *average momentum* measured through a time window may in fact be zero.

To simulate the probability distribution "measured" through a short time window we

consider the Stark state wavefunction given by,

$$\psi(r,\theta,\phi) = \sum_l a_{n,m;l,k} Y_{l,m}(\theta,\phi) R_{n,l}(r), \tag{5.4}$$

which is the analog to Eq. 5.2, but in position space [20]. The wavefunction is initially written in spherical coordinates, but is numerically transformed into cylindrical coordinates. When the z-axis is parallel to the static electric field axis, m is a good quantum number [20]. A two-dimensional representation of the wavefunction is found by taking the wavefunction $\psi(x,z,y=0) = \psi(\rho,\theta,\phi=0)$ for $x > 0$, and $\psi(x,z,y=0) = -\psi(\rho,\theta,\phi=\pi)$ when $x \leq 0$. Using this two-dimensional representation of the wavefunction we calculate trajectories that an electron starting at a position (x,z), will follow during the probing pulse. For $m = 0$ this two-dimensional wavefunction is representative of any two-dimensional wavefunction in a plane parallel to the field axis. For larger $|m|$-values, x and y are coupled through ϕ. However, we argue that for all $|m|$-values, since cylindrical symmetry is retained, the p_z-probability distribution cannot depend on m. It is important to note that this does not hold true for all probability distributions, eg. the p_x- nor the p_y-distributions. However, when calculating the p_z-distribution, the motion in a two-dimensional plane is equivalent to the motion in any other two-dimensional plane.

To calculate a trajectory for the electron starting at (x,z), we need values of p_x and p_z. One problem that arises is that an eigenstate is a standing wave, so at a given point in position space there is no defined direction of motion, and therefore the electron's momentum is not well-defined. Thus, in the calculations we use a wave-packet model where the state wavefunction is represented as a coherent superposition of four orthogonal wavefunctions, $\psi_j(x,z)$, with the momentum constrained to one of the momentum-space quadrants, $j = I - IV$. To calculate $\psi_j(x,z)$ we take the Fourier transform of $\psi(x,z)$, filter-out all probability outside of quadrant j, then apply the inverse Fourier transform to obtain the coordinate space representation. For example, for $j = 1$, in momentum space, only probability with momenta

$p_x \geq 0$ and $p_z \geq 0$ is retained after filtering. In coordinate space, approximate momentum is calculated for $\psi_j(x,z)$ as the expectation value within a small area element on a probability density map, for example the map shown in Fig. 5.11. Next, the classical trajectory for an electron starting at a given position and momentum, is computed and the complex phase, Δ, accumulated during the classical trajectory is approximated as the average phase of all wavefunctions at the coordinates included in the trajectory. The "measured" wavefunction is approximated as $\psi'_j(x,z) = |\psi_j(x,z)|e^{i\Delta}$. Since only the phase of the wavefunction is modified, normalization is retained in this approximation. Other wavefunction averaging methods have been considered, for example, if one calculates the average wavefunction as simply a weighted average of wavefunctions at various coordinates on a classical trajectory, then the wavefunction after the probing pulse is a smoothed version of the original wavefunction. This particular method of averaging is mathematically the same as applying a low-pass filter to the momentum space wavefunction, filtering out the high-momentum wings. This alternative averaging method, does indicate some of the physics we set out to show, however it is not the method used because this particular method of averaging simply throws away probability, and results in un-normalized wavefunctions.

After computing $\psi'_j(x,z)$, the modified wavefunction is Fourier transformed and the p_z-distribution is calculated. Finally, the probability distributions of the modified wavefunctions where $j = I - IV$ are added together and the resulting distribution is smoothed to the experimental resolution, producing the probability distributions compared with measurements in Fig. 5.6, and also shown as a function of probing pulse duration in Fig. 5.12. For completeness, several probability distributions are shown before smoothing in Fig. 5.13. The four modified wavefunctions are orthogonal, so there is no difference between adding the wavefunctions coherently or adding their probabilities. Physically this implies that trajectories do not interfere with each other. By recording the end points of all trajectories we have verified

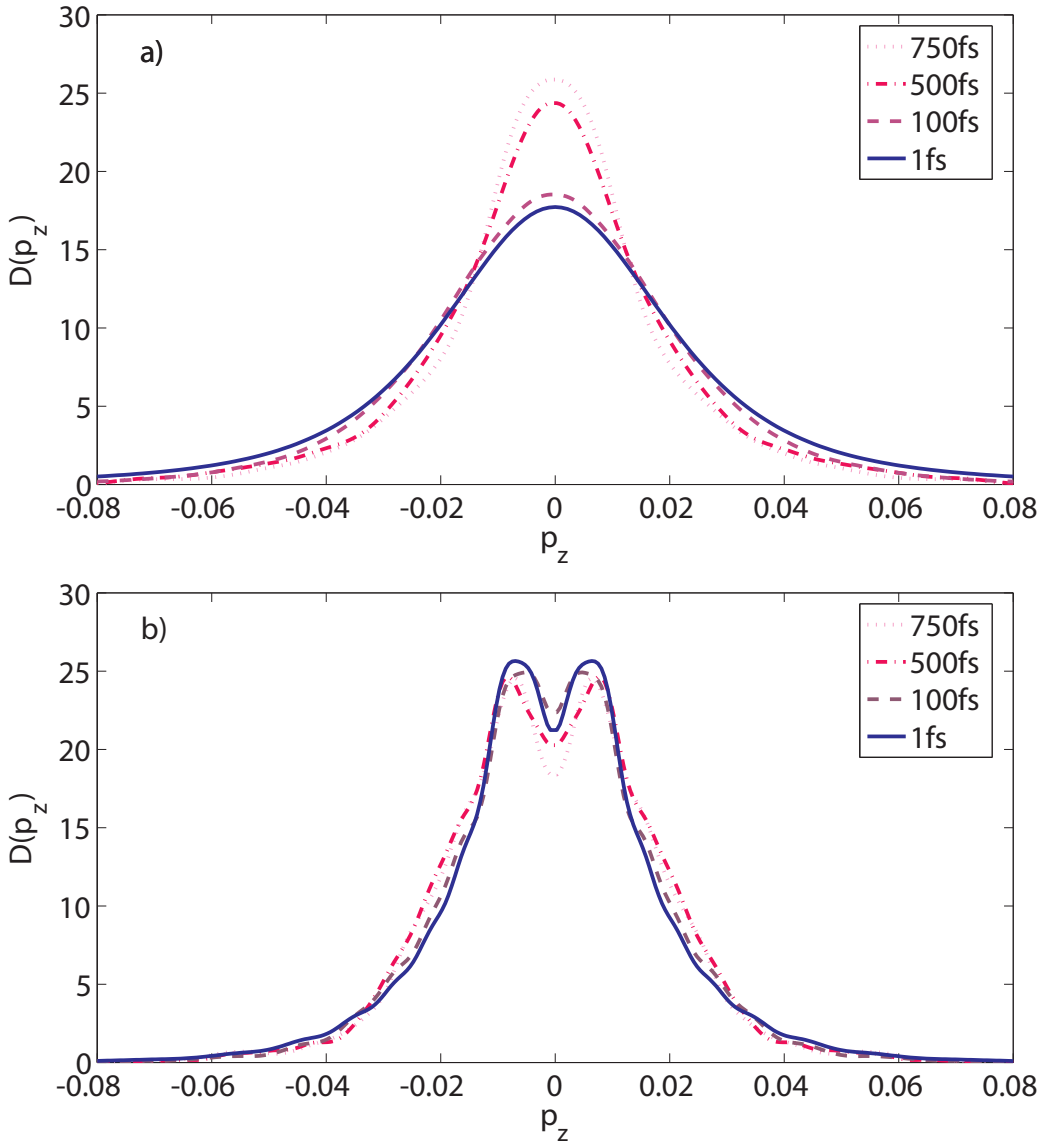

Figure 5.12: Results of wave-packet calculation of a) the $n = 28, k = -26$ state and b) the $n = 28, k = -6$ state through various probing windows. A $1fs$ probing window converges to the results obtained from Eqn. 5.2. A $500fs$ probing window obtains the best agreement with the measurement, which is also consistent with previous measurements of the HCP duration [66].

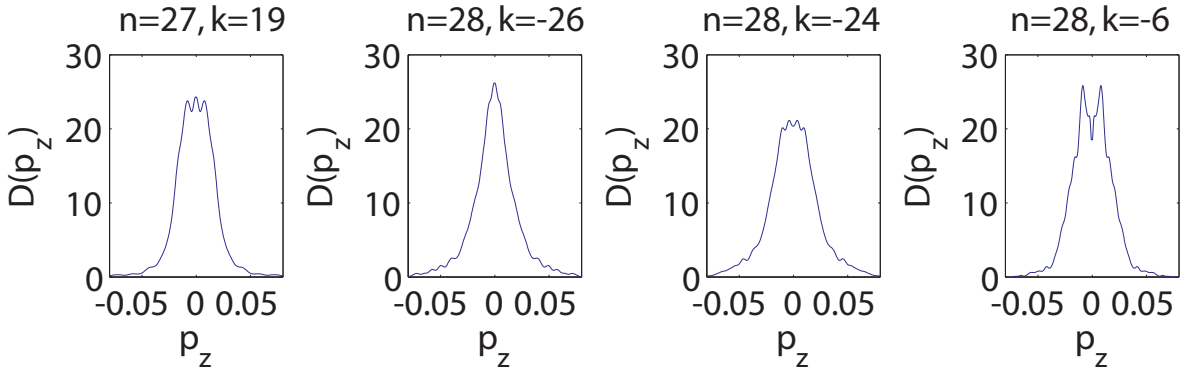

Figure 5.13: Results of wave-packet calculation with a $500fs$ probing window, before a gaussian smoothing to the experimental resolution is applied. These results are shown for comparison with Fig. 5.6.

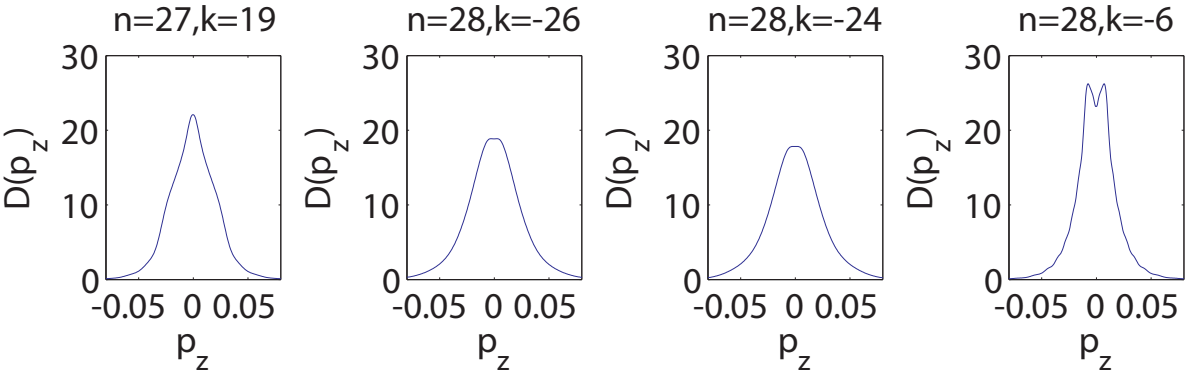

Figure 5.14: Results of wave-packet calculation with a $1fs$ probing window. These results are shown for comparison with Fig. 5.6.

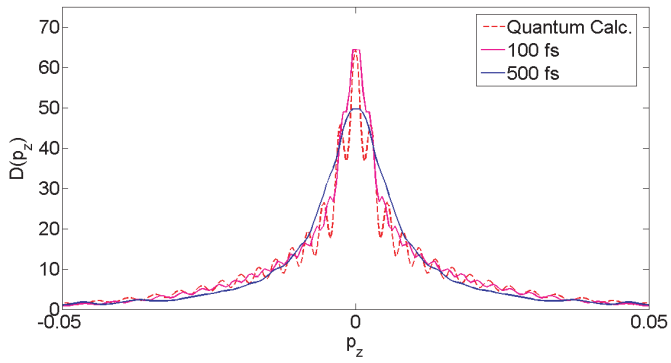

Figure 5.15: Results of the wave-packet calculation of $n = 25, l = 2, m = 0$ eigenstate. Quantum calculations [86] and"measured" distributions through $100fs$ and $500fs$ windows are shown. This graph demonstrates excellent agreement between the computational methods employed here and fully-quantum mechanical calculations of Robicheaux [78].

that no two trajectories end at the same position with different momenta, supporting the idea that trajectories do not interfere.

Results in Fig. 5.12 demonstrate that where there is significant probability in the high momentum wings, that probability is aliased to the central region of the momentum distribution. The calculations using a $500fs$ pulse-width demonstrate very good agreement with the measured Stark state momentum distributions.

As an additional verification of the computational method, this wave-packet propagation model is applied to approximate a momentum distribution for the $l = 2, m = 0$ angular momentum state. We present the calculation of this state because IMR measurements of this state have been studied, experimentally by Jones [5] and numerically by Robicheaux [78]. In Robicheaux's calculation, the Hamiltonian includes a pulsed electric field to mimic the effects of a HCP on a Rydberg electron. Robicheaux integrated the Shrödinger equation and calculated ionization curves. Finally, via IMR approximate momentum distributions were obtained from the ionization curves. Figure 5.15 is provided for direct comparison to Fig.3 of Robicheaux [78], and demonstrates excellent agreement, further verifying our wave-packet propagation method.

In summary, for large-dipole moment states, eg. $k = -26, -24, 19$, where the position space wavefunction is asymmetric about the z-axis, the electron's trajectory takes it rapidly around the small r core. The measurements of these states appear to be pulse-width limited. Also notable is the lack of probability aliasing in the $k = -6$ state, since it has only small probability at large values of p_z.

5.4 Conclusions

Using an improved impulsive momentum retrieval technique, we experimentally measure approximate momentum distributions of Rydberg electrons in a static-electric field. The measurements show structure within the $n = 28, k = -6$ z-momentum distribution that demonstrates the high resolution of the improved IMR technique. A wave-packet model is employed that lends physical insight into the general problem of probing atomic systems with a finite-length pulse. With this computation technique we obtain very good agreement between calculated and measured momentum distributions.

Chapter 6

HCP Ionization Experiments

6.1 Introduction

This chapter details two HCP ionization experiments completed in conjunction with the experiment presented in Ch. 5. In the first measurement presented here, $l = 2$ angular momentum states in Ca are initially excited, then ionized using a HCP. In the second experiment, Stark eigenstates are probed using a HCP where the axis is perpendicular to the static field axis. The original goal of both experiments was an IMR measurement similar to the one presented in Ch. 5, unfortunately with the apparatus we have this type of interpretation proved to be difficult. It is possible that there are aberrant effects in the measurements that we have failed to take into account. However, so far as we understand the problems, the two experiments presented here both suffer from interactions with the HCP that ultimately lead to break down of the impulse approximation. Considering the failures of these two experiments, together with the success of the experiment presented in Ch. 5, is instructive for understanding when HCP ionization may be utilized effectively for IMR, and understanding this point is the primary scientific goal of this chapter.

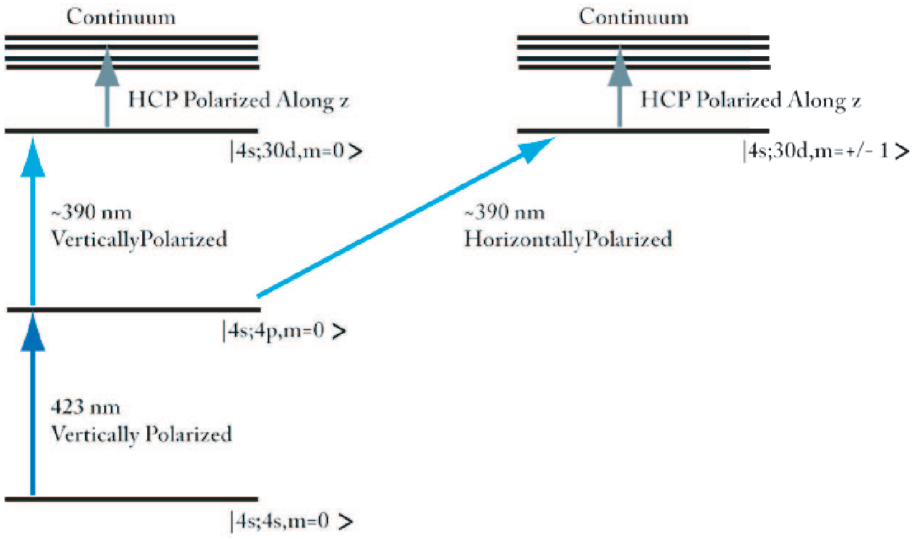

Figure 6.1: Excitation schemes for the angular momentum state measurements. The pre-HCP-driven transitions are not shown in this schematic though they are discussed in the text.

6.2 Angular Momentum States Measurement

Rydberg electron systems are well-described in terms of classical pictures, however the quantum mechanical wavefunction also has interferences that reflect the wave nature of the electron. In many cases these interferences produce only fine-scale structure in the projection of the probability distribution onto one coordinate axis. For example, in the p_z-distributions of Stark states presented in Ch. 5, upon integration over p_x, we did not expect any large-scale structure reflecting the quantum mechanical interferences of the wavefunction, despite that Fig. 5.7 shows a significantly structured momentum space probability distribution. The $l = 2$, $m = 0$ and ± 1 angular momentum states are a unique system where the quantum mechanical states are distinctly different from their classical analogs. The quantum mechanical states have large-scale interferences, most notably a node at $p_z = 0$ when $l + m$ is odd, reflecting a node in the form of the spherical harmonic [78]. Although, not all of the fine-scale structure is expected to be resolvable using IMR, in principle, this pronounced

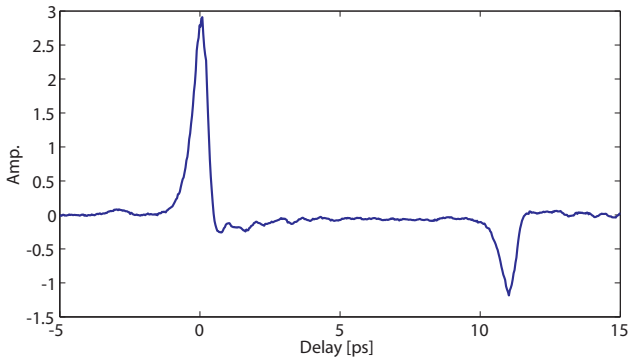

Figure 6.2: The HCP's electric field as a function of delay, measured using the HCP-induced Pockels effect in a ZnTe crystal to attenuate linearly polarized $\sim 100fs$ laser light [56]. A pre-HCP is the small peak around $t = -4ps$. The pre-HCP that is discussed in the text is around $-800ps$ (not shown here). The main peak ($t = 0ps$) is followed by a $\sim 5ps$ negative tail. Around $t = 12ps$ is a reflection pulse from the HCP that results from scattering in the GaAs wafer [55].

node at $p_z = 0$ when $l + m$ is odd is resolvable using IMR [78].

In the experiment d-states are excited from a thermal beam of Ca atoms using two nanosecond dye lasers. The excitation scheme is shown in Fig. 6.1. Light from the first dye laser is polarized vertically, exciting the $4s4s \longrightarrow 4s4p$ $m = 0$ transition. The second dye laser generates 391 nm laser light, that is initially polarized vertically, but is rotated to either horizontal or vertical polarization using a half-waveplate. The $4s4p \longrightarrow 4snd$ $m = \pm 1$ or $m = 0$ transition is driven as a function of the second dye laser's polarization, respectively either horizontal of vertical. When the inner valence electron is $l_v = m_v = 0$, Ca is found to be well described by LS-coupling [46], so the angular momentum eigenstates, $4snl$, are well defined by the quantum numbers l and m. About $20ns$ after the initial excitation, the states are exposed to HCP radiation in basically the same experimental set up illustrated in Fig. 5.1 of Ch. 5. However, it was found that a small amount of HCP radiation arrives in the interaction region $800ps$ before the main pulse [56]. This pre-pulse of HCP radiation is caused by a small pre-pulse in the ultrafast laser system, verified using a scanning autocorrelator [91].

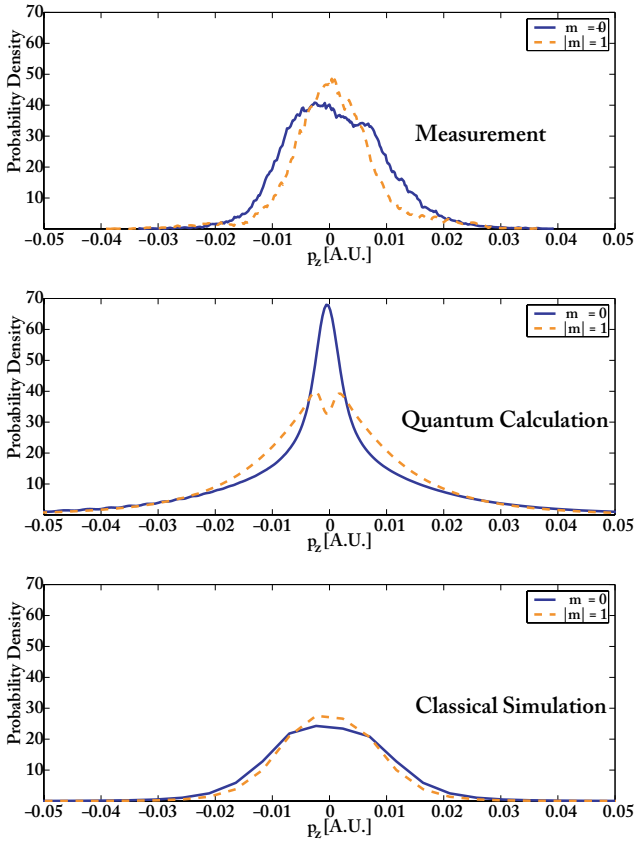

Figure 6.3: p_z-momentum distributions of states initially excited to $l = 2$ either $m = 0$ or ± 1. Classical and quantum distributions for the $l = 2$, $m = 0$ or ± 1 states are plotted to demonstrate their significant differences from each other. The distributions are smoothed to the experimental resolution.

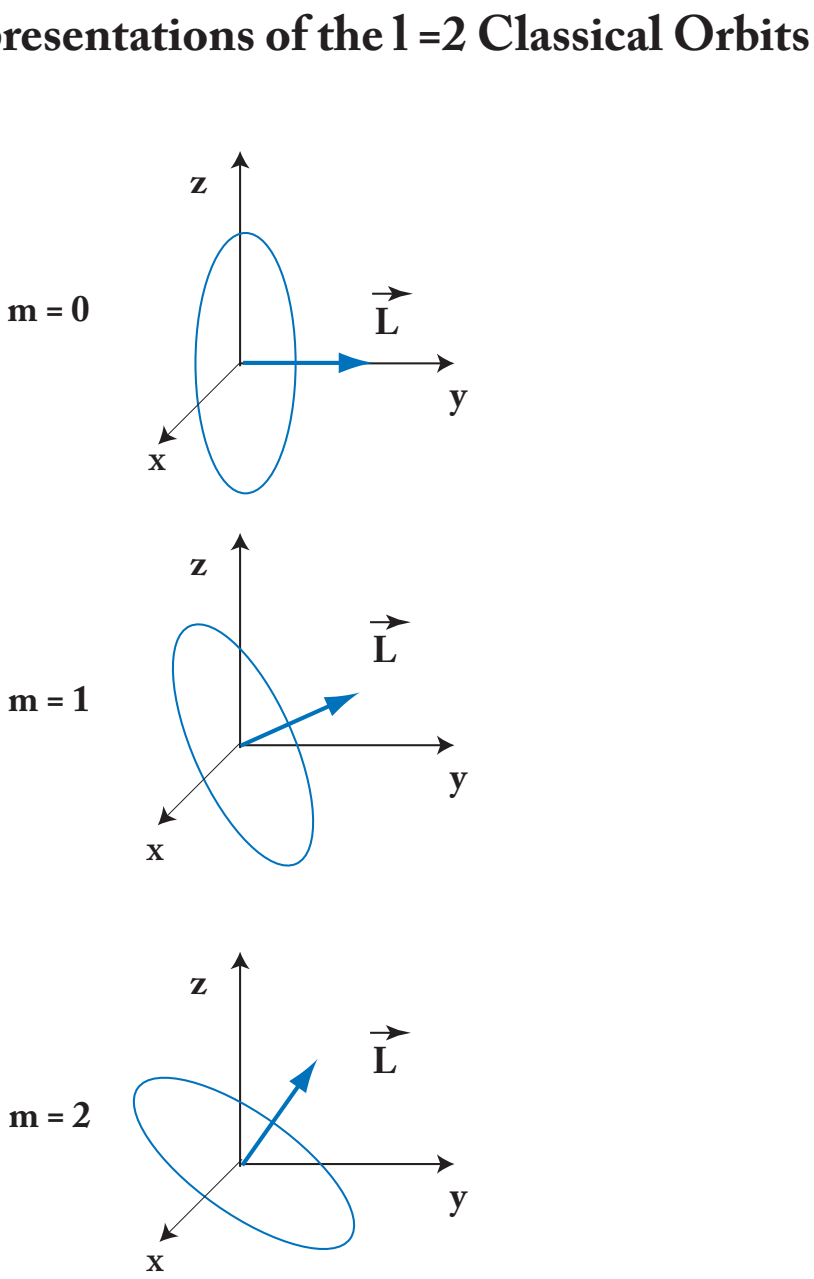

Figure 6.4: Classically, since the $m = 0$ orbit has a larger projection onto the z-axis than higher m-valued orbits, it is expected that the p_z momentum distribution of the $m = 0$ angular momentum state will be broader than other m-values' momentum distributions.

Figure 6.3 shows the recovered momentum distributions using IMR. These results indicate that the $m = 0$ distribution is narrower and taller than the $m = \pm 1$ distribution, and neither one shows any significant structure. The difference in the momentum distribution's relative width indicates a classical picture which is understood in terms of the classical electron's orbital alignment with the z-axis. As illustrated in Fig. 6.4, the m-value is a measure of the orbital angular momentum's projection onto the z-axis [19]. For the $m = 0$ configuration, the orbital plane of the electron is directly along the z-axis, and therefore, there is significant probability to measure the electron with large p_z-momentum. The $m = 0$ case is contrasted with the $|m| = 1$ configuration where the orbital plane has a smaller projection onto the z-axis, and consequently the electron has a narrower p_z-momentum distribution.

For this experiment, where the quantum and classical momentum distributions are very different, a classical result is surprising. To verify this result the differences in the momentum distributions' widths are measured directly in a second experiment. In this second measurement, the same basic experimental apparatus is used, but the half-waveplate is replaced with a Pockels cell. The voltage applied to the Pockels cell is set to rotate linearly polarized light by $\pi/2$. Voltage is applied to the Pockels cell with a field pulse box, where the trigger is a control sequence generated by a logical AND gate that takes inputs from a standard trigger pulse at a $15Hz$ rep rate, and a divide-by-N clock followed by a "flip-flop biting its tail" [87]. This second pulse is on for $25s$, then off for $25s$, at a $0.04Hz$ rep rate. The resulting pulse sequence facilitates measurements where, when the voltage is applied to the Pockels cell, the light's polarization is rotated for a number of laser shots, followed by an equal number of laser shots where the voltage is not applied, and the light's polarization is not rotated. Recording HCP ionization data while periodically switching the second dye laser's polarization at $f_0 = 0.04Hz$ provides a direct measurement of the ionization differences, $I(A)_{m=0} - I(A)_{|m|=1}$. Since the ionization differences are related to the derivative

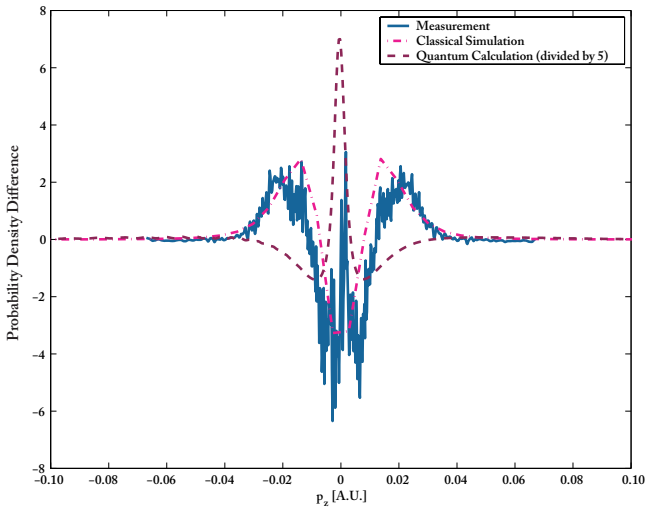

Figure 6.5: Momentum distribution differences $D(p_z)_{m=0} - D(p_z)_{|m|=1}$ inferred from a measurement of the ionization differences, $I_{m=0} - I_{|m|=1}$. This direct measurement of the ionization differences verifies the findings of the measurements shown in Fig. 6.3. Classical and quantum calculations are shown for $l = 2$ angular momentum states.

differences $dI/dA_{m=0} - dI/dA_{|m|=1}$, a numerical derivative of the ionization data is taken, and the experimental data is scaled into momentum coordinates through the same procedure that is used for standard HCP ionization data. The results of this second experiment, shown in Fig. 6.5, verify that the measured momentum distribution, when $m = 0$ states are excited, is broader than the $m = \pm 1$ state's distribution.

Since we appear to be measuring an effect that is, in a sense opposite to our quantum mechanical intuition, a question that one might ask is if it is possible that, due to birefringence in the vacuum window under strain [34] as the laser light enters the chamber, the light's polarization is rotated. To check this is not the case, a Glan-Thompson polarizer was placed inside the vacuum chamber where the IMR measurements are performed, and it was verified that the polarization of the light is not rotated by birefringence in the vacuum window.

While it is clear that the angular momentum eigenstates' p_z-momentum distributions are very different from their classical analogs, a wave-packet consisting of various angular momentum states actually does represent the measurement well. Results of a calculation

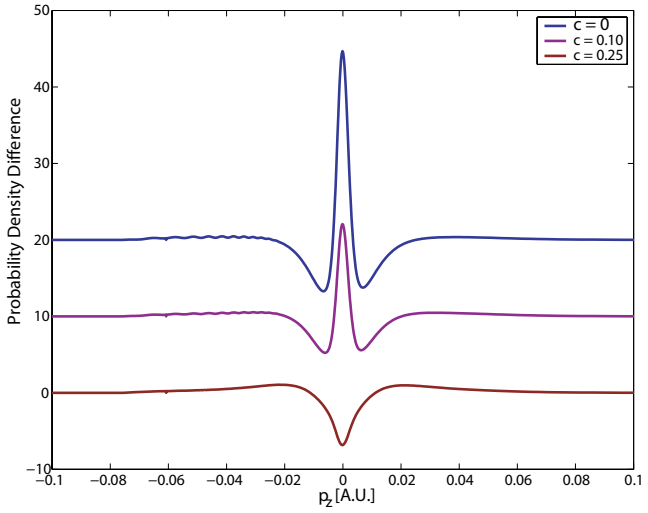

Figure 6.6: Calculated quantum mechanical momentum distribution differences $D(p_z)_{m=0} - D(p_z)_{|m|=1}$, of wave-packets defined by Eq. 6.1. Curves, shown offset for visual clarity, vary in this model as a function of k, the mixing parameter for $l = 1$ and 3 angular momentum states in the wave-packets.

where a wave-packet is modeled as a coherent mixture of angular momentum states are shown in Fig. 6.6. In the model, the wave-packet is given by a sum of angular momentum eigenfunctions [86]:

$$\Upsilon(p, \Theta, \Phi) = P_{n,l}(p)[(1 - 2c)Y_{l=2,m}(\Theta, \Phi) + cY_{l=1,m}(\Theta, \Phi) + cY_{l=3,m}(\Theta, \Phi)], \tag{6.1}$$

where the mixing coefficient, c is dependent on the HCP field strength. While a full solution of the quantum mechanical problem is beyond the scope of this thesis, a bound-state calculation was used to estimate c. In the bound-state quantum mechanical calculation, the Hamiltonian includes a $0.8ps$ wide gaussian electric field pulse to mimic the HCP. The calculation finds that the mixing coefficient, c, is approximately 0.25 for a HCP pre-pulse of $\sim 0.0030A.U.$ of impulse. This size of pre-pulse is about 10% as large as the kick strength required to ionize 50% of the electrons. The bound state calculation also indicates that for the same size of HCP field, the probability for driving transitions where $|\Delta l| > 1$ is less than 5%. Changes of m-value are forbidden by selection rules [88]. In addition to being consistent with the

data in Fig. 6.6, a pre-pulse of this size is consistent with independent measurements of the HCP field strength [56]. At the same time, this field is small enough that ionization is not expected to result from the pre-pulse alone, and therefore there is no inconsistency with the ionization measurements in Fig. 4.6 and 4.7 of Ch. 4. Had the pre-pulse been large enough to cause ionization on its own, these measurements, using a transient attenuator, would have indicated it. It may seem surprising that such a small HCP field can significantly affect the angular momentum eigenstates. However, since the angular momentum eigenstates do not have dipole moments, transitions where $\Delta l = \pm 1$ are strongly driven [89]. On the same note, the Stark eigenstate measurements in Ch. 5, have significant dipole moments, and subsequently transitions between Stark manifold states are difficult to drive with the HCP.

Efforts to eliminate any HCP pre-pulse included attempts to eliminate pre-pulses in the ultrafast laser system. Though it was found that improvements to the ultrafast laser system could be made, it was difficult to eliminate all pre-pulses. Additionally, we attempted to use a $1mm$ non-linear crystal for Second Harmonic Generation (SHG) of short-pulse laser light, where the concept was that the small SHG pre-pulses would have insufficient intensity to effectively produce a HCP pre-pulse. Since SHG is second-order in the intensity [34], we expected this might effectively eliminate the small laser pre-pulse. Unfortunately, with the amount of short-pulse SHG laser light available, the HCP radiation that was generated was insufficient to perform ionization experiments.

In summary, pre-pulses in ultrafast laser systems may be present, and must be considered when performing experiments that are sensitive to small amounts of HCP radiation. In principle, the IMR technique is still valid in this experiment, with the caveat that the HCP ionized a HCP-populated wave-packet, rather than an angular momentum eigenstate.

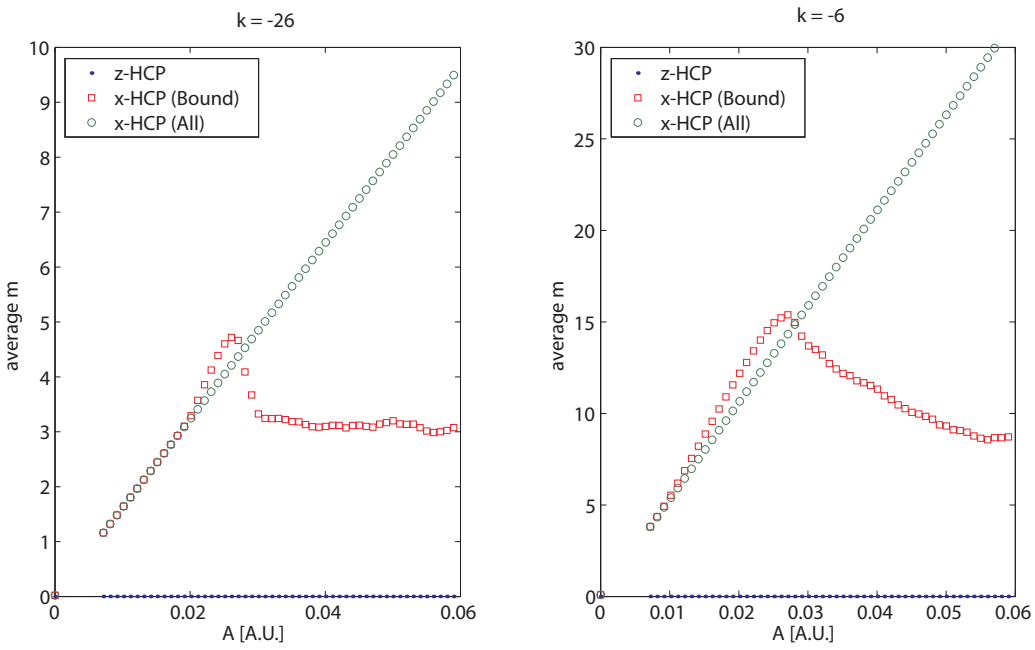

Figure 6.7: Average m-values are shown for both states studied. Electrons kicked by an HCP perpendicular to the static field axis readily change m-value. Though higher m-values facilitate higher ionization thresholds, the m-values for bound states are constrained by L_{Max}, given by Eq. A.12 of Appendix A. Electrons kicked by an HCP parallel or anti-parallel to the static field axis do not change m.

6.3 Stark State Measurements using a HCP perpendicular to the static field

This section describes studies of Stark eigenstates probed with a HCP, where the field axis is perpendicular to the static field axis. These measurements are similar to the measurements of Stark eigenstates conducted in Ch. 5, with a HCP parallel or antiparallel to the static-electric field axis. In fact, with the GaAs wafer mounted on a rotational stage, the exact same apparatus is used in the experiments presented here as in the measurements of the p_z-distributions.

It is expected from calculations (see Figs 5.7 and 5.8 of Ch. 5) that the p_x-distributions would have significantly different structures than the p_z-distributions. A further motivation

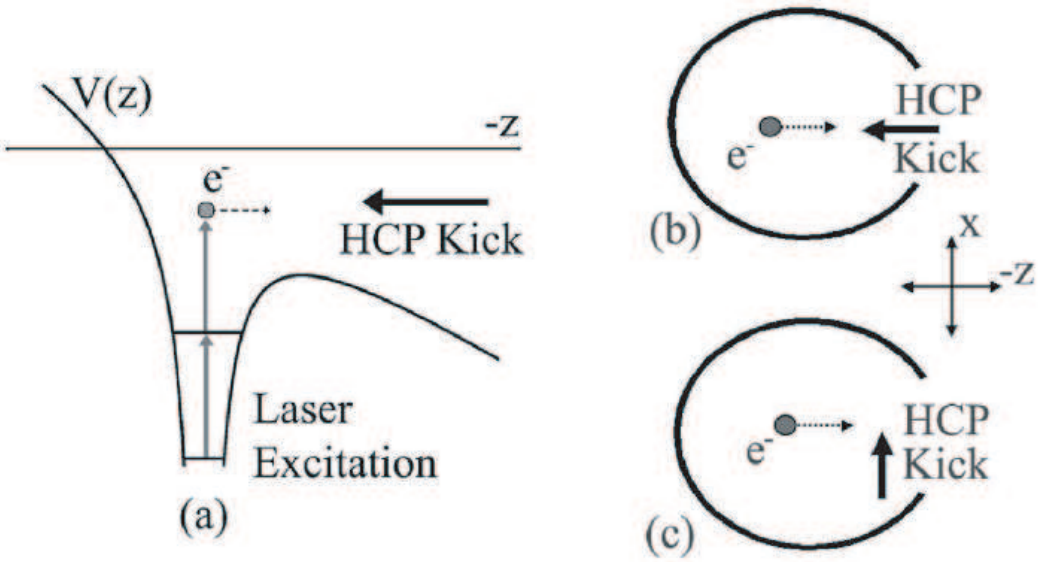

Figure 6.8: (a) is a schematic "side view" of the laser excitation and HCP ionization in the presence of a static-electric field. In (a), the "antiparallel" configuration of HCP and static fields is shown. (b) shows a "top view" of the Coulomb and Stark potentials for the for the "antiparallel" field orientation. The solid line represents a potential barrier that prevents the electron from exiting the system. The electron's motion is towards the hole in the potential. (c) shows the orthogonal field configuration [90].

for probing the atomic systems at different angles between the HCP and static field axis was an attempt to use IMR, through the techniques of computed tomography (CT), to construct a multidimensional image of the probability distribution. However, it was found that since the HCP probes the system over a finite time interval, the HCP kick in the perpendicular direction torques the electrons into a high-m state (see Fig. 6.7). The effects of this change in m-value are observed in the HCP ionization curves as shifts of the 50% ionization level to larger impulses. Previous measurements by Zeibel *et al.* [90] show that electron-ion recombination in a static-electric field is facilitated by HCP kicks orthogonal to the static field axis, through a dynamic stabilization process, illustrated in Fig. 6.8.

As already mentioned, the basic experimental apparatus is described in Ch. 5, with the only difference being the angle between the HCP field axis and the static-electric field axis. When the HCP field axis is parallel(antiparallel) to the static field axis, $+z(-z)$ ionization curves are measured. When the HCP field axis is perpendicular to the static field axis, x-ionization curves are measured. The x-ionization measurements are taken on the same days as much of the z-ionization data, to ensure regularity between the two types of data. The x-HCP fields are calibrated with the standard techniques.

The ionization curves shown in Figs. 6.9 and 6.10 are experimental results and classical simulations for comparison. A fully quantum mechanical calculation for a Hamiltonian with both an HCP and static-electric field is beyond the scope of this dissertation. However, classical simulations are practicable [31], and are performed here by launching an $l = 0$ electron into a static-electric field at a small radius $r(t = 0) = 100 A.U.$ The choice of $r(t = 0)$ does not affect the calculation so long as it is not chosen too small, specifically too close to $r = 0$ of the Coulomb potential, such that numerical errors propagate through-out the calculation. The initial energy of the electron is chosen to be the same energy that is determined for the $n = 28$ Stark states. The launch angle, with respect to the z-axis, is

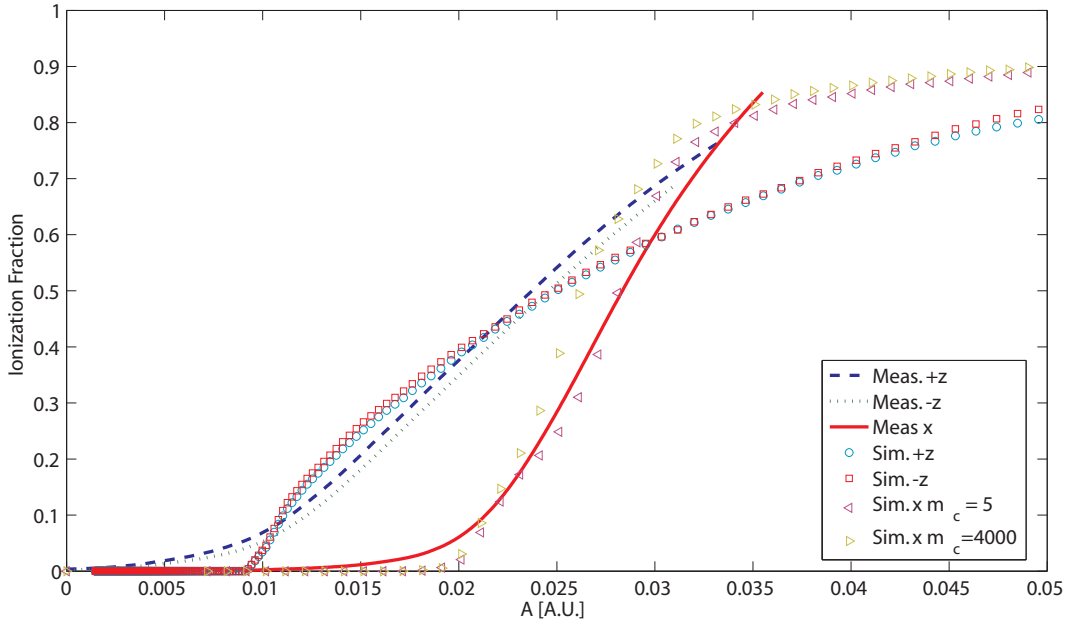

Figure 6.9: Measurements and results from classical simulations for the $n = 28, k = -26$ Stark eigenstate are shown for HCPs parallel $(+z)$, antiparallel $(-z)$ and perpendicular (x) to the static field axis. Two cases of m_c are shown to demonstrate the effects of HCP-induced stabilization in the ionization curves.

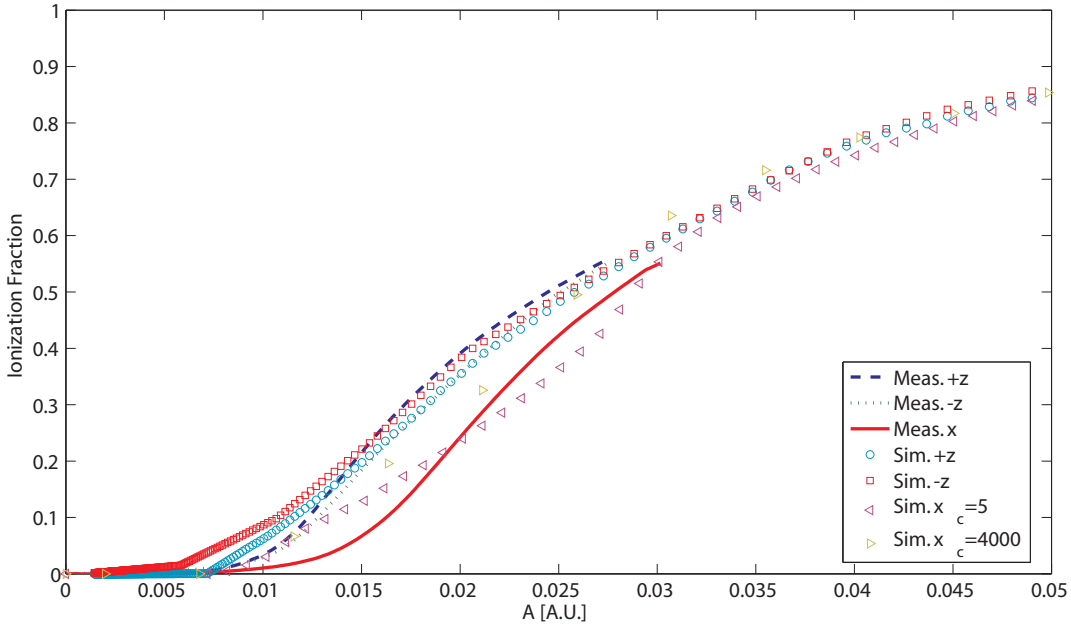

Figure 6.10: Measurements and results from classical simulations for the $n = 28, k = -6$ Stark eigenstate are shown for HCPs parallel $(+z)$, antiparallel $(-z)$ and perpendicular (x) to the static field axis. Two cases of m_c are shown to demonstrate the effects of HCP-induced stabilization in the ionization curves.

chosen so that the calculated dipole moment of the electron equals the dipole moment of the corresponding quantum mechanical Stark eigenstate. The Hamiltonian, including a $0.5ps$ FWHM gaussian to simulate the HCP and a $104V/cm$ static-electric field, is integrated over one Stark period. Throughout the integration, energy is numerically conserved to better than 5%. The probing time, the time-step where the HCP is maximum, is determined randomly, for a total of 5000 points. After the HCP probe has been applied, the electron's energy is calculated, and if it is larger than the critical energy, E_c, the electron is considered to be ionized. The critical energy is in general,

$$E_c = \frac{-F_s\eta_c}{2} - \frac{2Z_2}{\eta_c} + \frac{m^2-1}{2\eta_c^2}, \tag{6.2}$$

where η_c is the parabolic coordinate ($\eta = r - z$) [20] of the saddle point of the combined Coulomb/Stark potential. Z_2 in Eqn. 6.2 is called the separation constant. For large $|m|$-values the electron is excluded from the small radius part of the binding potential, and is subsequently referred to as hydrogenic. Here, Z_2 is dependent on the orientation of the electron's orbit with respect to the z-axis, and m [20]. A critical value of m_c is chosen, above which $Z_2(m)$ is calculated as,

$$Z_2(m) = \frac{1}{2}(1 - \langle A_z \rangle). \tag{6.3}$$

The physical significance of m_c is that it represents the value of $|m|$ above which the small r-portion of the potential is negligible. Z_2 may also be approximated in the case where $|m|$ is small. In this case, $\langle A_z \rangle$ is not conserved due to effects from the non-Coulombic part of the binding potential. For a given $|m| < m_c$ all classical electron trajectories ionize at the same critical energy, and where n_2 is the parabolic quantum number:

$$Z_2(m) = \frac{1}{n}(n_2 + \frac{|m|+1}{2}). \tag{6.4}$$

Simulation results, shown in Fig. 6.11, are run for $m_c = 1, 4, 5, 6, 10$ and 4000, where $m_c = 5$ provides the closest match to the data, but $m_c = 4$ and 6 are practically indistinguishable

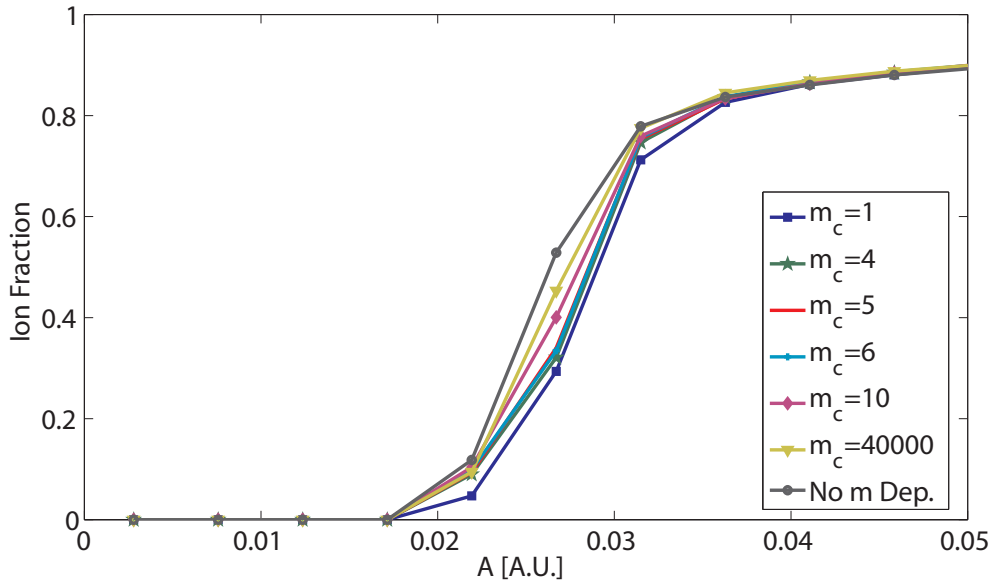

Figure 6.11: For the $k = -27$ state ionization curves are calculated at several values of m_c. The critical m-value determines above which values of m the potential may be considered hydrogenic.

from $m_c = 5$. Previous studies by Zeibel found a similar value of m_c. It was also verified that the ionization curve for the downhill state ($\langle A_z \rangle = -1$), when $m_c = 4000$, is converging to the case where the binding potential is independent of m.

It is found that while the HCP is interacting with the electronic states there is a significant change in the state's m-value. In principle, using the impulse approximation, HCP ionization is insensitive to the form of the potential, however, in the situation here, where the mean m-value changes significantly during the HCP/electron interaction, the impulse approximation breaks down. The asymmetry in the ionization curve results from the 50% ionization level shifting to larger values of the HCP kick strength - a stabilization effect. Previously, this HCP effect was utilized to recombine electrons with their parent ions through a dynamic stabilization of high m-value states that are populated during the HCP [90]. The stabilization, which is shown schematically in Fig. 6.8, is caused by the establishment of a centrifugal barrier at small r, that prevents the electron from sampling the non-hydrogenic

part of the binding potential [90].

When IMR is applied to transform the asymmetric ionization curves shown in Figs. 6.9 and 6.10, the approximate distributions are also asymmetric. Although there is reasonable agreement between classical calculations and experimental measurements, it is clear that the distributions recovered by applying IMR are not good approximations to the Stark eigenstate p_x-distributions. Thus, Stark state p_x-distributions are not presented in this thesis, since such an interpretation of the data would be flawed.

In fact, IMR may be applied to the data presented here, but one must interpret these distributions as the approximate momentum distributions of a HCP-induced wave-packet rather than the momentum distribution of a Stark eigenstate. Previously, the experiments of Campbell *et al.* [101] studied Stark wave-packets ionized by an HCP with an applied field perpendicular to the static electric field axis and observed changes in the wave-packet's p_x-distribution as a function of time. The recovered p_x-distributions showed a breathing of the wave-packet at the Stark period, which was the expected result. However, this experiment was primarily concerned with monitoring the Stark wave-packet as a function of time, not necessarily with the precise form of the wavefunction. Beside the experimental goals, there are other difference between the experiment presented in this section and those of Campbell *et al.*, for example they worked at higher energy levels where the HCP is expected to act more impulsively. As well, Campbell *et al.* calculated numerical derivatives from ionization curves. They accomplished this by spline-fitting the data [75], a process that can potentially introduce inaccuracies or smooth over small scale features. However, we mention the results of Campbell *et al.* because they demonstrate a useful application of the IMR process: Monitoring changes in a wave-packet as function of time. While the experiments presented in this section point out a difficulty in the measurement process, if the goal is to monitor changes as a function of time with the HCP, experiments by Campbell *et al.* demonstrate

that such an experiment is still possible.

6.4 Discussion

Presented here and in Ch. 5, are three experiments through which the validity of the impulse approximation is investigated. In all three experiments non-impulsive interactions with the HCP modify the atomic states prior to ionization. Though it is clear that this explains why the momentum distributions of the eigenstates were not successfully recovered with high accuracy in two cases, an obvious question raised is: *Under what circumstances can we expect the impulse approximation to be valid?*

In an attempt to answer this question, we begin by referring to the theoretical work of Robicheaux [78], where it was demonstrated by fully quantum mechanical calculations that in principle, $l = 2$ angular momentum eigenstates can be measured with IMR. The experimental results shown in Sec. 6.2 are reasonably-well explained in the context that a HCP pre-pulse changes the eigenstate, populating a wave-packet, that is subsequently probed with IMR. Therefore, we do not believe our experimental results contradict the predictions of Robicheaux. Rather, this measurement delineates a case where the HCP interacts with the atomic state over a very long time, before ionization occurs.

The measurements of Stark eigenstates HCP-kicked in the x-direction, together with the measurements of Stark eigenstates HCP-kicked in the z-direction certainly raise the question presented here, where the question becomes even more specific: *Why can we expect that the impulse approximation is valid for kicks along the z- but not the x-axis?* The pulse duration is the same along each axis, so the simple answer that the pulse is not fast enough is insufficient. The classical simulations presented in Sec. 6.3 show that this is another situation where information about the HCP interaction with the states is important to the ionization distribution.

Another way to state the impulse approximation in an ionization experiment is that little information about the final state distribution measured [78]. In experiments where Stark eigenstates are kicked in the x-direction, the possibility of dynamic stabilization indicates that the final state distribution is important, invalidating the impulse-approximation for this experiment. Kicked along the z-axis, selection rules protect the state from m-changing transitions. Selection rules here reflect the underling symmetry of the potential, so another way to state the last sentence is that when the HCP is parallel to the static field axis, the symmetry of the potential is not broken by the HCP/Stark state interaction. In this case, the impulse approximation evidently allows for momentum distribution measurements that are reasonable representations of the Stark eigenstates.

6.5 Conclusions

In this chapter, two experimental studies of HCP ionization are presented. In conjunction with the experiment presented in Ch. 5, these two studies are discussed in the context of the validity of the impulse approximation when applying IMR. In summary, all experiments showed significant non-impulsive effects of the HCP, and in cases where the HCP could drive transitions to bound states that are significantly different than the original state, the effects of these transitions are observed.

Chapter 7

Conclusions

Monitoring Rydberg electron wave-packets and eigenstates is a topic of great interest for several reasons: its relevance to the understanding of the dynamics and structure of electrons in external fields, verification of the principles of quantum control, and implementations of the notions of quantum information processing with atoms. The experiments presented in this thesis study highly excited alkaline earth atoms in a static-electric field, which form a practical system for investigating the complex dynamics and basic properties of electrons coupled to an external field. Two experimental techniques are used in the investigations. As discussed in Ch. 3, scaled energy recurrence spectroscopy (SERS) is used to reveal semi-classical dynamics in two-electron Stark atoms. Spatially sensitive detection for impulsive momentum retrieval (IMR) is used in the experiments presented in Ch. 5, where structure is measured in the momentum distribution of Stark eigenstates. In Ch. 6, a variety of HCP-probed electronic state measurements, as well as the applicability of the impulse approximation when performing these measurements, is discussed. Advancements to both scaled energy recurrence spectroscopy, and the impulsive momentum retrieval technique are demonstrated.

Scaled Energy Recurrence Spectroscopy

The development of techniques for the interpretation of the scaled energy recurrence spectra of alkaline earth atoms in a static electric field demonstrates the applicability of SERS to mixed-configuration Rydberg systems. Our results show that the general structure of the two-electron atom's recurrence spectra are very similar to those expected from a one-electron picture. This result verifies that we may apply SERS to these two-electron atoms, and indicates that the interaction with the static-electric field dominates the dynamics of the problem. Additionally, once the general structure of the scaled energy recurrence spectra are understood, the role played by two-electron dynamics is also evident in the spectra. Both Ca and Ba atoms are studied, and for the two different atomic species, two different doubly-excited signatures are found in their respective recurrence spectra. In Ba, when the electron returns to the ion-core after a Stark period, the electronic wave-packet develops doubly-excited character that interferes with the singly-excited character, causing structure in the recurrence spectra. Ba is an example of an atom where the configuration interaction is highly localized to states in a narrow region of the energy spectrum. Viewed with SERS, this narrow perturbing resonance corresponds to large time-scale structure. In Ca, the perturbing resonance is very broad, resulting in a short time-scale shift of individual recurrence peaks. A wave-packet picture must be employed here as well, but also the electronic wave-packet tends to act in a way that is well-described by a classical picture. Recurrence peaks in Ca are always shifted to longer times, since the electron is delayed after spending an extra amount of time near the ion-core: time associated with the configuration interaction. This delay in the electronic orbital period is too small to resolve over short times. However, over longer times, after the electron completes many orbits, the delay after every return accumulates, producing a large overall shift in the recurrence peaks at the Stark period. Although measurement of two different atomic species does not represent an exhaustive demonstration, the consistent

and coherent interpretation of both Ca and Ba demonstrates that SERS can be applied to observe a variety of doubly-excited effects. Our work, in conjunction with others in the field [41, 43], are advancing the techniques of SERS toward the development of a probe useful for understanding the dynamics of even more complicated systems, eg. atoms with several interacting configurations or even molecules. SERS is a particularly useful tool for the investigation of complicated systems because it provides interpretable pictures of the semi-classical dynamics. With the contributions presented in Ch. 3, SERS is now a proven experimental technique for revealing, from the Rydberg atom perspective, dynamical signatures of configuration interaction in atoms in a static-electric field.

Spatially sensitive detection for impulsive momentum retrieval

New techniques using the spatial profile of a beam of HCP radiation facilitate a precision measurement of Stark eigenstates, as discussed in Ch. 5. The specific advantage of the spatially sensitive detection method developed in this thesis, over previous implementations of IMR, is provided through the use of amplitude modulation techniques for the direct measurement of the derivative of the HCP ionization curves. Utilization of spatially sensitive detection capitalizes on amplitude modulation IMR techniques [74], aiding in a continuous derivative measurement, which was not previously possible.

With the direct experimental determination of the derivative signal, the primary limitation of the IMR process appears to be that the HCP is not a perfectly-impulsive probe of the Rydberg atoms where $n^* = 28$. The Kepler period of a Rydberg atom when $n^* = 28$ is about $3.4ps$, so it may seem surprising that a $0.5ps$ HCP is not a fast-enough probe for this system. However, calculations show that during a $0.5ps$ time window, electrons that have a large momentum, move significantly, and consequently the electronic momentum distributions are not accurately measured. This effect is indicated by the experiments where

z-momentum distributions of large-dipole moment Stark states are measured, and significant probability at large momenta is expected. Specifically, the break-down of the impulse approximation causes the measured distributions to be narrower and taller than expected for these Stark eigenstates. For the small-dipole moment state, where the p_z-momentum distribution does not have significant probability at large momenta, the measurements appear to be accurate representations of the Stark eigenstate momentum distributions. These measurements benchmark the IMR technique, demonstrating unprecedented accuracy and resolution.

Although the particular characteristics of Stark atoms are exploited in the measurements in this thesis, the experimental techniques, suitably extended, may be applied to a broader definition of atoms. As discussed in the previous paragraph, investigations using spatially sensitive detection for impulsive momentum retrieval were successful for approximating the Stark eigenstate momentum distributions projected onto the p_z-axis. However, application of the techniques is unsuccessful in a few other cases presented. Investigations of these other cases, and a thorough exploration of the applicability of the impulse approximation is presented in Ch. 6. This discussion shows that the accuracy of the approximate momentum distributions obtained through IMR is limited, because the HCP is not an infinitely short pulse. Of course, many previous experimental and theoretical studies have already explored IMR applied to other atomic systems [5, 8, 31, 67, 69, 74, 75, 77, 78, 79, 80, 81, 82, 85, 101], and the IMR technique is a proven effective probe for measuring approximate electronic-momentum distributions as a function of time. In particular the experiments by Jones [5] and Campbell *et al.* [67, 101] have proven that IMR is useful for monitoring Rydberg wavepacket dynamics, so the limitations discussed in Ch. 6 are not to say that the IMR technique is invalid. It is a question of the role that IMR plays in the experiment, in addition to the validity of the impulse approximation. Another example of recent work in probing

atomic systems is the previously mentioned work of Italani *et al.* [1], where a method for tomographic imaging of molecular orbitals is described. Undeniably, this is ground-breaking work. However, it is argued that in general, for many electron systems this tomographic probing method is inaccurate [92]. Still, despite the limitations, Italani *et al.*'s method is useful for monitoring temporal changes in electronic wavefunctions. Despite their inaccuracies, both the tomographic imaging method of Ref. [1] and impulsive momentum retrieval are useful probes for viewing electronic probability distributions. In the current field of atomic and molecular research, where there is significant interest in probing atomic systems, it is important to know the limitations of the experimental probes. In this thesis a highly-accurate impulsive momentum retrieval measurement is demonstrated. As well, limitations of the impulse approximation are explored.

Summary

Two experimentally useful probes of atomic systems are explored in this thesis. The utility of scaled energy recurrence spectroscopy is extended through new techniques for interpretation of the spectra. The new techniques exhibit the signatures of two-electron dynamics in an electronic wave-packet that is strongly driven in a static electric field. In other experiments, new techniques for the application of half-cycle pulse ionization are explored, and result in highly-resolved probability distribution measurements of Rydberg states in a static-electric field. In addition to the development of these two probing techniques, experiments presented in this thesis also contribute to the general understanding of electronic properties in the presence of a static-electric field.

Bibliography

[1] J. Itatani, J. Levesque, D. Zeidler, H. Niikura, H. Pépin, J. C. Kieffer, P. B. Corkum, and D. M. Villeneuve, Nature **432**, 867-871 (2004).

[2] H. Niikura, F. Légaré, R. Hasbani, M. Y. Ivanov, D. M. Villeneuve, and P. B. Corkum, Nature **421**, 826-829 (2003).

[3] R. Kienberger, E. Goulielmakis, M. Uiberacker, A. Baltuska, V. Yakovlev, F. Bammer, A. Scrinzi, Th. Westerwalbesloh, U. Kleineberg, U. Heinzmann, M. Drescher, and F. Krausz, Nature **427**, 817-821 (2004).

[4] A. Föhlisch, P. Feulner, F. Hennies, A. Fink, D. Menzel, D. Sanchez-Portal, P. M. Echenique and W. Wurth, Nature **436**, 373-376 (2005).

[5] R. R. Jones, Phys. Rev. Lett. **76**, 21 (1996).

[6] R. R. Jones, D. You, and P. H. Bucksbaum, Phys. Rev. Lett. **70**, 1236 (1993).

[7] M. Shapiro and P. Brumer, *Principles of the Quantum Control of Molecular Processes* (Wiley, Toronto 2003).

[8] H. Maeda, D. V. L. Norum, and T. F. Gallagher, Science 307, 1757 (2005).

[9] R. S. Minns, M. R. Kutteruf, H. Zaidi, L. Ko, and R. R. Jones, Phys. Rev. Lett. **97**, 040504 (2006).

[10] G. K. Brennen, C. M. Caves, P. S. Jessen, and I. H. Deutsch, Phys. Rev. Lett. **82**, 10601063 (1999).

[11] J. Ahn, T. C. Weinacht, and P. H. Bucksbaum, Science **287**, 463 (2000).

[12] M. W. Noel and C. R. Stroud Jr. Optics and Photonics News, April (1999).

[13] C. R. Stroud Jr. Science **303** 5659 pp.778-779 (2004).

[14] S. N. Pisharody, Science **303** 5659 pp.813-815 (2004).

[15] X. Wang and W. E. Cooke, Phys. Rev. A. **46**, R2201 (1992).

[16] T. F. Gallagher *Rydberg Atoms* (Cambridge Univeristy Press, Cambridge, 1994).

[17] U. Eichmann, K. Richter, D. Witgen, and W. Sandner, Phys. Rev. Lett. **61**, 2438 (1988).

[18] J. Murray-Krezan, J. Kelly, M. R. Kutteruf,and R. R. Jones, Phys. Rev. A, (accepted 2006).

[19] S. Gasiorowicz, *Quantum Physics* (John Wiley and Sons Inc., New York 2003).

[20] H. A. Bethe and E. E. Salpeter, *Quantum Mechanics of One- and Two-Electron Atoms* (Plenum, New York, 1977).

[21] R. R. Jones and L. D. Noordam, *Advances in Atomic, Molecular, and Optical Physics* **38**, 1 (1997).

[22] S. N. Pisharody, J. G. Zeibel,and R. R. Jones, Phys. Rev. A, **61**, 063405 (2000).

[23] M. B. Campbell, T. J. Bensky, and R. R. Jones, Opt. Express **1**, 197 (1997).

[24] Kimball Physics Inc. Phosphor Screen Data Sheets.

[25] Eljen Technology, EJ-440 Phosphor Data Sheets, http://www.apace-science.com/eljen/ej-440.htm.

[26] Spectra-Physics Inc. Millennia Vs User's Manual (2001).

[27] T. W. Hansch, Applied Optics **11**, 4 (1972).

[28] M. G. Littman, Opt. Lett. **3**, 138 (1978).

[29] Flammable liquids, especially non-polar ones, may develop static charges when moving. Although there is no mention of this particular problem on the Sigma-Aldrich 1-4 Dioxane Material Safety data sheet, multiple sources (Prof. Bob Jones, Sirah Laser Corp., Spectra-Physics) report that this problem is acute in P-Dioxane.

[30] S. N. Pisharody, PhD. Thesis, University of Virginia, (2003).

[31] J. G. Zeibel, PhD. Thesis, University of Virginia, (2003).

[32] Kapteyn-Murnane Laboratories Inc. Model MTS Mini Ti:Sapphire Laser Kit Instruction Manual (2003).

[33] W. T. Silvfast, *Laser Fundamentals* (Cambridge University Press, Cambridge, England, 1996).

[34] E. Hecht, *Optics* (Addison Wesley, San Francisco 2002).

[35] J. Gao and J. B. Delos, Phys. Rev. A **49**, 869 (1994); A. D. Peters, C. Jaffe, and J. B. Delos, Phys. Rev. Lett. **73**, 2825 (1994).

[36] P. A. Dando, T. S. Monteiro, and S. M. Owen, Phys. Rev. Lett. **80**, 2797 (1998).

[37] F. Robicheaux and J. A. Shaw, Phys. Rev. A **58**, 1043 (1998); J. A. Shaw and F. Robicheaux, Phys. Rev. A **58**, 1910 (1998).

[38] B. E. Granger and C. H. Greene, Phys. Rev. A **62**, 012511 (2000).

[39] M. Courtney, N. Spellmeyer, H. Jaio, and D. Kleppner, Phys. Rev. A **51**, 3604 (1995); M. Courtney, H. Jiao, N. Spellmeyer, and D. Kleppner, Phys. Rev. Lett. **73**, 1340 (1994); M. Courtney, H. Jiao, N. Spellmeyer, D. Kleppner, J. Gao, and J. B. Delos, *ibid.* **74**, 1538 (1994).

[40] A. Kips, W. Vassen, and W. Hogervorst, Phys. Rev. A **59**, 2948 (1999); G. J. Kuik, A. Kips, W. Vassen, and W. Hogervorst, J. Phys. B **29**, 2159 (1996); A. Kips, W. Vassen, W. Hogervorst, and P. A. Dando, Phys. Rev. A **58**, 3043 (1998).

[41] K. A. Bates, J. Masae, C. Vasilescu, and D. Schumacher, Phys. Rev. A **64**, 033409 (2001).

[42] M. L. Keeler and T. J. Morgan, Phys. Rev. Lett. **80**, 5726 (1998); Phys. Rev. A **59**, 4559 (1999).

[43] M. L. Keeler, H. Flores-Rueda, J. D. Wright, and T. J. Morgan, J. Phys. B **37**, 809 (2004).

[44] R. V. Jensen, H. Flores-Rueda, J. D. Wright, M. L. Keeler, and T. J. Morgan, Phys. Rev. A **62**, 053410 (2000).

[45] X. J. Liu, J. W. Cao, M. S. Zhan, and J-P. Connerade, J. Phys. B **34**, 1175 (2001); M. S. Zhan, X. J. Liu J. W. Cao and J-P Connerade, J. Phys. B **35**, 2069 (2002).

[46] J. A. Armstrong, P. Esherick,and J. J. Wynne, Phys. Rev. A **57**, 3712 (1998).

[47] M. Born *The Mechanics of the Atom* (Frederick Ungar Publishing Co., New York, 1960).

[48] T. R. Gentile, B. J. Hughey, D. Kleppner, and T. W. Ducas, Phys. Rev. A **42**, 440 (1990).

[49] M. L. Zimmerman, M. G. Littman, M. M. Kash, and D. Kleppner, Phys. Rev. A **20**, 2251 (1979).

[50] B. Lyons, D. W. Schumacher, D. I. Duncan, R. R. Jones and T. F. Gallagher, Phys. Rev. A **57**, 3712 (1998).

[51] M. Aymar, and O. Robaux, J. Phys. B **12**, 531 (1979).

[52] F. Robicheaux, C. Wesdrop and L. D. Noordam, Phys. Rev. A **60**, 1420 (1999); W. Sandner, K. A. Safinya, and T. F. Gallagher, Phys. Rev. A **33**, 1008 (1986).

[53] B. H. Post, W. Vassen, W. Hogervorst, M. Aymar, and O. Robaux, J. Phys. B **18**, 187 (1985);W. Vassen, T. v. d. Veldt, C. Westra, E. Bente, and W. Hogervorst, J. Phys. B **6**, 1473 (1989).

[54] W. A. Henle, H. Ritsch, and P. Zoller, Phys. Rev. A **36**, 683 (1987).

[55] N. E. Tielking, T. J. Bensky, and R. R. Jones, Phys. Rev. A **51**, 3370 (1995).

[56] L. Ko, personal communication.

[57] E. Budiarto, N.W. Pu, S. Jeong, and J. Bokor, Opt. Lett. **23** 3 (1998).

[58] B. Fischer, M. Hoffmann, H. Helm, G. Modjesch, and P. Uhd Jepsen, Semicond. Sci. Technol. **20** 7 (2005).

[59] A. Gürtler, C. Winnewisser, H. Helm, and P. U. Jepsen, J. Opt. Soc. Am. A **17** 1 (2000).

[60] T.I. Jeon and D. Grischowsky, Appl. Phys. Lett. **88**, 061113 (2006).

[61] T.I. Jeon, J. Zhang, and D. Grischowsky, Appl. Phys. Lett. **86**, 161904 (2005).

[62] A. Wetzels, A. Gürtler, A. Buijserd, T. Vijftigschild, H. ter Horst, and W. J. van der Zande, Rev. of Sci. Inst. **74** 6 (2003).

[63] G. L. Carr, M. C. Martin, W. R. McKinney, G. R. Neil, K. Jordan, and G. P. Williams, Nature **420** 153 (2002).

[64] R. Köhler, A. Tredicucci, F. Beltram, H. E. Beere, E. H. Linfield, A. G. Davies, D. A. Ritchie, R. C. Iotti, and F. Rossi, Nature **417** 156159 (2002).

[65] B. Ferguson and X. C. Zhang, Nature Materials **1** 26-33 (2002).

[66] D. You, R. R. Jones, D. R. Dykaar, and P. H. Bucksbaum, Opt. Lett. **18**, 290 (1993).

[67] M. B. Campbell, T. J. Bensky, and R. R. Jones, Phys. Rev. A **58**, 514 (1998).

[68] C. Raman, T. C. Weinacht, and P. H. Bucksbaum, Phys. Rev. A **55**, R3995 (1996).

[69] H. Maeda and T. F. Gallagher, Phys. Rev. Lett. **92**, 13004-1 (2004)

[70] J. Bromage and C. R. Stroud, Phys. Rev. Lett. **83**, 4963 (1999).

[71] P. H. Siegel, IEEE MTT **50** 3 (2002).

[72] E. Mueller, The Industrical Physicist **9** 4 (2003).

[73] O. Zobay and G. Alber, Phys. Rev. A **60** 1314 (1999).

[74] J. G. Zeibel and R. R. Jones, Phys. Rev. A **68**, 023410 (2003).

[75] M. B. Campbell, PhD Thesis, University of Virginia (2000).

[76] R. R. Jones, N. E. Tielking, D. You, C. Raman and P. H. Bucksbaum, Phys. Rev. A **51**, R2687 (1995).

[77] R. R. Jones and M. B. Campbell, Phys. Rev. A **61**, 013403 (2000).

[78] F. Robicheaux, Phys. Rev. A **56**, R3358 (1997).

[79] F. Robicheaux, Phys. Rev. A **60**, 431 (1999).

[80] C. Manescu, J. L. Krause, and K. J. Schafer, Phys. Rev. A **68**, 013405 (2003).

[81] A. Bugacov, B. Piraux, M. Pont, R. Shakeshaft, Phys. Rev. A **51**, 4877 (1995).

[82] C. Rangan, K. J. Schafer, and A. R. P. Rau, Phys. Rev. A **61**, 053410 (2000).

[83] C. Kittel, *Introduction to Solid State Physics* (John Wiley and Sons Inc., New Jersey, 1996).

[84] A. Yariv, *Quantum Electronics* (John Wiley and Sons Inc., New Jersey, 1988).

[85] A. Wetzels, A. Gürtler, H. G. Muller, and L. D. Noordam, Eur. Phys. J. D **14**, 157-165 (2001).

[86] B. Podolsky and L. Pauling, Phys. Rev. **36**, 109 (1929).

[87] P. Horowitz and W. Hill, *The Art of Electronics*, Cambridge University Press, USA (1989).

[88] Selection rules can be found in many standard quantum mechanics texts. For example see Ref. [19].

[89] N. E. Tielking and R. R. Jones, Phys. Rev. A **52**, 1317 (1995).

[90] J. G. Zeibel and R. R. Jones, Phys. Rev. Lett. **89**, 093204 (2002).

[91] J. C. Diels and W. Rudolph, *Ultrashort Laser Pulse Phenomena* (Academic Press, 1996).

[92] R. Santra and A. Gordon, Phys. Rev. Lett. **96**, 073906 (2006).

[93] I. Samengo, Phys. Rev. A **58**, 2767 (1998)

[94] T. P. Hezel, C. E. Burkhardt, M. Ciocca, and J. J. Leventhal, Am. J. Phys. **60**, 324 (1991).

[95] T. Ehrenreich, J. C. Day, S. B. Hansen, E. Horsdal-Pedersen, K. B. MacAdam, and K. S. Mogensen, J. Phys. B: At. Mol. Opt. Phys. **27**, L383-389 (1994)

$$\beta_x = \frac{e m_e v_0}{n(1-e^2)^{1/2}} \tag{7.1}$$

$$R_p = \frac{m_e v_0}{n(1-e^2)^{1/2}.} \tag{7.2}$$

[96] J. C. Gay, D. Delande, and A. Brommier, Phys. Rev. A **39**, 6587 (1989).

[97] F. Penent, D. Delande, and J. C. Gay, Phys. Rev. A **37**, 4707 (1988).

[98] A. Hooker, C. H. Greene, W. Clark, Phys. Rev. A **55**, 4609 (1997).

[99] E. Rabani, R. D. Levine, A. Mühlpfordt, and U. Even, J. Chem. Phys. **102** 4 (1995).

[100] C. L. Stokely, F. B. Dunning, C. O. Reinhold, and A. K. Pattanayak, Phys. Rev. A **65**, 021405(R) (2002).

[101] M. B. Campbell, T. J. Bensky, and R. R. Jones, Phys. Rev. A **59**, R4117 (1999).

[102] B. Cordani, *The Kepler Problem* (Birkhäuser Verlag, 2003).

[103] H. C. Corben and P. Stehle *Classical Mechanics* (Dover, 1994).

[104] T. J. Bensky, PhD. Thesis, University of Virginia, (1998).

Appendix A

Classical orbits in a static-electric field

A.1 Introduction and Background

This Appendix discusses the classical orbits of an electron in a static electric field that correspond to quantum mechanical Stark eigenstates. The classical problem of an electron in a Stark field has been explored previously, since it is interesting in a variety of areas, (see Refs. [47, 94, 95, 96, 97, 98, 99, 100, 101, 102, 103, 35, 39, 79, 76, 90, 74]). Notably, a similar discussion, of oriented elliptical states formed in crossed E and B fields, is in the paper on electron-ion collisions by Ehrenreich *et al.* [95]. Still, to the best of our knowledge, the analysis presented here, where an expression is found for the maximum angular momentum of classical states corresponding to Stark eigenstates, has not been previously published, nor have the momentum-space forbidden regions discussed here been previously presented.

The equations describing the orbits in a field-free situation are discussed, to facilitate understanding the problem in a static electric field. A Rydberg electron's orbit in both spatial and momentum coordinates is well-described in terms of a few simple relations.

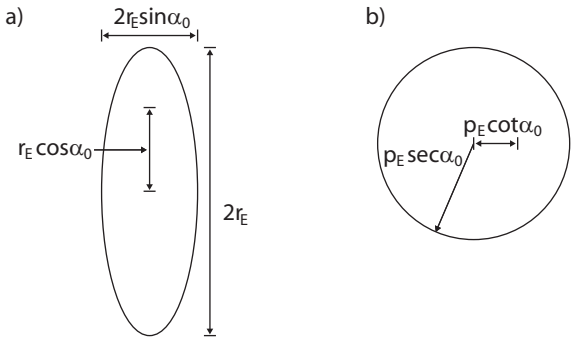

Figure A.1: a) Trajectory of an electron in coordinate space b) Trajectory of an electron in momentum space. In both cases the electron is bound in a Coulomb potential. α_0 is defined in the text in terms of the angular momentum and Runge-Lenz vector.

While this is well-known in spatial coordinates, the relations and picture (see Fig. A.1 b) in momentum space are less well-known. We begin with the energy, E, and follow the notation of Samengo [93]:

$$E = \frac{p_E^2}{2} = -\frac{1}{2r_E} = \frac{1}{2L_E^2}. \tag{A.1}$$

Given that $E = -1/2n^2$ in atomic units,

$$p_E = 1/n \tag{A.2}$$

$$r_E = n^2 \tag{A.3}$$

$$L_E = n. \tag{A.4}$$

Defining $\alpha_0 = arctan(L/L_E A)$, we express the angular momentum and Runge-Lenz vector as,

$$L = L_E sin\alpha_0 \tag{A.5}$$

and

$$A = cos\alpha_0. \tag{A.6}$$

Figure A.1 b) shows the momentum space trajectories in the field free situation: circles of radius $R_p = p_E sec\alpha_0$, offset from the origin by $p_E cot\alpha_0$.

In this appendix we determine the electron's classical trajectories in momentum space for the Stark problem. In a straightforward manner, the classical Hamiltonian is integrated, yielding the trajectories. However, interpretation of the computational results requires further exploration. A maximum value of the angular momentum is determined in the Stark problem that lends some physical insight into the computational results. Additionally, the equations of motion are solved directly, and through this result, the forbidden regions in momentum space are described.

A.2 Computational Methods

The Hamiltonian in the Stark problem, for an electron constrained to a plane parallel to the static-electric field axis is,

$$H = \frac{1}{2}(p_x^2 + p_z^2) - \frac{1}{\sqrt{x^2 + z^2}} - zF. \tag{A.7}$$

The set of differential equations:

$$\frac{dx}{dt} = p_x \tag{A.8}$$

$$\frac{dz}{dt} = p_z \tag{A.9}$$

$$\frac{dp_x}{dt} = -\frac{x}{r^3} \tag{A.10}$$

$$\frac{dp_z}{dt} = -\frac{z}{r^3} + F \tag{A.11}$$

follow, and are integrated with a Runge-Kutta algorithm. We use a C code based on Zeibel's [31], which in turn is based on Bensky's [104] code, and *Numerical Recipes*. We have also developed an alternative code in MatLAB using the *ode45* solver to perform the integration. For the specific values of E and F we are interested in simulating, the numerical accuracy required to obtain $< 5\%$ deviation in energy as a function of time appears to be at the limit of our algorithm's ability. For this highly accurate calculation, we find

that the C code is much faster than the equivalent MatLAB implementation. At any rate, given the four differential equations, Eqs. A.8-A.11, and a good Runge-Kutta algorithm, it is straightforward to calculate the trajectories.

There are four initial conditions to specify: $x(t = 0)$, $z(t = 0)$, $p_x(t = 0)$, and $p_z(t = 0)$. These four quantities are calculated from four other parameters, the energy, angular momentum, L, initial radius, $r(t = 0)$, and launch angle. In these classical calculations, an electron is launched onto a trajectory in a static-electric field of $\overrightarrow{F} = 1/3n^5\hat{z}$, and the launch angle is defined with respect to the z-axis. Although the calculation is not sensitive to the exact value of $r(t = 0)$, launching from the origin causes numerical errors, so the electron is launched from the position $r(t = 0) = \frac{1}{100}n^2$. The electron is launched with $L = 0$, and the initial velocity $v(t = 0)$ is solved for, given $r(t = 0)$ and E. The electron's launch angle with respect to the z-axis, is the primary factor determining the value of $\langle A_z \rangle$, or alternatively the electron's average dipole moment. Energy and the time-averaged z-projection of the Runge-Lenz vector are conserved, so we define the classical analog to a Stark eigenstate with principle quantum number n and parabolic quantum number k, as having the same energy and value of $\langle A_z \rangle = k/n$. It is notable that while different choices of fields and $r(t = 0)$ may result in slightly different dynamics, for example a different Stark period, the energy and $\langle A_z \rangle$ remain well defined.

Results from the classical calculations are shown in Figs. A.2-A.4 for a few different choices of launch angle. For the sake of coherence in this discussion, only calculations with launch angles that yield $\langle A_z \rangle < 0$ are shown. However, calculations over the full range of $\langle A_z \rangle$ have been computed, and the plots shown here are for just a few of the launch angles studied. In Figs. A.2-A.4 a) spatial-coordinate trajectories are displayed. These clearly show that the electron spends most of its time on one side of the z-axis, indicating a permanent dipole moment. Figures A.2-A.4 b) are the corresponding momentum space trajectories, and

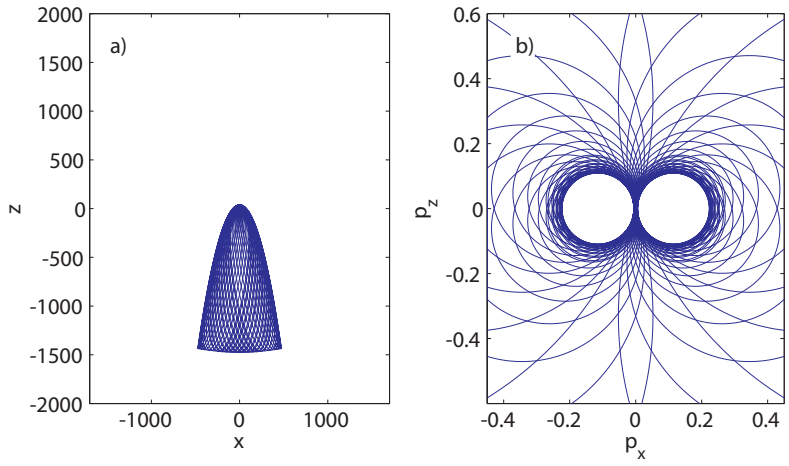

Figure A.2: $n = 28$, $\langle A_z \rangle$=-0.95, $L_{Max} = 8.8$, $R_p + \beta_x = 0.226$

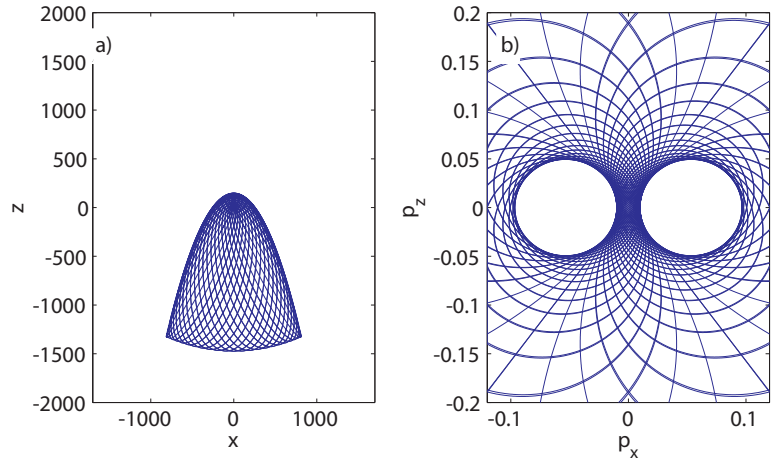

Figure A.3: $n = 28$, $\langle A_z \rangle$=-0.81, $L_{Max} = 16.5$, $R_p + \beta_x = 0.107$

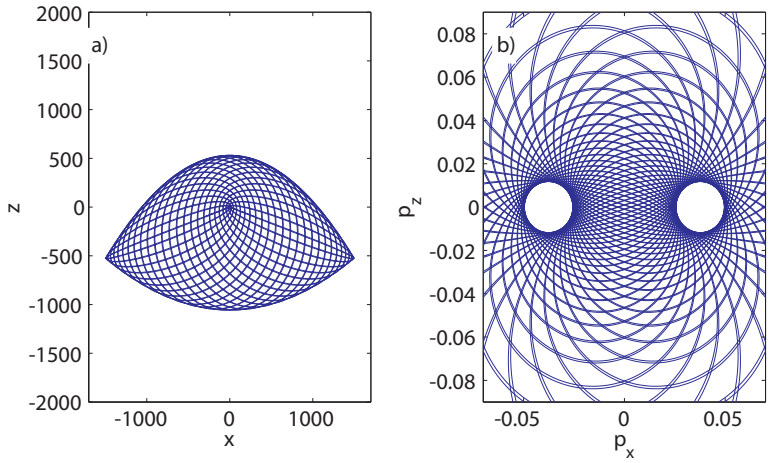

Figure A.4: $n = 28$, $\langle A_z \rangle$=-0.32, $L_{Max} = 26.8$, $R_p + \beta_x = 0.049$

they clearly show forbidden regions through which the electron does not pass.

A.3 Discussion

Since the calculations shown in Figs. A.4-A.3 are results of a classical computation, it is reasonable to expect that with some physical insight, we can understand this problem. Indeed, the classical Stark problem is detailed in several text books, for example Born's *Mechanics of the Atom* [47], Corben and Stehle's *Classical Mechanics* [103], and Cordani's *The Kepler Problem* [102]. Although the Stark problem is worked out in detail in these references, the momentum space representation is not addressed, and consequently, the forbidden regions are not discussed. The following sections attempt to show how the forbidden regions in momentum space come about through two different approaches. The first approach is a simple model, where it is indicated that, at least to some extent, the sizes of the forbidden regions are related to the electron's maximum angular momentum value, which in turn is a function of the electron's orbital orientation in the field. This aids in providing physical insight, but does not lead to a complete description of the forbidden regions. The second ap-

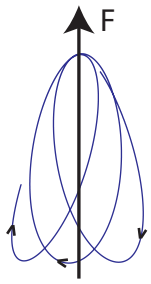

Figure A.5: Cartoon of an electron's elliptical orbit precessing about the static electric field axis.

proach is to use insight from perturbation theory, through Hamilton-Jacobi formalism. This approach is mathematical, but provides a reasonably complete picture of the constraints on the electron's motion.

A.3.1 The Simple Model: Consider precession of the electron's orbit

In this approach to the classical Stark problem we begin by examining the momentum space orbits in zero-field. In zero-field, the momentum space orbit is a circle with radius, $R_p = p_E L_E/L$ (see Fig. A.1 b). In the Stark problem, for the case of the so-called downhill state ($\langle A_z \rangle = -1$when $L \neq 0$), the picture is identical to the one in zero-field, Fig. A.1. When $\langle A_z \rangle \approx -1$, in a small static-electric field, the electron's orbital shape and position undergoes a slow variation, as the static-electric field perturbatively torques the electron's angular momentum [47, 94]. This picture is illustrated in Fig. A.5. An electron initially launched into the static electric field with $L = 0$ is torqued to a maximal value, L_{Max}, when the semi-major axis of the electron's orbit is aligned with the field axis, and $A = \langle A_z \rangle$ [94]. Illustrated in Fig. A.6, using Eqns. A.5 and A.6, when $L = L_{max}$, it is found that the electron's angular momentum is constrained by both the energy and the z-projection of the

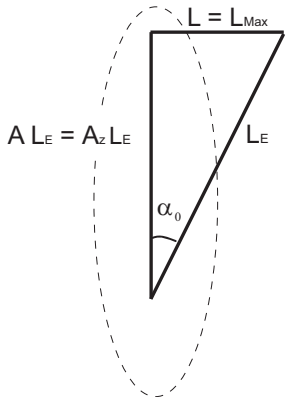

Figure A.6: Solid lines illustrate the geometrical relation between the Runge-Lenz vector and the angular momentum when $A = \langle A_z \rangle$ and L is maximized. The dashed line is an orbital path, where the semi-major axis of the electron's orbital ellipse is aligned with the z-axis. Since $L_E = n$, Eq. A.12 is derived from this picture.

Runge-Lenz vector:

$$L_{Max} = \sqrt{n^2 - n^2 \langle A_z \rangle^2}. \tag{A.12}$$

Equation A.12 is tested by numerical studies, shown in Figs. A.7 and A.8. These results do not demonstrate perfect agreement between the simulations and analytic results derived here. However, strictly speaking Eq. A.12 is only valid when the electric field is small, and the fields used in the calculations are sufficient to produce large Stark shifts. So we believe that the agreement between the calculations and the analytic results is reasonable considering the approximations made.

Returning to the discussion of the momentum space orbits, for Stark states, as the coordinate space orbital axis precesses in the field, the momentum space orbit also precesses, and changes shape. To the extent that we may consider the orbits as elliptical trajectories in position space, in momentum space the orbits are approximately circular ($R_p \approx p_E L_E / L$). This radius approximately describes the orbit at a given time and is minimized when $L = L_{Max}$. The center of a nearly-circular momentum space trajectory is offset from the origin

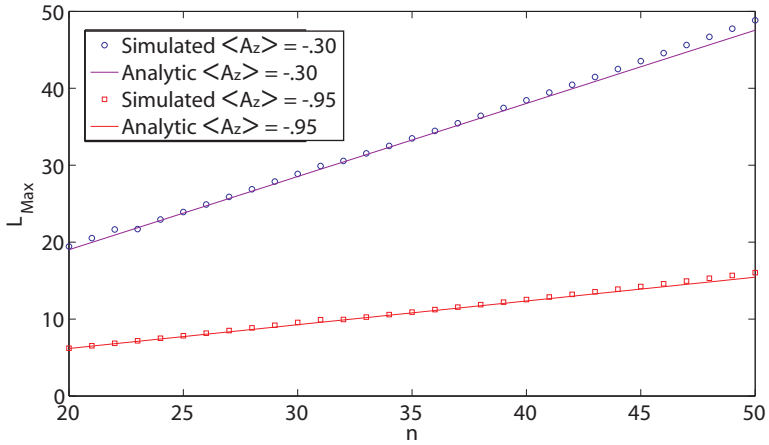

Figure A.7: Comparison between calculation and analytic results where n is varied. $\langle A_z \rangle$ is calculated as the time average of $A_z = (-v_x L_y + z/r) + 1/2(z^2 - r^2)F$.

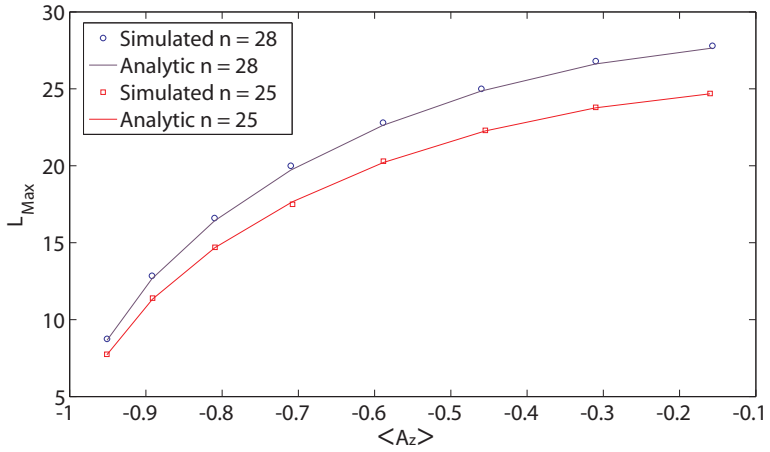

Figure A.8: Comparison between calculation and analytic results where $\langle A_z \rangle$ is varied.

by $\overrightarrow{\beta} = p_E cot\alpha_0[\hat{L} \times \hat{A}]$ [93]. The equations,

$$\beta_x = \mp A_z \frac{L_E p_E}{L} \tag{A.13}$$

$$\beta_z = \pm A_x \frac{L_E p_E}{L} \tag{A.14}$$

follow, describing the centers of circular orbits in momentum space. Since L is limited by L_{Max} in the Stark problem, the inequalities,

$$\beta_x \geq \mp A_z \frac{1}{L_{Max}} \tag{A.15}$$

$$\beta_z = 0 \tag{A.16}$$

are derived using the fact that when the angular momentum is maximum, $\overrightarrow{A}$ is parallel to the electric field axis. Considering the specific example where $\langle A_z \rangle \approx -1$, for which the approximation that the trajectories are like elliptical orbits perturbatively torqued is reasonable, the forbidden regions in momentum space should look like circles of radius $1/L_{max}$. Indeed, it is found numerically that the forbidden regions for the $\langle A_z \rangle = -0.95$ state are roughly circles of radius $1/L_{max}$ (see Fig. A.2).

Now, considering other cases, for example the two other cases calculated and displayed in Figs. A.3 and A.4, the simple picture of an electron only perturbatively torqued by the field is not valid. Yet, using Eqs. A.15, A.16, and R_p, all developed in the perturbative picture, we can predict the coordinates of the largest and smallest values of the forbidden regions along the p_x-axis. These coordinates, $(p_x, p_z) = (\pm R_p \pm A_z p_E/L_{max}, 0)$, represent the closest approach of a trajectory's outer turning point to the origin in momentum space, when $L = L_{max}$. In Figs. A.2-A.4, the forbidden region's boundary along the p_x-axis are determined, with the values stated in their respective captions. The results of these calculations agree well with analytical results derived from Eq. A.15 and A.16, demonstrating that the forbidden regions are, in part, reflections of the electron's momentum when it is at its maximum angular momentum. The electron's outer turning point in momentum space corresponds to the inner

turning point of the electron in position space. So we may further interpret the forbidden regions as a reflection of the electron's closest approach to the core when $L = L_{Max}$.

Interestingly, the maximum and minimum values of p_z in the forbidden region are apparently at the coordinates $(\pm 1/L_{Max}, \pm\langle A_z\rangle/L_{Max})$ for all values of n and $\langle A_z\rangle$ computed. The min and max values of p_z correspond to an electron near the inner turning point of its orbit, at low angular momentum. We have already discussed the case of $\langle A_z\rangle = -0.95$ and found that the forbidden regions are approximately circles of radius $1/L_{Max}$. Since here, $\langle A_z\rangle \approx -1$, this is consistent with the min and max values of p_z in the forbidden region. This case is relatively straightforward to understand. More difficult to understand is the small dipole moment case, for example when $\langle A_z\rangle = -0.32$. Unfortunately, using the simple model for these Stark states, we were not able to explain the forbidden space maxima and minima p_z-values. We can comment, that these coordinates depend strongly on the orientation of low-L trajectories, and in the case of $\langle A_z\rangle = -0.32$, $L \approx 0$. These low-L orbits are oriented at a large angle, θ, with respect to the z-axis. One might harken back to the picture in Fig. A.1, but in the present case, the orbital axes in both position and momentum space are rotated in the plane by θ. As well, the precessional rate of the angular momentum is fast in this part of the Stark orbit, so the simple picture we have introduced of ellipses only changing slightly is not accurate. One reason that the simple picture is successful for predicting coordinates $(\pm R_p \pm \langle A_z\rangle L_E p_E/L_{max}, 0)$ is that when $L = L_{Max}$, the precessional rate is slow, since the electron's orbit is parallel to the static field axis, and does not experience a torque. Despite the failure to determine a physical reason for the coordinates $(\pm 1/L_{Max}, \pm\langle A_z\rangle/(L_{Max}))$, these values are verified across the range of $\langle A_z\rangle$-values, so it is tempting to think that there must be a good physical way to understand these coordinates in momentum space.

The results of this section showed that the sizes of the forbidden regions are related to

L_{Max}. However, since the picture described for the forbidden regions is incomplete, a more sophisticated approach is necessary.

A.3.2 The equations of motion

To develop a complete picture of the electron orbits in the Stark problem, we go through an analysis of the equations of motion, through which limiting curves for the variables x, z, p_x, and p_z are found. The classical Stark problem has been studied previously as an illustration of an integrable perturbation to the Kepler problem [47, 102, 103]. This section follows Corben's [103] derivation of the problem. The derivation finds formulas for z as a function of x^2 - parabolas that intersect, and define the boundaries of a two dimensional region, in a plane parallel to the static electric field. The electron's orbit is bound in this two-dimensional region.

The generalized coordinates are set equal to the previously defined parabolic coordinates, $q_1 = \xi$ and $q_2 = \eta$. In turn, the generalized coordinates are defined in terms of the Cartesian coordinates as

$$x = q_1 q_2 \tag{A.17}$$

$$z = \frac{1}{2}(q_1^2 - q_2^2). \tag{A.18}$$

The kinetic energy in the parabolic coordinate system is

$$T = \frac{1}{2}[(q_1^2 + q_2^2)(\dot{q}_1^2 + \dot{q}_2^2)], \tag{A.19}$$

yielding canonical momenta

$$p_1 = (q_1^2 + q_2^2)\dot{q}_1 \tag{A.20}$$

$$p_2 = (q_1^2 + q_2^2)\dot{q}_2. \tag{A.21}$$

The Hamiltonian is

$$H = \frac{1}{2(q_1^2 + q_2^2)}[p_1^2 + p_2^2 - 4 - F(q_1^4 - q_2^4)], \tag{A.22}$$

where the -4 term comes from the r^{-1} term of the Coulomb potential. Born writes the equivalent term $-4me^2Z$ [47], where Z is the order number and equals unity for a single excited electron, as is the case here.

The Hamilton-Jacobi equation is then,

$$2E(q_1^2+q_2^2) = (\frac{dS_1}{dq_1})^2 + (\frac{dS_2}{dq_2})^2 - 4 - F(q_1^4 - q_2^4), \tag{A.23}$$

and this equation separates in the parabolic coordinate system, so that rearranged Eq. A.23 is,

$$(\frac{dS_1}{dq_1})^2 - 2Eq_1^2 - Fq_1^4 = -(\frac{dS_2}{dq_2})^2 + 2Eq_2^2 - Fq_2^4 + 4 = \alpha_1. \tag{A.24}$$

Given the definitions of S_1 and S_2 in the action-angle formalism, it is convenient to write,

$$S_1 = \int \sqrt{f_1(q_1)}dq_1 \tag{A.25}$$

$$S_2 = \int \sqrt{f_2(q_2)}dq_2, \tag{A.26}$$

where

$$f_1 = \alpha_1 + 2Eq_2^2 + Fq_2^4 \tag{A.27}$$

$$f_2 = -\alpha_1 + 4 + 2Eq_2^2 - Fq_2^4. \tag{A.28}$$

For real momenta $f_1(q_1) \geq 0$ and $f_2(q_2) \geq 0$. The roots of $f_1(q_1^2)$ are,

$$(q_{1roots})^2 = \frac{-E \pm \sqrt{E^2 - \alpha_1 F}}{F}. \tag{A.29}$$

We also examine the local extrema of $f_1(q_1^2)$:

$$0 = \frac{df_1}{d(q_1^2)} = 2E + 2Fq_1^2 \tag{A.30}$$

$$0 = \frac{d^2f_1}{d(q_1^2)^2} = 2F. \tag{A.31}$$

Hence, we see that $f_1(q_1^2)$ has a local minimum at $q_1^2 = -E/F$. At the local minimum $f_1 = \alpha_1 - E^2/F$, so conditions for the particle to be bound near the origin are that $\alpha_1 > 0$

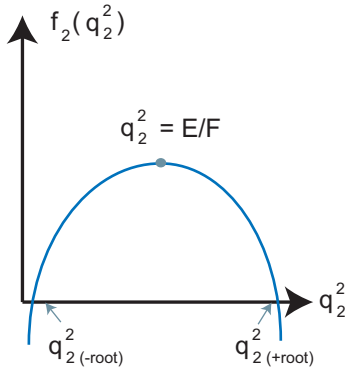

Figure A.9: Plot of $f_2(q_2^2)$. For real momenta, f_2 is greater than zero.

and $F < E^2/\alpha_1$ [103]. This implies that q_1 is bound between $0 \leq q_1 \leq q_{1max}$, and q_{1max} is given by the larger root in Eq. A.29 [103].

Consider next the roots of $f_2(q_2^2)$,

$$(q_{2roots})^2 = \frac{E \pm \sqrt{E^2 - (\alpha_1 - 4)F}}{F}. \tag{A.32}$$

Examining the extrema of $f_2(q_2^2)$, similar to was done for $f_1(q_1^2)$, we see that $f_2(q_2^2)$ has a local maximum at $q_2^2 = E/F$. The domain over which physical solutions of $f_2(q_2^2)$ exist is maximum at the larger root in Eq. A.32, and q_2 is bound by $0 \leq q_2 \leq q_{2max}$.

In summary, we derived bounds for the parabolic coordinates q_1 and q_2. Next, we consider what the maximal values of the parabolic coordinates imply about the orbits in Cartesian coordinates. Substituting into the definitions of the parabolic coordinates, we obtain for $q_1 = q_{1_{max}}$,

$$z = \frac{1}{2}(q_{1max}^2 - \frac{x^2}{q_{1max}^2}), \tag{A.33}$$

and for $q_2 = q_{2_{max}}$,

$$z = \frac{1}{2}(\frac{x^2}{q_{2max}^2} - q_{2max}^2). \tag{A.34}$$

Parabolas described by these equations are plotted in Fig. A.10- A.12 a). These curves define boundaries for the electron's trajectory in position space.

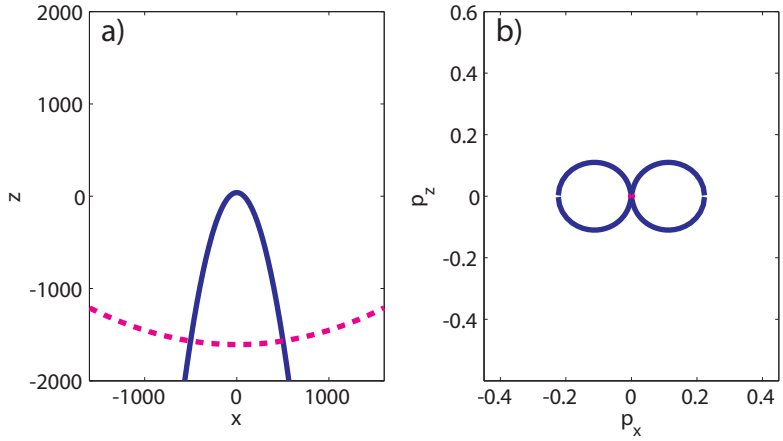

Figure A.10: a) Solid curves are z plotted as a function of x, with the function given by Eq. A.34. The dashed curves are z plotted as a function of x given by Eq. A.33. The electron's motion is constrained to the area defined by these parabolas. b) Solid curves are coordinates $(p_x(x),p_z(x))$, using Eqs. A.37-A.40. The dashed line (not visible on this scale) are coordinates $(p_x(x),p_z(x))$, defined in Eqs. A.41-A.44. These plots are computed with $\alpha_1 = 3.9$, $F = 104V/cm$, and for the energy level $n = 28$, producing curves that constrain orbits similar to those plotted in Fig. A.2.

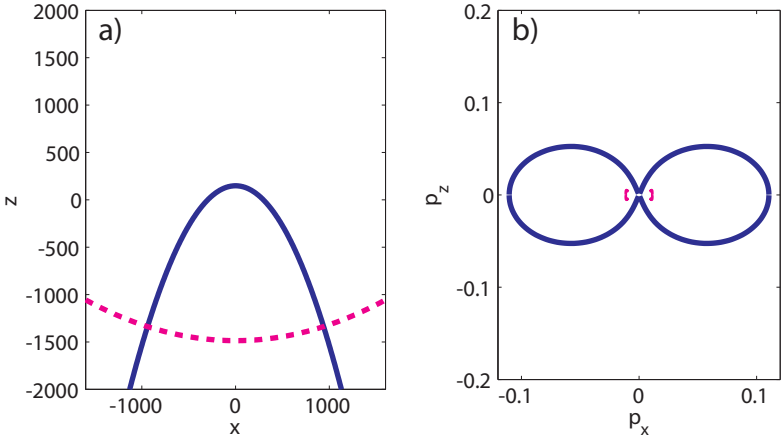

Figure A.11: For a) and b) The different curves are defined in Fig. A.10. These plots are computed with $\alpha_1 = 3.64$, $F = 104V/cm$, and for the energy level $n = 28$, producing curves that constrain orbits similar to those plotted in Fig. A.3.

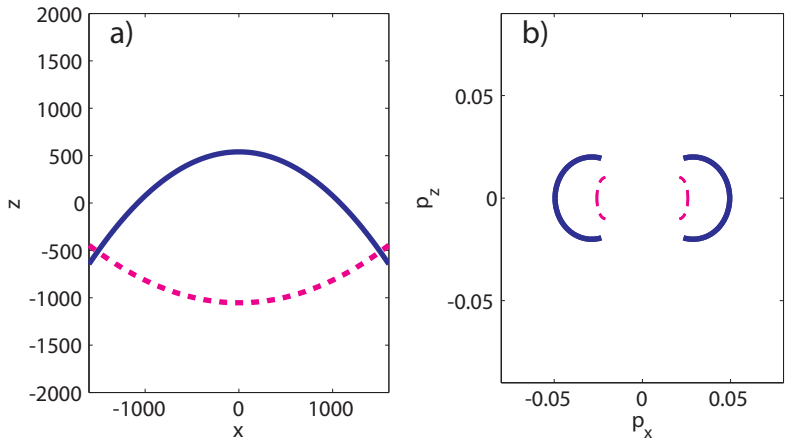

Figure A.12: For a) and b) The different curves are defined in Fig. A.10. These plots are computed with $\alpha_1 = 2.9$, $F = 104V/cm$, and for the energy level $n = 28$, producing curves that constrain orbits similar to those plotted in Fig. A.4.

Forbidden regions in momentum space

The paraboloid boundaries found in the last section provide equations that describe the forbidden regions in momentum space. Differentiating the coordinate space Eqs. A.33 and A.34 yields forms for the momentum. Equation A.34 is differentiated to obtain the momentum equation,

$$p_z \leq \frac{xp_x}{q_{2_{max}}^2}. \tag{A.35}$$

Considering now the energy equation, in Cartesian coordinates,

$$E = \frac{1}{2}(p_x^2 + p_z^2) - 1/\sqrt{x^2 + z^2} - zF, \tag{A.36}$$

together with the relation derived between p_z and p_x at the position space boundary (Eq. A.34) obtains,

$$p_x \geq \sqrt{\frac{2(E + 1/\sqrt{x^2 + z^2} + zF)}{x^2/q_{2_{max}}^4 + 1}} \tag{A.37}$$

$$p_x \leq -\sqrt{\frac{2(E + 1/\sqrt{x^2 + z^2} + zF)}{x^2/q_{2_{max}}^4 + 1}}. \tag{A.38}$$

Although Eqs. A.37 and A.38 are not pretty, since z is determined in terms of x and q_{2max}, when the electron's ellipse is tangent to the parabolic boundary, these equations determine

p_x, in terms of only one variable, x. Additionally, when the electron is tangentially on the parabolic spatial coordinate boundary, back substitution into Eq. A.35, yields p_z as a function of one variable, x,

$$p_z \geq \frac{x}{q_{2_{max}}^2}\sqrt{\frac{2(E+1/\sqrt{x^2+z^2}+zF)}{x^2/q_{2_{max}}^4+1}} \tag{A.39}$$

$$p_z \leq -\frac{x}{q_{2_{max}}^2}\sqrt{\frac{2(E+1/\sqrt{x^2+z^2}+zF)}{x^2/q_{2_{max}}^4+1}}. \tag{A.40}$$

Thus the forbidden regions in momentum space are manifestations of the coordinate space boundaries, and parametric equations describing the boundaries in terms of x are found. The other coordinate space boundary, defined by Eq. A.33 yields,

$$p_x \leq -\sqrt{\frac{2(E+1/\sqrt{x^2+z^2}+zF)}{x^2/q_{1_{max}}^4+1}} \tag{A.41}$$

$$p_x \geq \sqrt{\frac{2(E+1/\sqrt{x^2+z^2}+zF)}{x^2/q_{1_{max}}^4+1}} \tag{A.42}$$

$$p_z \leq -\frac{x}{q_{1_{max}}^2}\sqrt{\frac{2(E+1/\sqrt{x^2+z^2}+zF)}{x^2/q_{1_{max}}^4+1}} \tag{A.43}$$

$$p_z \geq \frac{x}{q_{1_{max}}^2}\sqrt{\frac{2(E+1/\sqrt{x^2+z^2}+zF)}{x^2/q_{1_{max}}^4+1}}. \tag{A.44}$$

These conditions define the minimum values of $|p_x|$ for the forbidden regions, along the p_x-axis. For the specific case plotted in Fig. A.10 a), the momentum space boundaries are shown in b). As the electron is confined less along the x-direction, the area between the parabolas in spatial coordinates becomes wider. With more area to explore, the electron has smaller forbidden regions in momentum space. This is delineated in Fig. A.11 which shows the momentum space boundary when the electron's dipole moment is $\langle A_z \rangle = -0.82$ (corresponding to Fig.A.3). The forbidden regions in momentum space are not completely constrained by the equations derived in this section, as seen clearly in Fig. A.12. However, the momentum directly along the p_x-axis is constrained by the equations derived. For still

smaller dipole moments, the boundaries defined by the equations described here become even closer together. As the dipole moment goes to zero, the forbidden regions shrink to zero. Then at larger, positive dipole moments, the role of the two boundaries, as far as which boundary constrains the maximum and minimum values on the p_x-axis, is reversed.

The physical picture is found by considering the electron on an approximately elliptical trajectory, where the electron's trajectory cannot cross the boundaries defined by Eqs. A.33 and A.34. So the trajectory of the electron follows a path that reflects from the combined Coulomb/Stark potential, and subsequently only tangentially approaches the corresponding forbidden region of momentum space. The probability distribution in momentum space is symmetric about the p_x-axis, and thus forbidden regions are symmetric as well. Given this, the forbidden regions are ellipses, with an axis defined by the p_x-equations given in this derivation.

A.4 Conclusions

Numerical studies of the classical equations of motion in the Stark problem show that there are forbidden regions in momentum space. Treatment of the Hamilton-Jacobi equations of motion yield equations that define the boundaries of the forbidden regions in momentum space. From this analysis, we see that the boundaries are a result of the electron's confinement in the Stark problem. As well, a simple derivation considering the electron at its maximum angular momentum near the core seems to provide a clear picture of the maximum of the forbidden region along the p_x-axis. This discussion contributes to the understanding of the Stark problem from the classical point of view. Additionally, these trajectory pictures aid in understanding the probability distribution in momentum space, since the forbidden regions result in areas of small probability. Notably, a small probability region reflecting the forbidden region in momentum space is observed in the measurement of the Stark states

presented in Ch. 5.